ADVANCEMENTS IN MICROFLUIDICS FOR BIOTECHNOLOGY APPLICATIONS

A DISSERTATION
SUBMITTED TO THE FACULTY OF THE GRADUATE SCHOOL
OF THE UNIVERSITY OF MINNESOTA
BY

Pranav Agrawal

IN PARTIAL FULFILLMENT OF THE REQUIREMENTS
FOR THE DEGREE OF
DOCTOR OF PHILOSOPHY

Advised by:
Theresa M. Reineke
Kevin D. Dorfman

October 2018

Acknowledgement

I would like to thank my advisors Professor Theresa Reineke and Professor Kevin Dorfman for giving me the opportunity to work on a wide variety of projects and applications. They have always been approachable and patient especially during tough times. It has been a privilege to learn from both of them.

A part of the research in this thesis was done in close collaboration with Professor Jacob Tolar, Wei-Shou Hu, Gary Dunny, and their group members. I'm immensely grateful that they were willing to work with me. Minnesota fabrication centre and its staff was very important for all my fabrication work and I like to thank Paul, Kevin, Mark and Tony for training and help.

I am also grateful for the consistently friendly and collaborative culture of the Bio Group. I would like to acknowledge the group members who have been generous with their time and always willingly participated in helpful discussions over the years. I am grateful to my mentors – Nilesh, Will, Haley, Yogesh, Dustin, Julian, Scott and Zhicheng, who displayed saint-like patience, teaching me without hesitation. I am grateful to my friends in the lab for the wonderful time and fun conversations – Victoria, Mammad, Jeff, Seyoung, Anatolii, Leon, Yaming, Zhe, Snain, Annie, Monica, Craig, Ngoc, Rashid, Derek, Ethan, Akash, Abhiram, Hui-Min, Seunghwan, Xioalin, GK, Vaidya, Aditya, Mathew and Paridhi. I had a great time working with Marian, Ommar and Zsófi. A special mention to Julie, Teresa, Joe, CEMS and Chemistry office staff for all their help and consideration.

A big thanks to all my friends – Sujay, Abhinav, Chowdhary, Rohit, Nitish, Anurag, Biswa, Ami, Rishabh, Billi, Vikas, Shashank who provided me with wonderful and lifelong

memories of the amazing time we spent together. Most importantly, I would like to thank my family who has always believed in me and supported me in every decision.

Dedicated to my family

Abstract

Microfluidic technology has made a huge impact in the field of biotechnology and life sciences. The advancements can be categorized into three aspects: understanding of physical phenomena at the microscale; development of tools for easy integration of different phenomena; and devising systems for various applications. This thesis highlights the ability of microfluidic technology in manipulating different biological entities by fabricating small feature sizes. In particular, we have focused on the development of new processes for three biotechnology applications – (i) long DNA sample preparation for genomic; (ii) delivery of genetic delivery vehicles for gene and cell therapy; and (iii) an *in vitro* model to study human gut. Each of these systems is developed in close collaboration with potential users and is aimed towards easy integration with the existing workflow.

Long-read genomic applications such as genome mapping in nanochannels require long DNA that is free of small-DNA impurities. Chapter 2 reports a chip-based system based on entropic trapping that can simultaneously concentrate and purify a long DNA sample under the alternating application of an externally applied pressure (for sample injection) and an electric field (for filtration and concentration). In contrast, short DNA tends to pass through the filter owing to its comparatively weak entropic penalty for entering the nanoslit. The single-stage prototype developed here, which operates in a continuous pulsatile manner, achieves selectivity of up to 3.5 for λ-phage DNA (48.5 kilobase pairs) compared to a 2 kilobase pair standard based on experimental data for the fraction filtered using pure samples of each species. The device is fabricated in fused silica using standard clean-room methods, making it compatible for integration with long-read genomics technologies.

Non-viral delivery vehicles are becoming a popular choice to deliver genetic materials for various therapeutic purposes, but they need engineering solution to improve and control the delivery process. In Chapter 3, we demonstrate a highly efficient method for gene delivery into clinically relevant human cell types, such as induced pluripotent stem cells (iPSCs) and fibroblasts, reducing the protocol time by one full day. To preserve cell physiology during gene transfer, we designed a microfluidic strategy, which facilitates significant gene delivery in short transfection time (<1 minute) for several human cell types. This fast, optimized and generally applicable cell transfection method can be used for rapid screening of different delivery systems and has significant potential for high-throughput cell therapy applications.

Microfluidic *in vitro* models are being developed to mimic individual or combination of various human organ functions for systematic studies, and for better predictive models for clinical studies. In Chapter 4, we outline a microfluidic-based culture system to study host-pathogen interaction in the human gut. We demonstrate that the infection of *Enterohemorrhagic Escherichia coli* (EHEC) in epithelial cells are oxygen dependent and can be used to prolong co-culture of bacterial and epithelial cells. This work presents a large scope to study the factors influencing the infection, especially the commensal microbiome in the human gut.

Overall, this thesis shows how the microfluidic system can be useful in solving real-life problems and envision further advancements in the field of biotechnology.

Table of Contents

List of Figures

List of Tables

Statement of the Author's Contributions

Portions of this dissertation were written in collaboration with the members of the Dorfman, Reineke, Tolar, Hu and Dunny group. Some chapters have also appeared as articles in various journals. Here, I would like to point out the contributions of the different people involved.

Chapter 2 was published as an article: Pranav Agrawal, Z. Bognár and K. D. Dorfman, "Entropic trap purification of long DNA", *Lab Chip*, 18, 955 (2018). In this paper, we have developed a chip-based system based on entropic trapping that can simultaneously concentrate and purify a long DNA sample under the alternating application of an applied pressure (for sample injection) and an electric field (for filtration and concentration). I performed all experiments and data analysis for the published work. The original resistor code was developed by K.D.D and I further modified based on the actual device design. I developed the initial COMSOL model and Z.B expanded the model to incorporate various device dimension for predicting electric field profile inside the device. K.D.D and I wrote most of the paper.

Chapter 3 appeared as Pranav Agrawal, N. P. Ingle, W. S. Boyle, E. Ward, J. Tolar, K. D. Dorfman, and T. M. Reineke, "Fast, Efficient, and Gentle Transfection of Human Adherent Cells in Suspension", *ACS Appl. Mater. Interfaces*, 8, 8870 (2016). This paper demonstrated a highly efficient method for gene delivery into clinically relevant human cell types, such as induced pluripotent stem cells (iPSCs) and fibroblasts, reducing the protocol time by one full day. The experiments for this paper were conceived, initiated and designed by N.P.I, K.D.D, T.M.R and me. J.T provided the PFB cells and iPSCs. I and W.S.B. performed iPSC experiments. E.W. trained and advised on iPSCs culture protocol. I and N.P.I carried out the rest of the biological experiments and analyzed the results. I designed and fabricated the microfluidic device. Experimental conditions and operating parameters were optimized by me and N.P.I. The manuscript was written by N.P.I, K.D.D, T.M.R and I, with contributions from other authors.

I wrote Chapters 1, 4 and 5. Chapter 4 is an unpublished work performed in collaboration with E. Cameron, A. Bandyopadhyay, O. Hammami, W.S. Hu, G. Dunny, T.M. Reineke and K. D. Dorfman. All collaborator contributed to the development of the initial idea for this study. E.C performed the coverslip-based experiments. I performed device fabrication, microfluidic device-based experiments and confocal imaging for the bacterial infection on the microfluidic device.

Chapter 1 – Introduction and motivation

1.1 The role of microfluidics in biotechnology

The last two decades have seen major advancements in microfluidic-based research, especially in the fields of biotechnology and life science (Figure 1.1a).[1] The average timeline for a technology development to reach widespread commercialization from the lab scale is 29 years.[2] In the case of microfluidic, it has already made a huge impact as many have reached a commercial stage. The microfluidic market was valued at $1.6 billion and is projected to reach $3.5 - 5.8 billion by 2018.[3] Some of the popular and important applications of these technologies involve targeted diagnostic platforms,[4] analytical tools,[5] *in vitro* models,[6] nanoparticle assembly, genomics, and sample preparation.[7] The term "lab-on-a-chip" has been coined for certain microfluidic technologies that miniaturized specific laboratory functions or operations. Several laboratory functions have already been translated to the micro- or nanoscale including drug and biologics delivery,[8] cell- and biochemical-based assays, cell sorting,[9] gel electrophoresis,[10] and various chemical reactions. Initial technology developments stemming from engineering laboratories are limited to only a handful of the population, mainly due to the requirement of expertise and the high cost of adaptation by a non-engineering laboratory. The major engineering contribution to the field has been the development of scaling laws, based on various physical concepts such as fluid flow and surface forces, for device design as well as tools for device fabrications. The first major

success in the translation of microfluidic technology for general users is point-of-care diagnostic, especially for developing nations. Another important example is genome sequencing – the innovative conglomeration of microfluidics, biochemistry, optical and electronic techniques have translated a multibillion-dollar project to a $1000 commercial product (Figure 1.1b). Most advances were made when the developmental efforts were focused on either reducing the total operational cost such as that of genome sequencing or achieving functionalities which, otherwise, cannot be easily implemented using existing methods such as single cell manipulation. The increasing popularity of the field and interdisciplinary collaborations have refined the developmental approach for laboratory and commercial applications.

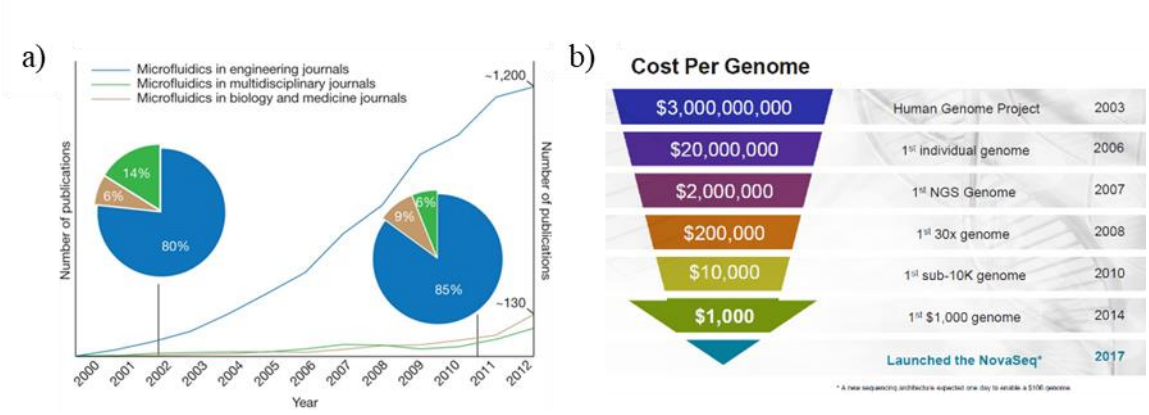

Figure 1.1 a) Microfluidic publications in engineering, multidisciplinary, and biology and medicine journals from 2000 to 2012. Figure adapted from *Nature*.[1] b) Time and cost estimation for the genome sequencing. Reproduced from Illumina (2018).

The characteristic advantages of microfluidic technology include low cost and design flexibility in fabrication, high-throughput or multiplex systems with process automation capabilities, real-time and on-line analysis, and low reagent and sample cost.

All these advantages stem from advancements in the fundamental understanding and the fabrication tools for the microfluidic applications. The cost, flexibility and multiplexing in the microfluidic technology is a direct consequence of advancements in the fabrication tools and the material development. The low reagent cost and fast response time are attributed to the small length scale involved in this technology which is a direct result of the in-depth understanding of the scaling laws at nano- and microscale in addition to the fabrication advancements. One example is the microfluid-based assay provides an additional advantage of assessing biological response at the single-cell level as compared to the large cell population at the macroscale that can have inherent heterogeneity in the cell population. In this assay, a minimum cell concentration is necessary to detect the biological response; operating at small volumes (nano-litres) will require 1 cell as compared to 10^6 cells when operated at the macroscale (millilitre). Indeed, in these examples, it is necessary to have a thorough understanding of the scaling laws and fabrication tools relevant to the microfluidic technology.

1.2 Basic physics of microfluidics

The physical phenomena and forces dominant at the microscale may be significantly different from that observed at the macroscale and this drives some of the applications that were not feasible before the advent of microfluidic technology.[11] A scaling law, determined by a dimensionless number, compares the significance of two competing forces or phenomena.

A common dimensionless number characterizes the fluid flow is the Reynolds Number (Re), which compares the impact of inertial to viscous forces and determines the flow profile in the channel. Re is given by $\frac{\rho U_0 D_h}{\eta}$, where ρ and η are the density and viscosity of fluid respectively, while U_0 and D_h represent characteristic fluid velocity and channel dimension respectively. Re is generally used to predict the flow profile in the channel: laminar or turbulent (Figure 1.2a & b). For a fluid, Re is proportional to the channel dimension. Turbulent flow profile is more prevalent at the macroscale for large Re (>~2300) and is characterized by the time-dependent chaotic flow. For a microfluidic system, Re typically ranges between 0.1 to 10. The laminar flow in a microchannel is dominated by viscous flow and has a time-independent flow profile. Such flow condition is either a blessing or a curse depending on the application. For example, the laminar flow profile has been used to promote cell sorting. On the other hand, the parallel flow profile makes it very difficult to mix two streams and therefore require other methods to assist in mixing at the microscale.

Diffusion is the net movement of small molecules from the region of high concentration towards low concentration because of the Brownian motion (Figure 1.2c). The distance travelled by a molecule in a one-dimensional system is represented by $d^2 = 2Dt$, where d is the distance travelled by a particle with diffusivity D over time t. The diffusivity of a particle depends upon its size, and smaller particles diffuse faster compared to large particles. At the microscale, diffusion often competes with convective flow. This

is represented by the Peclet number$\left(Pe \equiv \frac{lU_0}{D}\right)$, which is the ratio between timescales for diffusion and convection. The most common application involves the diffusion of molecules perpendicular to that of the fluid flow. For example, in the case of mixing of two streams in a straight channel, diffusion is the dominant mechanism for the motion of molecules between parallel flow fields. A fast response in a microfluidic system is due to the rapid transport process, which is a direct result of the high surface area to volume ratios (*SA/V*) in a microfluidic system. Novel device designs have been tested for high *SA/V* and have achieved fast mixing or controlling isothermal conditions for various biological processes. For example, efficient temporal and spatial temperature control helps in achieving high-quality polymerase chain reaction in different microfluidic systems.[12]

Several other surface forces dominate significantly in microscale systems. For example, the capillary phenomenon, which is an interplay between the surface tension of the liquid and the surface chemistry and geometry of the channel, is dominant at the microscale (Figure 1.2d & e). A popular application of this phenomena at the microscale is droplet microfluidics where droplets are generated based on the difference in the interfacial tension between two immiscible liquids.[13] These droplets are often used as micro-reactors to perform biological and chemical processes such as single-cell genomics.[14] Oil-water systems are commonly used for droplet-based microfluidic systems. Capillary number compares the importance of viscous forces with respect to the interfacial tension and it represented by $Ca = \frac{\eta U_0}{\gamma}$, where γ of the surface tension of a liquid. Another popular phenomenon is electro-kinetic transport comprising of electro-osmosis and

electrophoresis.[15] Electro-osmosis is the motion of the bulk liquid in the presence of an external electric field and requires the presence of charge double layer at the solid-liquid interface. On the other hand, electrophoresis is the motion of a charged particle in a stationary liquid in the presence of an external electric field. The electro-kinetic transport

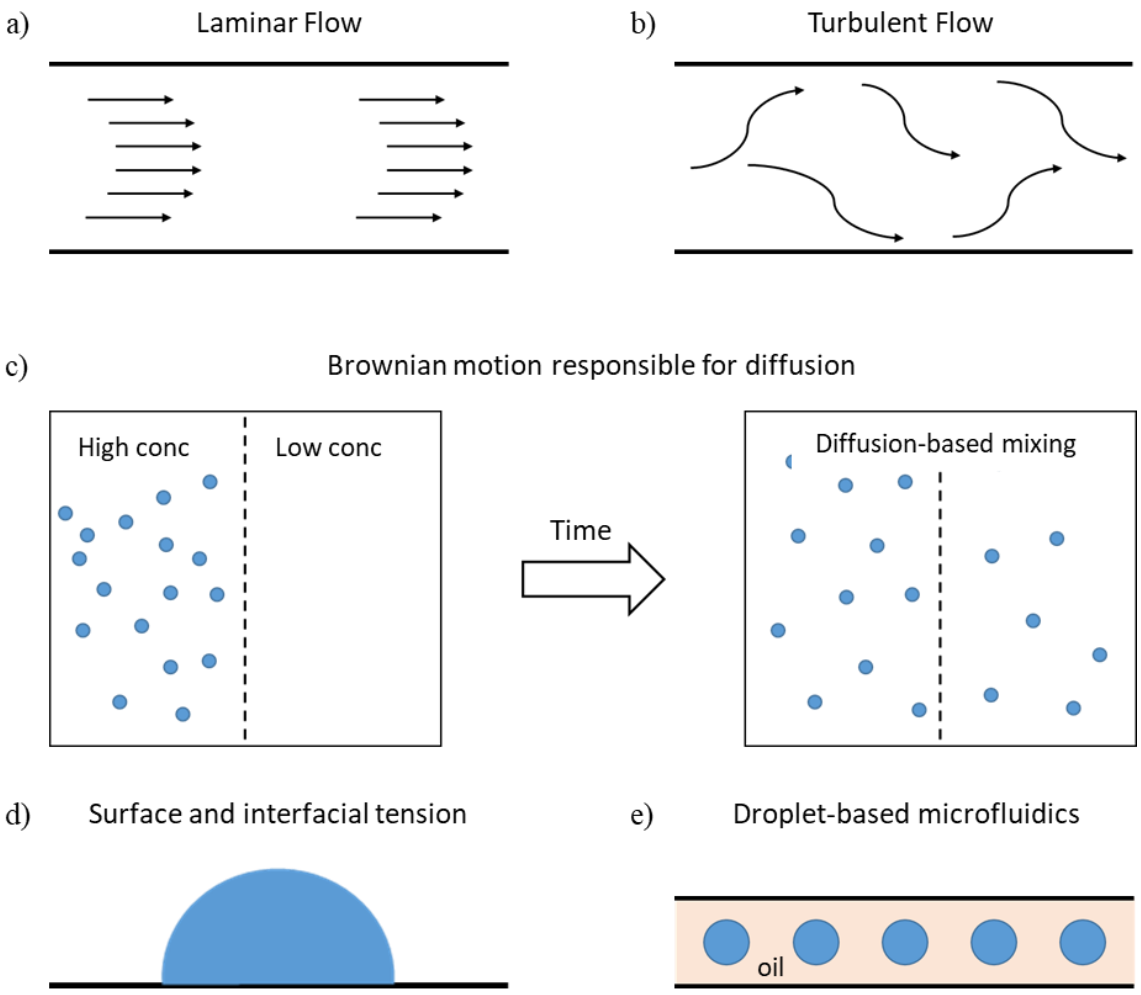

Figure 1.2 Different physical phenomenon prominent in microfluidic systems: a) Laminar vs b) turbulent flow regime. The arrow represents the velocity streamlines for two flow regimes. c) Schematic representing the diffusion of small molecules from the high concentration region to low concentration region over time. d) Surface and e) interfacial tension are the net forces at air-liquid or immiscible liquid-liquid interfaces and are dominant at the microscale.

phenomenon becomes important when the width of the charge double layer becomes comparable to the size of the channel or charged molecules. This has been very useful in the manipulation of polyelectrolytes such as DNA, protein, as well as, plug-like fluid flow without external pressure. For a specific application, the use of appropriate phenomenological model (scaling laws) is often dictated by its compatibility with the fabrication tool and materials used in the fabrication required for the implementation of the model.

1.3 Engineering tools for microfluidics

The theoretical understanding of many of the above discussed physical phenomenon has been under development for years, but their true potential for the microfluidic system was realized due to the advancement in the fabrication tools that facilitate the implementation of relevant physical conditions necessary for an application. Conventional microfabrication techniques were the early tools adopted for fabricating microfluidic devices, which involved the patterning of the desired design in a photosensitive polymer (photoresist) and transferring the final pattern to the desired material. Silicon and glass are popular material choices for bulk manufacturing using microfabrication, in semiconductor and microelectromechanical systems (MEMS) industry. The commercial application of microfabrication has streamlined fabrication protocols along with sophisticated equipment and advanced materials for various applications.[16] Despite the advancements in the semiconductor and MEMS industry, the

advent of elastomer-based lithography – Polydimethylsiloxane (PDMS) replica molding – was the major factor that promoted the widespread use of microfluidic technologies.

The PDMS-based fabrication, often referred to as the soft lithography, involves the fabrication of the silicon mold that usually contains the negative pattern of the design intended to be fabricated followed by mold casting with well-mixed PDMS precursors and thermal crosslinking for the final pattern.[17] The elastomeric nature of PDMS allows easy peeling of the casting from the mold as well as the simple punching of access hole for the fluidic connections. The elastomeric property is also very crucial for some of the novel device designs such as on-chip pumps and valves. In addition to the elastomeric property, PDMS is virtually the default material for laboratory microfluidic devices due to its low cost, ease of fabrication, good optical property for imaging (transparent to broad wavelengths with low autofluorescence of the material), high gas permeability for cell culture and biocompatibility. However, PDMS possess some limitations in the casting process as well as its use for the microfluidic devices. Commercial PDMS formulation is too soft for the fabrication of high aspect ratio features, assist non-specific protein and small molecule adsorption on its hydrophobic surface, and is incompatible with common organic solvents. High water permeability in PDMS can be challenging to handle, as it can introduce bubbles during device operation. Several chemical modifications for PDMS-based lithography has been explored in the literature to tackle the aforementioned limitations, including post-curing surface modification,[18] and change in chemical formulation.[19] In addition, new elastomeric materials have been tested as well as their

casting protocols are being standardized for soft lithography. As microfluidic technologies advance from the lab scale to the commercial scale, more accessible and cost-effective materials such as polymethyl methacrylate,[20] cyclic olefin copolymer,[21] or polycarbonate[22] are being explored as alternatives that can be fabricated with the variety of the industrial techniques including microinjection molding, hot embossing, casting and mechanical or laser micromachining.

Glass and silicon are also popular materials, especially for commercial applications.[23] There are many applications where both materials provide advantages over the polymeric such as precise definitions of nano-scale channels or pores, fabrication of high aspect ratio structures, chemical resistivity and ease of electrode integration. The high material or equipment cost associated with both materials are often mitigated through bulk manufacturing or device reusability. For example, different wafer sizes ranging from 2"–12" diameter are already available for bulk manufacturing which lowers the development cost when it is being adopted for microfluidic-based commercial applications. At the laboratory scale, silicon is advantageous for applications that require high thermal conductivity, hydrophilic surface and electrode integration. The wet and dry etching processes are already standardized for fast and precise small-scale fabrications. Moreover, several bonding methods including thermal, anodic and adhesive bonding assist in easy integration with different materials.

For many electro-kinetic applications, silicon dioxide is chemically grown on Si as an insulating layer. Glass wafer provides a simple alternative for such applications.[24,25]

Furthermore, it also provides precise feature size with the possibility of high aspect ratio structures, transparent material for imaging, high chemical resistance and established chemical modifications for tuning the surface hydrophobicity. Fabrication and bonding methods similar to those of silicon are also available for glass materials.[26] Three types of glass materials are popular for such applications – soda lime, borosilicate and quartz. Soda lime can achieve fast etching and high bonding strength at a relatively lower temperature, but it provides lower etch quality and suffers from high autofluorescence. On the other extreme, quartz is the purest form of SiO_2 with minimal autofluorescence and background noise making it ideal for optical application. However, it has a very slow etch rate for fabricating features and requires high temperature for thermal bonding.

All of the above techniques require a cleanroom facility for part or complete device fabrication, which significantly increases the overall fabrication cost and limits the potential users. Recent advancements are being made to use rapid prototyping techniques like 3D printing for the microfluidic device fabrication. A major motivation comes from the development and commercialization of several 3D products with useful resolution and accuracy, and some are as cheap as a few thousand dollars.[27] A 3D printing approach is especially an attractive tool for microfluidic as it supports the designing of complex geometry in a three-dimensional space, which otherwise is difficult and expensive to fabricate using microfabrication methods. 3D printing for microfluidic devices has been successfully implemented for simple and larger geometry (>100 μm). This technology is still in a developmental stage – in terms of the desired resolution and accuracy for smaller

length scales as well as a small library of material that can be used with commercial systems.[28] However, new printing design and materials are being developed both at the laboratory and industrial scale that leads to a large number of 3D printing-based devices, making it a "next-generation" tool for microfluidic technology.

1.4 Research outline

With great advancements in the fundamental understanding and development of diverse engineering tools for the microfluidic technology, the field is now well poised for its implementation in various biotechnology applications. An important consideration in this endeavour is to realize the shortcomings of existing protocols/processes or the need for a new method and then devising a simple platform that can be easily integrated into the existing workflow. *The objective of this dissertation is to advance the existing microfluidic technology for novel applications in the field of biotechnology, in particular for the fast delivery of genetic materials necessary for cell therapy, efficient sample preparation for genomics and a reliable in vitro model to study gut microenvironment.* Each of the systems presented in this dissertation was built upon the need to improve conventional standards in an application and used the conventional methodology for the validation of the new system.

Figure 1.3 demonstrates the range of length scale in the human body along with the relative length scale that is accessible with the microfabrication techniques and has been explored in this dissertation. Nucleic acids are fundamental to the existence of living species as it constitutes the genetic material of cells in the form of deoxyribonucleic acid

(DNA) as well as ribonucleic acid (RNA). The ability to manipulate this genetic material is very crucial for the mechanistic understanding of cellular function and disease manifestations as well as various biotechnology applications. A DNA is made up of four types of nucleotides (or base) – adenine (A), guanine (G), cytosine (C) and thymine (T), while for RNA, the fourth nucleotide is uracil (U) instead of thymine. The size of a nucleotide is in the order of a few angstroms. However, the assembled nucleic acid may range from tens of nanometers to few microns, depending upon its source and usage. For example, a human genome is over 3 billion base pairs (bp) while the circular DNA (plasmid) for a cell therapy has few thousand base pairs. The size and complexity of the genetic materials in a cell depends on the type of cells and organism. Prokaryotic cells are simple cells with less genetic information with few cellular functions and small cell size

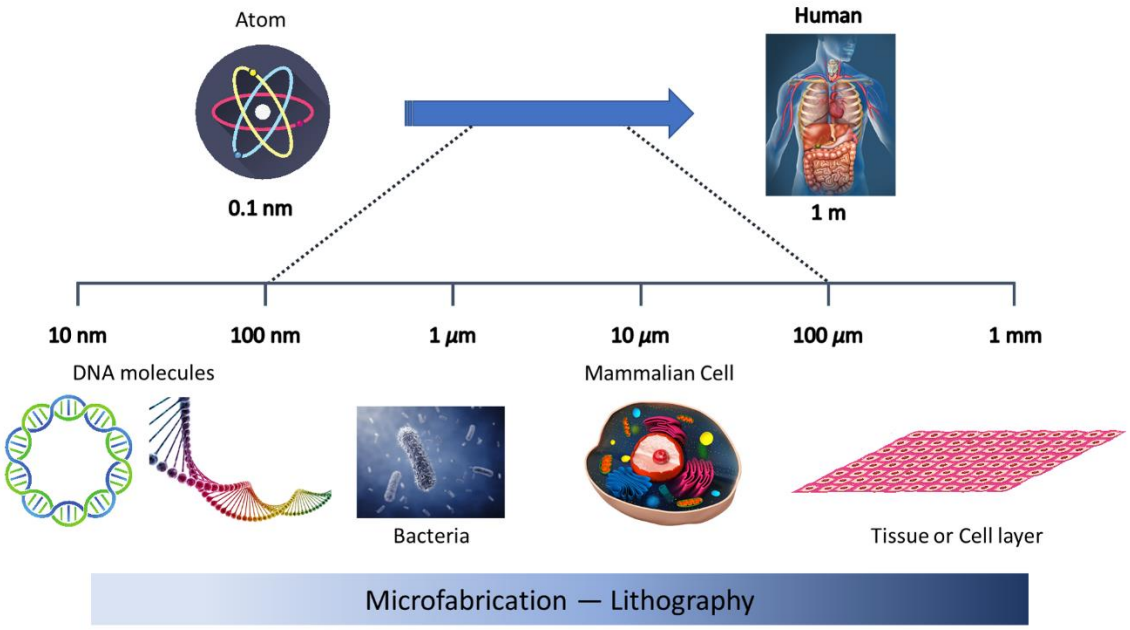

Figure 1.3 Size range in a biological system and the relevant length scales used in this dissertation using microfluidic systems.

(few hundred nanometers). On the other hand, eukaryotic cells such as human epithelial cells have much more complex machinery that is encoded in large genomic material and is bigger in size (few microns) than that of prokaryotic cells. Furthermore, a network of cells and extracellular matrix forms tissues which may extend to much larger sizes (few millimetres), as shown in Figure 1.3. *This dissertation demonstrates the use of microfluidic-based systems to manipulate different biological entities for various biotechnology applications.*

Chapter 2 aims towards the development of a unit operation to prepare samples for long DNA applications, especially for genome mapping. In nature, the genomic material in cells are efficiently packed and well-guarded inside the nucleus, even during the cellular division process. However, extraction of a purified and intact DNA sample is vital for the correct *in vitro* decoding of the genomic data. Genome mapping, in particular, aims towards providing accurate location of the specific base sequence along the DNA backbone, which necessitates the use of long intact DNA for the analysis. Even though the genome mapping is a microfluidic-based system, it still relies on the conventional agarose plug for DNA extraction and purification. Furthermore, the workflow of genome mapping system requires a liquid DNA sample and the mechanical shearing of long DNA during pipetting introduces undesired short DNA fragments in the sample. *Chapter 2 demonstrates a microfluidic platform that can filter short DNA fragments from the DNA mixture and supply a purified long DNA sample for downstream applications.*[29] Moreover,

the device fabrication protocols were similar to those used for the fabrication of genome mapping chips and can easily be integrated into the existing workflow.

In Chapter 3, we optimized the delivery protocol for the delivery of genetic material to adherent mammalian cells using non-viral delivery vehicles. Genetic medicine is a paradigm for personalized medicine but its delivery to the cell is inherently limited by cellular defense mechanism such as a structural barrier from the cellular and nuclear membrane as well enzymatic degradation inside the cells. The new chemical and biological vehicles are being clinically evaluated as potential carriers for the delivery of genetic material to the appropriate location inside the cell, mostly inside the nucleus for the plasmid delivery. For *in vitro* or *ex vivo* delivery, homogeneous and controlled delivery of payloads to the entire cell population is a crucial parameter for the therapeutic success. Moreover, as this therapeutic approach is advancing towards its clinical use, fast screening of various carriers is also necessary during the developmental phase. A major focus has been on designing delivery vehicles to overcome some of the natural barriers for efficient delivery. *However, instead of designing new carriers, we employed commercial delivery vehicles to demonstrate engineering solution to expedite the delivery of gene carriers to cells surface and designed ways to controls this delivery at almost a single-cell level.*[30]

Chapter 4 discusses the ongoing efforts to develop an *in vitro* model for the study of host-microbe interaction in a human gut. The human gut is the house of a diverse microbiome that contributes to a unique microenvironment and is difficult to replicate in an *in vitro* setting. The animal model as well as human gut samples are acceptable platforms

to study interactions of the microbiome in the gut but are limited by experimental and ethical considerations. Conventional *in vitro* models involving a plate system does not allow several experimental conditions such as prolong cell viability during coculture of bacteria and epithelial cells, the dependence of the pathogenic response on the commensal microbiome, and selective microenvironment for bacterial and epithelial cells, especially for pure anaerobes. These limitations are attributed to the lack of human physiological condition including the absence of fluid flow and low oxygen concentration. These *in vivo* conditions are responsible for modulating the culture media conditions on the apical and lumen side of the gut. *In Chapter 4, we demonstrate a combinatorial solution involving the engineering and biological approach to control the oxygen supply for host-microbe coculture.* Furthermore, the use of this new system highlights the dependence of the virulence of *Enterohemorrhagic E. coli* (EHEC) in human epithelial cells on the oxygen flux into the system.

Finally, Chapter 5 summarizes the salient features of the three platforms discussed in this dissertation. In addition, an outlook is provided on their advancements in the intended fields as well as new opportunities for the potential application of these devices.

Chapter 2 – Entropic trap purification of long DNA

2.1 Introduction

The last decade has witnessed massive improvements in the ability to read genetic information, ranging from short DNA fragments to whole human genomes. DNA can be read over short distances with single base pair resolution through DNA sequencing,[31,32] as well as over long distances at lower resolution via genome mapping.[33–36] The deployment of these new genomics methods has introduced new challenges in sample preparation. One major factor is the quality of the DNA samples, especially when working with long DNA molecules for genome mapping or long-read sequencing using the PacBio system.[37] Long DNA samples are typically contaminated with short DNA fragments that arise from shearing of long DNA during processing. These short DNA fragments produce undesirable short reads in sequencing and noise in genome mapping. Effective use of these new genomic technologies, especially for *de novo* human genome applications,[38] requires removing short DNA molecules prior to analysis. We have developed a continuous system that can filter short DNA fragments from a long DNA solution and can be readily integrated into chip-based genomic techniques.

DNA separation is conventionally performed by gel electrophoresis, where the DNA moves through a network of pores under the influence of an applied electric field.

* This chapter is based on P. Agrawal, Z. Bognár, and K.D. Dorfman, "Entropic trap purification of long DNA", Lab on a Chip **18**, 955-964 (2018).

Under certain conditions, the mobility of the DNA is a function of its molecular weight.[39] Its simplicity and long history make gel electrophoresis ubiquitous in biology labs. But this technique has some drawbacks when used upstream of genomic applications that involve long DNA. First, gel electrophoresis requires long times to separate long DNA, typically many hours, owing to the low electric fields required to prevent the orientation of DNA molecules in the direction of the electric field[40–42] and the long reorientation times during pulsed-field gel electrophoresis.[39,43] Furthermore, gel electrophoresis is a batch process using large amounts of DNA. While these masses of DNA are desirable in some contexts, single-molecule genomic methods operate with much smaller numbers of molecules. There are also challenges when integrating gel electrophoresis into the genomics workflow. Generally, the DNA recovered from gel electrophoresis are in millimeter-sized agarose gel plugs that must be converted into microliter volume liquid solutions by enzymatic digestion of the agarose gel and pipetting. This creates problems for interfacing the sample preparation technique with the genomic tool without human intervention. Moreover, pipetting the liquid solution adds variability in sample quality due to random shearing of DNA in flow.[44] Since most next-generation sequencing and mapping devices are already based on some type of microfluidic or nanofluidic system,[45–47] designing unit operations that prepare samples upstream from the genomic systems and minimize manual handling of samples will help in addressing the shortcomings of gel electrophoresis while, in principle, permitting facile integration with the genomics technologies.

Microfluidics provides a wealth of potential solutions to the aforementioned problems with gel electrophoresis for next-generation genomics sample preparation.[48] Separation of biomolecules based on the size and mobility has been accomplished by various microfluidic electrophoretic methods[49,50] where microfabrication has been used to fabricate controlled molecular sieve-like structures, such as slit-well motifs,[51] post arrays,[52] nanowires,[53] self-assembled colloidal arrays[54] and miniaturized polymeric sieving matrices.[55] Continuous filtration has been achieved using entropic trapping,[52] dielectrophoresis[56] and fluid flow via deterministic lateral displacement.[57]

For the purpose of filtering very short fragments from a long DNA sample, we propose that using a single stage of entropic trapping is a promising approach since it can provide simultaneous separation and concentration. Entropic trapping works on the principle that the long DNA must undergo conformational changes to enter a confined space and this creates an entropic barrier for their entry. This concept was first introduced to understand polymer dynamics in random porous media[58] and was later applied to gel electrophoresis to explain the low-field mobility of DNA molecules close to the size of gel pores.[59,60] In a microfluidic format, the entropic traps are formed by series of well and slit regions.[51,61–65] Many configurations of electric field profiles and slit-well motifs have been used to achieve separation of DNA,[61,65] RNA[66] and proteins.[62,63] A mechanistic understanding of these systems has been further explored experimentally[64,67,68] and computationally.[69–71] However, most systems have been designed to use hundreds of entropic traps in series to size a mixture of DNA molecules as an analytical tool, rather

than as a unit operation for sample preparation. In principle, such a system can be used as a filter by recovering the first part of the effluent containing the long DNA in one reservoir and diverting the remainder to a waste, since different size DNA will reach the end of the device at different times. However, this is a slow process because it requires time to concentrate the DNA at the injection point to create a sharp injection band, and the ensuing separation by molecular weight takes at least 30 minutes.[51]

Here we present an entropic trap approach that can filter short DNA fragments from a long DNA sample, and simultaneously concentrate the latter, to improve sample quality for genomic applications. Our device is different than previous work using entropic trapping because we do not separate the DNA by molecular weight, but rather create a bandpass filter with a single stage of entropic trapping.[51,64,72] Furthermore, our system provides a concentrated DNA plugs irrespective of the DNA concentration in the inlet feed as part of a continuous filtration process.[63] Our system is based on the principle that the mobility of short DNA across the slit-well interface can be increased dramatically when compared to long DNA molecules if the system is operated at an electric field that it is lower than the field strength required to overcome the entropic barrier for long DNA but high enough to readily allow short DNA to surmount their smaller entropic barrier. To build a continuous filtration system, we designed our system such that it decouples the injection and the filtration processes by the simultaneous use of pressure and electric potential, providing flexible operation and efficient injection of DNA into the device. Furthermore, we employed similar fabrication procedures as those used to fabricate

nanochannels to study confined DNA.[73–76] Our device could also be fabricated in silicon, making it, in principle, compatible with commercial genome mapping chips.[47] The similarity in fabrication methods will help ease the integration of this filtration system with existing genome mapping techniques. We have explored how the filtration process can be tuned by changing the filtration voltage and filtration time, demonstrating the ability to optimize the system for particular applications.

2.2 Working principle of filtration

We begin here by first outlining the basic operating principles underlying our device. The discussion below is generic, and provides guidelines for operating the device for an arbitrary mixture.

Device design

The device, illustrated schematically in Figure 2.1, consists of two microchannels connected by parallel nanoslits. The interface formed between the channel and the slit provides the entropic barrier for filtration. In contrast to entropic trapping devices used for size-based separation,[51,65,68] which typically comprise hundreds of entropic traps in series, the device in Figure 2.1 has 12 nanoslits in parallel. The two filtration zones highlighted in Figure 2.1 (main filtration and pre-concentration zone) are geometrically the same but have different roles during the filtration process, as discussed later. The device is designed to have nanoslits that are circa 90 nm deep and microchannel depths of 1 μm. The microchannels are connected at their extremities to ports for various purposes: the DNA

inlet port is used for injecting DNA into the device; long filtered DNA is sent to the DNA recovery port and short DNA fragments are shuttled to the filtration ports; and purge ports 1 and 2 are used to control DNA motion in the microchannel for continuous operation of the device. The world-to-chip connectors for these ports were configured to allow simultaneous application of hydrostatic pressure and electric potential during device operation.[77]

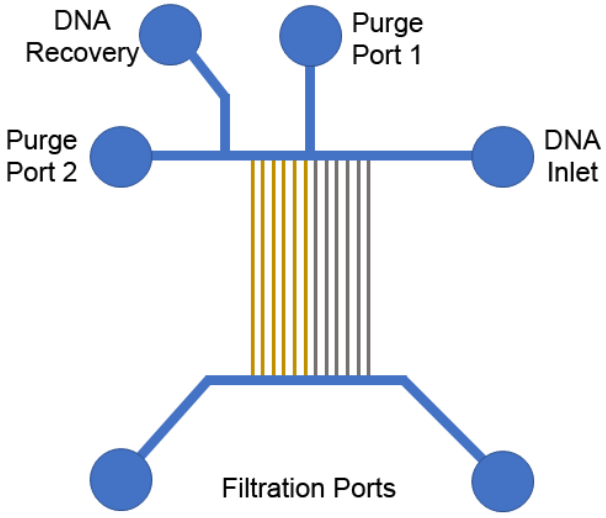

Figure 2.1 Schematic of the device. The blue regions represent microchannels. The two sets of colored nanoslits (gold and grey) represent the main filtration and pre-concentration zones discussed in Figure 2.2 and 2.3. The microchannels connecting the nanoslits are serpentine channels, seen in more detail in Fig 2.4.

Concentration of DNA at the microchannel-nanoslit interface

The device is designed to simultaneously concentrate and filter DNA at the microchannel-nanoslit interfaces. To demonstrate in a simple way how these dual effects are achieved, we constructed a resistor-based model to compute the electric potential at

each slit-channel interface, using Ohmic resistance for the channels and Kirchhoff's law at the junctions, with fixed electric potentials at each port. We assume that the resistance of a given part of the device of length L is $R = \sigma L/A$, where A is the cross-sectional area available for ionic conduction and the resistivity σ is a constant throughout the device. For the resistance calculations, the microchannels have a 1 μm depth and the nanoslits have a depth of 100 nm and a length of 1 cm. All other dimensions were similar to the mask used for device fabrication. In this calculation, the two purge ports and the DNA inlet ports in Figure 2.1 were kept at ground, while the filtration ports were given a fixed potential V_f. As the DNA is a negatively charged molecule, it moves opposite to the electric field direction, i.e. towards the higher potential. The DNA recovery port was not included in the model because, in our experiments, the potential at the recovery port is floated to minimize backflow of recovered DNA.

Figure 2.2 shows the predicted potential drop across the slits (ΔV_i) and the electric potential near each slit-channel interface within the upper microchannel (V_i). Figure 2.2b shows that, based on this model, there are two symmetric local maxima in the electric potential on either side of the central purge port 1, which is the cumulative effect of the potential drops across the serpentine microchannel connecting the two parallel nanoslits. These maxima lead to DNA accumulation because they correspond to electric potential minima for the negatively charged DNA. These concentration points arise from the current of ions from the purge and inlet ports towards the filtration ports via the nanoslits. The

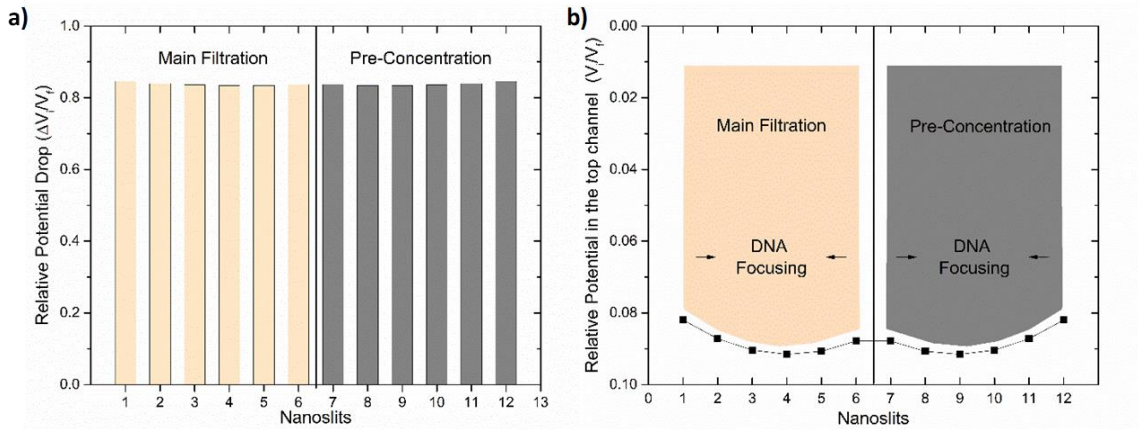

Figure 2.2 Resistor model for the device design in Figure 2.1. a) Potential drop in each slit (ΔV_i). b) Potential in the top microchannel of Figure 1 at each slit-channel interface (V_i). In both cases, the potentials are made dimensionless with the filtration voltage V_f. The six nanoslits on either side of purge port 1 are color-coded to indicate the main filtration and pre-concentration regions. The DNA recovery channel was not included in the resistor model. Note that the y-axis in (b) is plotted in reverse so that maxima in the electric potential are more easily interpreted as minima for the DNA electrostatic energy.

nanoslits are connected in parallel between the two microchannels, so the ionic current is distributed between nanoslits, leading to a non-uniform electric potential within the microchannels. Although there is a potential gradient within the microchannel, Figure 2.2a shows that the potential drop across each of the nanoslits is roughly constant. As a result, any of the nanoslits can serve as a filtration point for the DNA.

Recognizing that this resistor model may be overly simplified, we also designed a 3D COMSOL model of the device (Figure 2.3) and compared the electric potential profile from this more detailed model with that predicted by the resistor model (Figure 2.4). The COMSOL model predicts similar potential drops and two focusing zones in the device, indicating that the simple resistor model is a good approximation of the actual device

geometry.

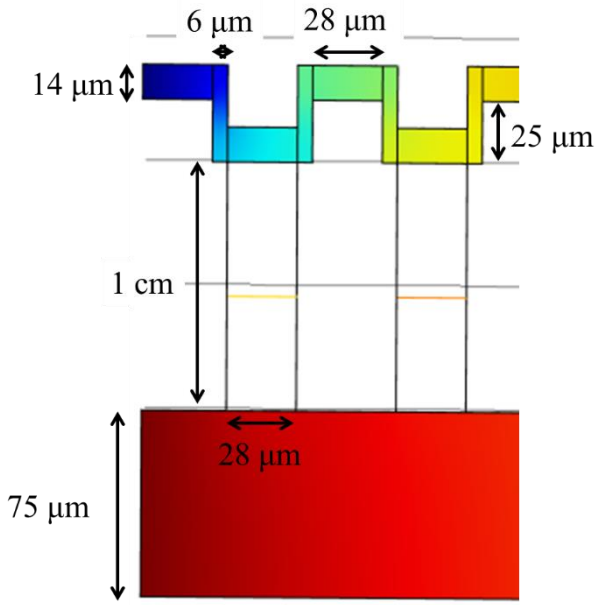

Figure 2.3 Dimensions of the microchannel and nanoslit used in the COMSOL model. Similar dimensions were used for the resistor model for comparison. There are 12 such parallel nanoslits connected by the microchannels as shown in the schematic (Figure 2.1). The device was modeled with a 90 nm deep nanoslit and microchannel depth of 1 µm.

Separation by sequential injection and filtration steps

To leverage the two filtration zones in our device, we designed an automated system to independently control the pressure and electric potential at each port. The DNA focusing regions on either side of the center purge port 1 serve as the pre-concentration and main filtration zones, with the objective to concentrate the DNA at the pre-concentration zone and then further purify the concentrated DNA mixture by subsequently transferring it to the main filtration zone. The design in Figure 2.1 constitutes a single-stage separation; the system could be modified as a multi-stage separation simply by replicating this single stage and putting the DNA recovery port as part of the last stage.

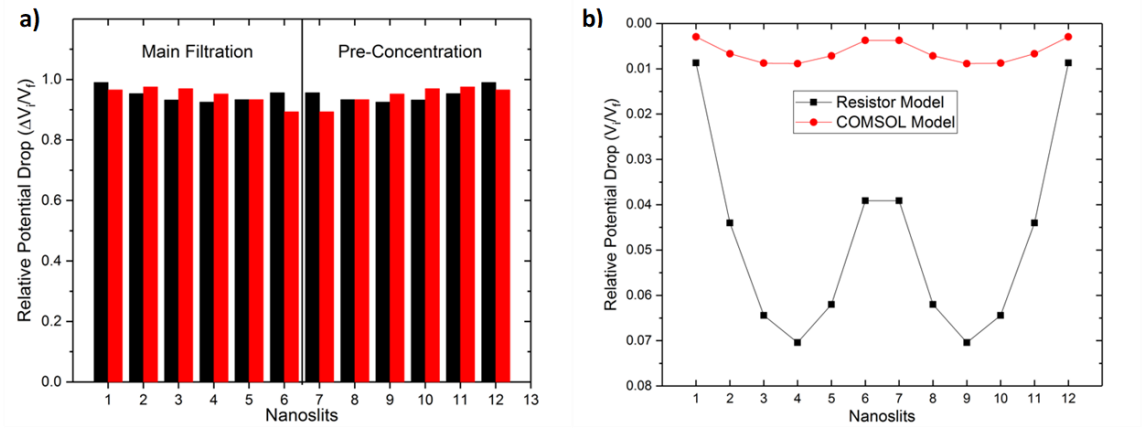

Figure 2.4 2D resistor model and 3D COMSOL model showed similar electric potentials in the microchannels and nanoslits. a) Plot of the potential drop in each slit for both models. b) Plot of the potential at each slit-channel interface in the top channel. The red data correspond to the COMSOL model and the black data correspond to the resistor model. We observe similar trends in both plots. However, the absolute values are different due to the three-dimensional effects that are incorporated into the COMSOL model. The COMSOL model focused on the filtration region and did not have the long microchannel connecting the ports to the filtration region. To make the comparison between the two models, the resistor model was modified from the main text so that it is similar to COMSOL model dimensions. As a result, the absolute values shown here are different from those of Figure 2.2.

The system was programmed to implement a sequential filtration process consisting of the injection and filtration steps shown in Figure 2.5. During the injection step, a constant air pressure (P_{in}) was applied at the DNA inlet, purge 1 and purge 2 ports, while all ports are electrically grounded. When the device is in operation, the pressure-driven flow accomplishes three aims: (i) recover the filtered DNA from the main filtration zone via the recovery channel; (ii) transfer the concentrated DNA from the pre-concentration to the main filtration zone; and (iii) inject fresh DNA from the DNA reservoir into the pre-concentration zone. We found a pressure-driven flow to be superior to electrophoresis for these steps due to the relatively low electric field in the DNA inlet reservoir, which makes

it challenging to have a high injection efficiency. Each injection step was followed by a filtration step, where a periodic pressure pulse was applied at the DNA inlet, purge 1 and purge 2 ports to help mix the DNA. At the same time, fixed electric potentials were maintained at all ports; the DNA inlet, purge 1 and purge 2 ports were kept at zero potential and the two filtration ports were kept at the filtration voltage (V_f) to provide the electric field in the slit that filters the short DNA. The DNA is focused in both zones of Figure 2.1 at one slit-channel interface and the focused DNA are filtered over time at a rate that depends on their size (Figure 2.5c). The periodic pressure provided oscillations that assisted fast focusing of DNA in the main filtration zone while keeping them within the trap created by the potential gradient illustrated in Figure 2.2b.

With the help of our continuous system, both the injection and filtration steps were repeated sequentially to achieve continuous filtration of the DNA sample. In this mode of operation, the DNA recovery channel is a crucial part of the design. The recovery port was kept at a floating potential, whereupon those DNA molecules that entered into the recovery channel during the pressure-driven injection step are not pulled back into the filtration zone during the electrophoresis-based filtration step. As a result, the device produces pulses of concentrated long DNA at the outlet.

Tuning the separation performance

The operation of the filter device is understood as the balance between two time scales.[78] The first time scale is the residence time for the DNA at the interface between the

microchannel and the nanoslit. To a first approximation, the residence time is given by the duration of the filtration step t_2 in Figure 2.5b. This estimate is an upper bound, as the DNA molecules require time to be transported to the interface when the voltage is applied. Moreover, the residence time differs between DNA molecules due to their different initial positions at the start of the filtration step. However, the residence time should be independent of molecular weight to a first approximation, since the free-solution electrophoretic mobility of DNA is independent of its size for molecules larger than 400 base pairs.[79,80] If anything, a size-dependent mobility, if were present, would enhance the filtration effect because it would slow the rate at which the longer DNA accumulate at the interface.

The second time scale is the characteristic time for escape over the entropic barrier. The entrapment time τ of long DNA has been modeled with an equation,[64,67,81]

$$\tau = \tau_0 \exp(\alpha / E_s kT) \quad (1)$$

where τ_0 and α are parameters that depend on the size of the molecule, E_s is the electric field strength in the slit and kT is the thermal energy. The prefactor τ_0 represents the frequency of attempts to escape an entropic trap. Prior work suggests that τ_0 is inversely proportional to the size of the DNA molecule because larger molecules present a larger cross-section at the interface, and thus have more opportunities to insert a hairpin into the slit.[61,64] Equation 1 has been applied to model long DNA, and it is likely an overestimate

of the trapping time for short DNA.[64] The other parameter α, is related to the free energy barrier for moving the polymer from the very weak confinement of the microchannel to the strong confinement of the nanoslit in the tilted potential energy landscape provided by the applied electric field. Simulation work suggests that α depends on the molecular weight of the DNA at low and moderate electric fields; larger DNA experience a higher entropic penalty due to the reduction in conformational phase space upon entry into the slit.[70] At

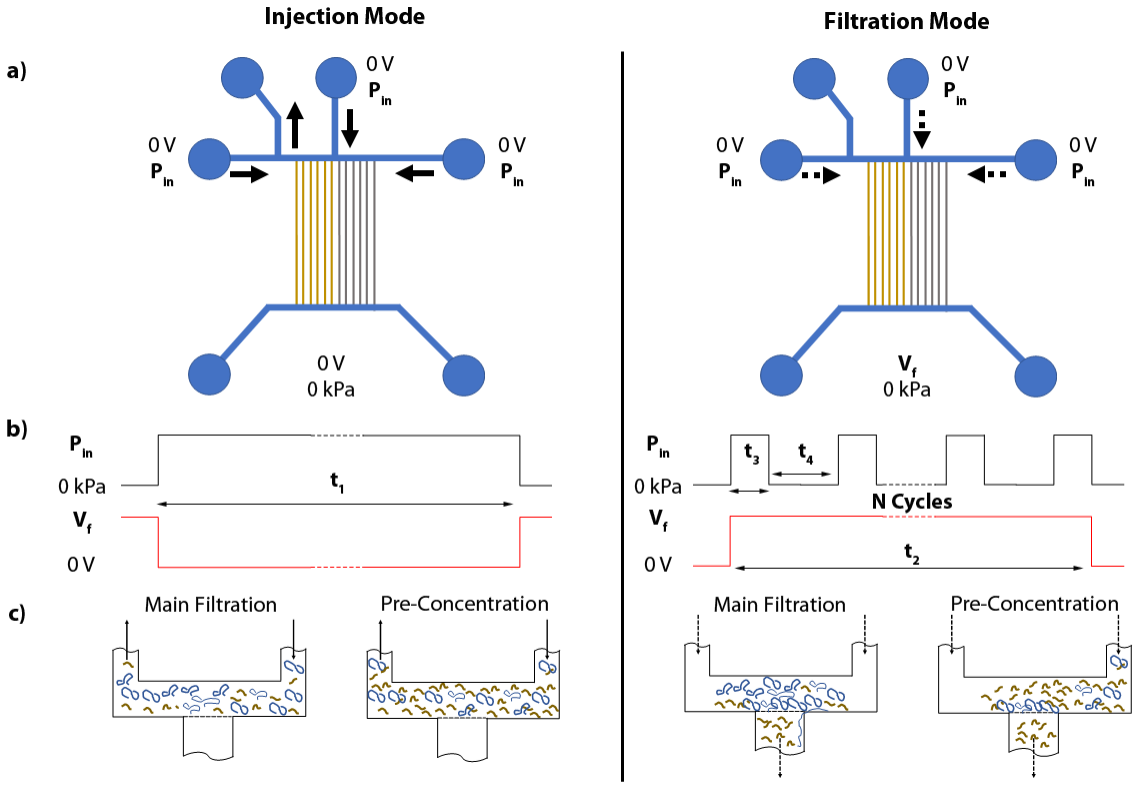

Figure 2.5 Procedure to operate the device. Sequential injection and filtration modes correspond to changes in the pressure and voltage at each port. a) Values of the pressure and electric potential at each port during a cycle. b) Schematic of the pressure and potential profile applied at each port during the two modes of operation. The pressure shown in the figure is the gauge pressure. c) Schematic of a potential use of the device to filter DNA mixture of short and long DNA molecules in the two filtration zones (main-filter and pre-concentration) during the two modes of operation. The pre-concentration zone continuously receives DNA from the inlet reservoir.

higher electric fields, α becomes independent of molecular weight for large DNA because its magnitude is governed by the entropic cost for inserting a "beachhead" of DNA into the nanoslit; the strong electric field then sucks the rest of the DNA into the slit.[69] If the entire size of the DNA is smaller than this beachhead, then α should remain a function of molecular weight for all electric field strengths.

The remarkable feature of entropic trapping as a size-based separation is that the longer DNA elute first from the device because, under the relatively high electric fields used in those experiments, the dependence of τ on τ_0 is more important than the dependence on α.[64] However, at sufficiently low electric fields, the parameter α will become the most important factor in governing the escape time because it appears in the exponential. Indeed, previous studies suggest that there should be a sufficiently small electric field for which the entrapment time will be essentially infinite, i.e. DNA can be completely trapped at the slit-channel interface.[64,67] In our experiments, we always observed finite entrapment time for long DNA at any filtration voltages that are sufficient to drive the DNA to the nanoslit-microchannel interface in a reasonable period of time.

The filtration performance of our device can be tuned by considering the ratio of the two relevant time scales,

$$\beta = t_2/\tau \qquad (2)$$

for a given DNA size. If $\beta \gg 1$, then that size DNA should escape through the entropic trap and be filtered out. Most of the previous studies involving DNA separations using entropic traps trivially satisfy $\beta \gg 1$ because all of the DNA molecules cross the first slit.[51,67,68] Conversely, if $\beta \ll 1$, then most of the DNA with that size should be retained in the microchannel and eventually shuttled to the DNA recovery port during the subsequent injection step. However, the intrinsic physics embodied by Eq. (1) implies that a single entropic trap will not provide an infinite selectivity since β is always finite and non-zero. Moreover, it is worth noting that β represents the characteristic time for the distribution of trapping times; even for $\beta \ll 1$, some of the molecules will still escape.

2.3 Material and methods

Device Fabrication

The device fabrication follows the standard protocols for creating entropic trap devices outlined in Figure 2.6.[65,73] Briefly, both the microchannels and nanoslits were patterned in S1813 photoresist (Shipley) using optical lithography followed by reactive ion etching using a mixture of $Ar/CF_4/CHF_3$ to transfer the patterns into a 4-in. diameter, 0.5 mm thick fused silica substrate (University Wafer). The etch depth for the nanoslits and microchannels were controlled by optimizing the etching duration for each layer to achieve desired depths. The channel depths were quantified using a profilometer (KLA-Tencor P7). Final devices were further characterized with scanning electron microscopy (SEM, JEOL 6610). After dicing the nine devices with a wafer saw (Disco DAD 2H/6T), access holes

for the ports were sand blasted (Danville). The completed substrate was then RCA-cleaned and thermally bonded to a 170 μm coverslip in a 1000 °C furnace (Thermo Fisher).[73]

Nine devices were fabricated on each wafer. Ideally, each device has the same channel depth, but the variability in gas concentration inside the etching chambers caused some variation in the channel depth between devices. This variation in our system ranged

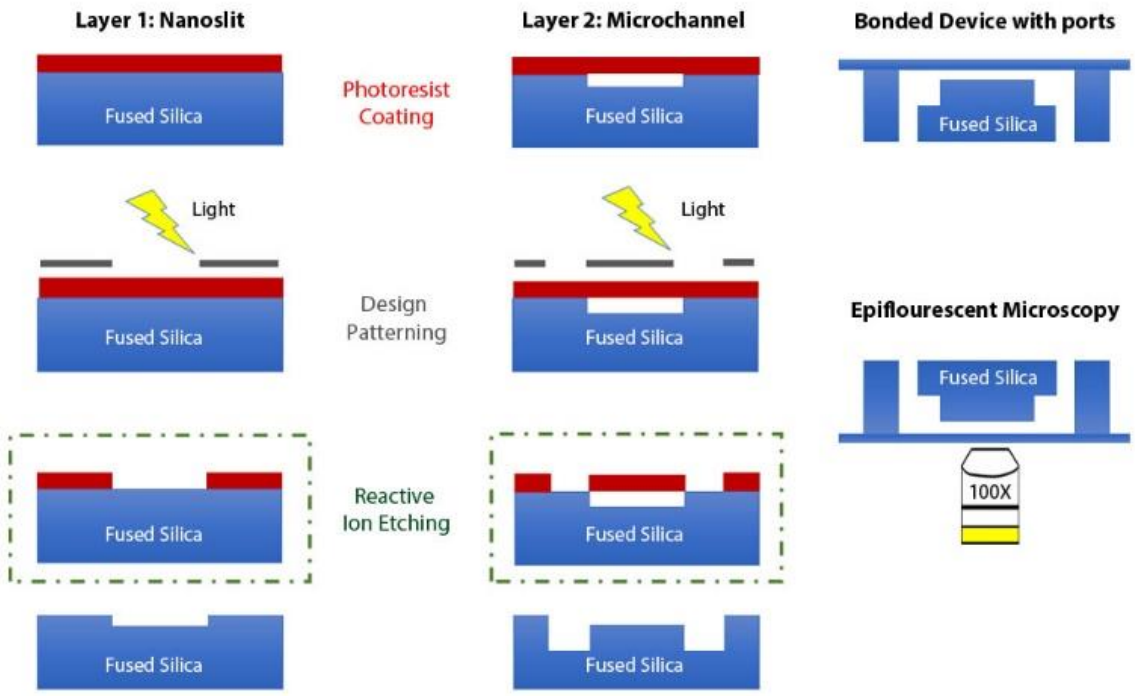

Figure 2.6 Steps involved in the fabrication of the device.

from 88 nm to 103 nm for the nanoslits and 906 nm to 936 nm for the microchannels between different devices. The filtration experiments discussed below used a device with a nanoslit depth of 88 nm and microchannel depth of 906 nm. Figure 2.7 shows the profilometer profile for this device. The integrity of the final fabricated device was further verified using SEM.

Sample Preparation

Our experiments use two model systems: λ DNA (48.5 kilobase pairs, kbp, New England Biolabs; $R_g \approx 750$ nm) as a prototypical long DNA molecule and 2 kbp DNA sample (New England Biolabs; $R_g \approx 100$ nm) as a model short DNA contaminant.[82] The DNA was stained with YOYO-1 fluorescent dye (Invitrogen) at a concentration of 1 dye molecule per 10 base pairs (bp) for λ DNA, and 1 dye molecule per 5 bp for 2 kbp DNA.[83] The stock DNA solution was prepared in 1X TBE buffer solution. For the experiments, the sample solution was prepared in 4X TBE buffer supplemented with 3% (w/v) 40 kDa polyvinyl pyrrolidine (Sigma-Aldrich) and 6% (v/v) β -mercaptoethanol (BME, Sigma-Aldrich). The final solution for all experiments had a DNA concentration of 3 μg/ml.

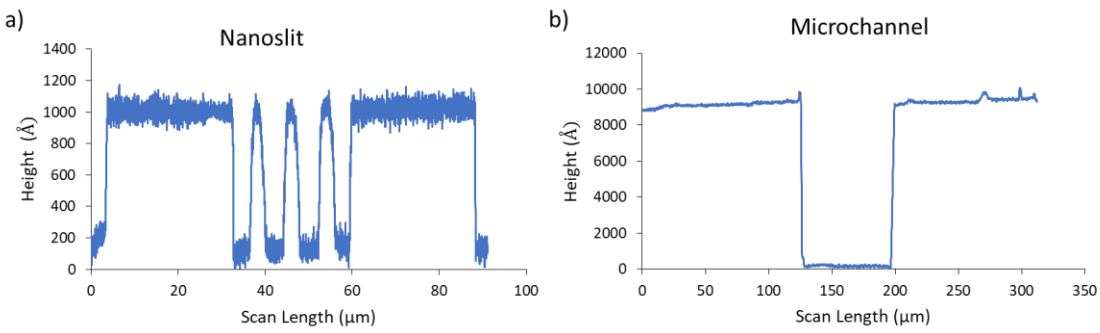

Figure 2.7 Profilometer data for the a) nanoslit and b) microchannels for the device used to produce the separation data in the main text.

Experimental procedure and quantification

The filtration device was mounted on a custom-built chuck that contains reservoirs for buffer solution as well as connections to simultaneously apply the hydrostatic pressure

and electric potential at each port. The filtration process for each DNA molecule was recorded with a sCMOS camera (ANDOR Zyla 4.2) using a 100x (1.4 N.A.) oil immersion objective on an inverted epifluorescence microscope (Leica DMI 4000B) with a 120 W metal halide source. Micro-Manager was programmed to synchronize the stage movement and camera recording during the filtration process.[84,85] The air pressure and electric potential at each port were independently controlled using a LabVIEW program (National Instruments). For these experiments, all pressure related steps were performed at a gauge pressure of 2.5 kPa. The injection time (t_1) was set as 35 s, which we found was sufficient for the filtered DNA to leave the main filtration region and the concentrated DNA to move from the pre-concentration region to the main filtration region. The short pressure pulse (t_3) was applied for 2 s, with a delay (t_4) of 28 s between the two pressure pulses. The operating pressure, injection and pulse time can be further optimized but were not evaluated in this work. The filtration process was quantified by measuring the decrease in the fluorescence intensity at the slit-channel interface during a filtration cycle. The final percentage decrease in the fluorescence intensity was averaged over two filtration cycles for each filtration condition.

Device performance

Figures 2.8a and 2.8b show scanning electron microscopy (SEM) images of a section of a completed device. The serpentine shape of the microchannels was designed to produce a potential drop within the microchannels in a compact geometry. Note that the

microchannel potential drop is required to produce the focusing predicted by Figure 2.2 and the COMSOL model.

Figures 2.8c and 2.8d show the basic operation of the device. In Figure 2.8c, we show the main filtration zone as it is filled with λ DNA molecules just after the injection cycle of Figure 2.5. Figure 2.8d then shows how these DNA molecules are concentrated at the completion of the filtration cycle of Figure 2.5. The pressure pulse for the DNA oscillation in the filtration cycle shifted the focusing of DNA in the direction of the pressure

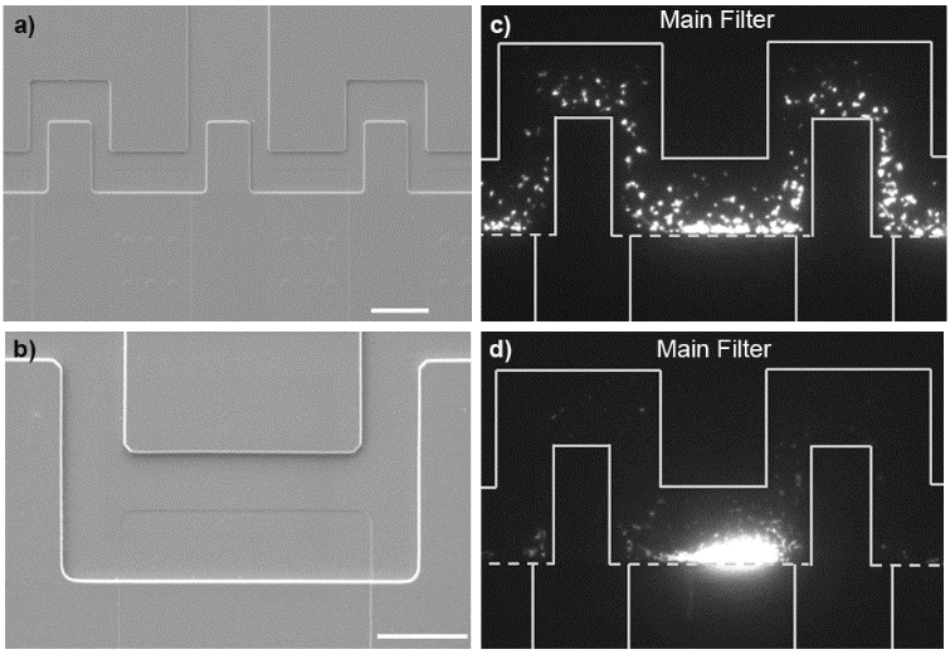

Figure 2.8 Validation of device fabrication and operation. a) SEM image of the upper microchannel near the center purge port 1 channel (Scale bar 20 μm). b) SEM image of the final slit-channel interface that provides the entropic barrier for filtration (Scale bar 10 μm). c) Fluorescent image of λ DNA molecules in the main filtration region near the third slit just after the completion of the injection cycle. d) Fluorescent image of the λ DNA just before the completion of the filtration cycle with the molecules trapped at the slit-channel interface. The white lines in (c) and (d) are included to indicate the channel boundaries, which are not visible in fluorescence images.

pulse, i.e. the DNA mostly focused on the third slit rather than the fourth slit predicted by the purely electrophoretic model in Figure 2.2b. However, the pressure pulse does not cause the DNA to jump to a new microchannel-nanoslit interface during the filtration step. Rather, it simply mixes the DNA at the interface to aid in filtration.

One possible concern in our device is the possibility of migration of the DNA away from the walls due to the shear flow produced by the pressure pulses.[86] However, we did not observe any significant impact of lateral migration during the filtration process. We attribute this outcome to two aspects of our system. First, during the filtration cycle, both the filtration zone and the concentration zone operate predominately under the influence of the electric field, with a small pressure pulse used to mix the DNA within the potential well created by the non-uniform electric field within the microchannel. These pressure pulses (duration t_3 = 2 s) may not be long enough to develop a steady-state depletion layer near the wall. Second, as the DNA are focused near the slit-channel interface and form a DNA plug (as shown in Figure 2.8), the higher solution viscosity near the wall (created by the concentrated DNA plug) and screening of hydrodynamics near the wall at finite concentration, should further reduce the migration effect. While we suspect that lateral migration has a negligible effect on our separation, enhancing its role could aid the filtration process. Based on theory, the flow-induced depletion length will be larger for long DNA as compared to the short DNA.[86] This implies that the long DNA should move away from the wall more than the short DNA, and thus reduce their escape attempt

frequency at the nanoslit entrance. The net effect is to increase the β for short DNA when compared to long DNA and assist the filtration.

We designed the device here for proof-of-concept experiments using pure 2 kbp and 48.5 kbp DNA separately. This separation is considerably more challenging than our targeted application in genome mapping, where the large DNA molecules are in excess of 150 kbp, and thus provides a very stringent test of the principles underlying the filtration device. These experiments, albeit more labor-intense than studying a mixture, allow us to quantify the filtration of short and long DNA molecules, respectively, without concern about spectral overlap and possible exchange of fluorescent dyes between molecules in a two-color experiment.

The device was designed with a slit height close to the radius of gyration of the short DNA, but much smaller than that of the long DNA. The configurational degrees of freedom for the short DNA are not significantly reduced by entry into the shallow region, implying that they do not have much of a partition between the shallow and the deep region and that α is relatively small. On the other hand, the long DNA molecules encounter a configurational entropy barrier associated with the deformation of the molecule in order for it to enter into the shallow region, whereupon α is relatively large.[71] We thus expect to observe different values of β for these two species. The slit height is a key aspect in the device design, and it can be tuned to set the filtration cut-off at different molecular weights.

Like most filtration processes, our system entails a trade-off between selectivity and recovery of the filtrate. From Eqs. (1)-(2), our discussion of device tunability suggests two different approaches to alter β: (i) changing the filtration voltage, which affects τ through changes in the electric field in the slit, E_s; and (ii) changing the filtration time, t_2. We consider each of these approaches separately in what follows.

Effect of changing filtration voltage

In our initial set of experiments, we examined the performance of the device at filtration voltages of 10 V, 12 V, and 14 V while fixing the filtration time at 600 s. Figure 2.9 shows how the fluorescence intensity at the nanoslit-microchannel interface (Figure 2.8d) changes as a function of time for these conditions using either 2 kbp DNA (Figure 2.9a) or λ DNA (Figure 2.9b). These plots present the average of the fluorescence intensity over injection/filtration cycles in a single experiment, and these data correspond to the fluorescence intensity in the main filtration zone of Figure 2.1. We chose to study the main

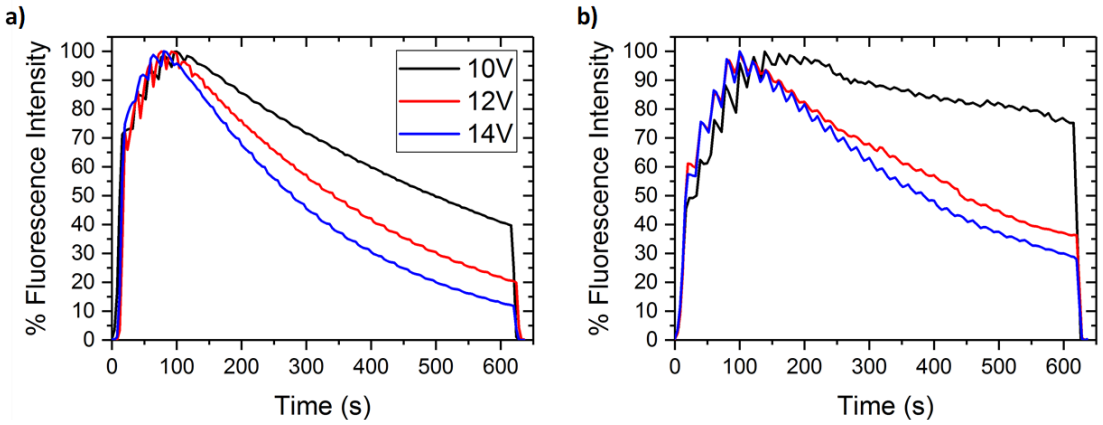

Figure 2.9 Percentage recovery of DNA for the filtration time of 600 s at different filtration voltages for a) 2 kbp and b) λ DNA molecules. Each filtration profile is an average of two filtration cycles. The color coding is the same for both panels.

filtration zone, rather than the pre-concentration zone, because the initial condition for the main filtration zone is the total amount of DNA to be filtered; for the pre-concentration zone, the filtration step involves a combination of filtration and continued injection and concentration of DNA from the loading reservoir, making it challenging to deconvolve the role of these two effects on the total fluorescence intensity.

It is clear from the data in Figure 2.9 that the fluorescence intensity of the shorter DNA is decreasing as it is filtered through the device. In contrast, the longer DNA are retained at the slit. However, as noted in the context of Eq. (1), there is a finite escape time for the long DNA. Thus, as we run the filtration for a longer period of time, the longer DNA eventually begin to escape over the barrier.

To convert the data in Figure 2.9 into a quantitative metric for the device performance, we defined the filtration efficiency to be proportional to the percentage of DNA (% fluorescence intensity) left in the main filtration zone at the end of the filtration cycle. For example, in case of 12 V, we recovered more than 40% of long DNA as compared to 20% recovery of short DNA when operated at the same condition.

We repeated the experiment in Figure 2.9 multiple times, and the results are summarized in Table 2.1. The fluorescence intensity profiles for the data in that table appear in Figure 2.10. When the separation was performed on different days for the same operating conditions, the percentage recovery of long DNA between trials varied by up to 15%. The corresponding day-to-day variation for small DNA molecules was 5% or less.

The variability in filtration, however, decreased with increasing filtration voltage. As such, the variability in the filtration of the large DNA may be attributed to the fluctuation in the mobility of DNA and the frequency of barrier hopping at relatively low electric fields. Previous studies have also reported mobility variations as large as 15%.[67,87] These works tend to suggest that the variation in the mobility is more prominent at low electric fields and in the buffer solution with PVP. Both of these conditions exist in our system.

Table 2.1 Percentage recovery of DNA molecules different trials and averaged DNA recovery for two DNA types as well as the selectivity of filtration at 600 s filtration time for different filtration voltages. Electric field in slit 3 was calculated for each filtration voltage using the resistor model shown in Figure 2.2.

Filtration Voltage (V)	**Electric Field (V/cm)**	**λ DNA (%)**			**2 kbp DNA (%)**	
		Trial 1	Trial 2	Trial 3	Trial 1	Trial 2
10	8.75	60	75	46	30	40
12	10.50	58	37	45	20	20
14	12.24	41	29	36	8	12

Filtration Voltage (V)	**Electric Field (V/cm)**	**Average recovery (%)**		**Selectivity**
		λ DNA	**2 kbp DNA**	
10	8.75	60	35	1.7
12	10.50	41	20	2.1
14	12.24	35	10	3.5

The amount of short DNA removed from the solution increased from 60% to 90% on increasing the filtration voltage from 10 V to 14 V. This, in turn, increases the selectivity of filtration of short DNA as compared to long DNA in Table 2.1. But the improved selectivity comes at the expense of losing more λ DNA molecules with increasing filtration voltage. The recovery of λ DNA decreased from 60% to 40% with an increase in the filtration from 10 V to 14 V, consistent with our discussion of device tunability via Eqs. (1)-(2).

Table 2.2 Percent recovery of individual DNA molecules for 600 s and 450 s filtration as well as the anticipated recovery at 450 s based on the filtration profile from 600 s filtration time. Electric field in slit 3 was calculated for each filtration voltage using the resistor model shown in Figure 2.2.

	Filtration Voltage (V)	**Electric Field (V/cm)**	**Percentage recovery (%)**		
			600 s	450 s (Prediction)	450 s (Actual)
2 kbp DNA	12	10.50	20	35	36
	14	12.24	12	25	25
λ DNA	12	10.50	45	59	58
	14	12.24	37	48	54

Effect of changing filtration time

The second approach to control β is to control the duration of the filtration cycle. Figure 2.11a shows the filtration profile of 2kbp and λ DNA, separately, for two different filtration times at a filtration voltage of 12 V. The fluorescence intensity profiles for the

two different filtration times nicely overlap on each other for both DNA sizes, indicating a high reproducibility within a given experiment. As a result, a filtration profile obtained for a large value of t_2 should predict the filtration efficiency for shorter filtration time. Table 2.2 summarizes the effectiveness of this approach, using the data obtained for a 600 s

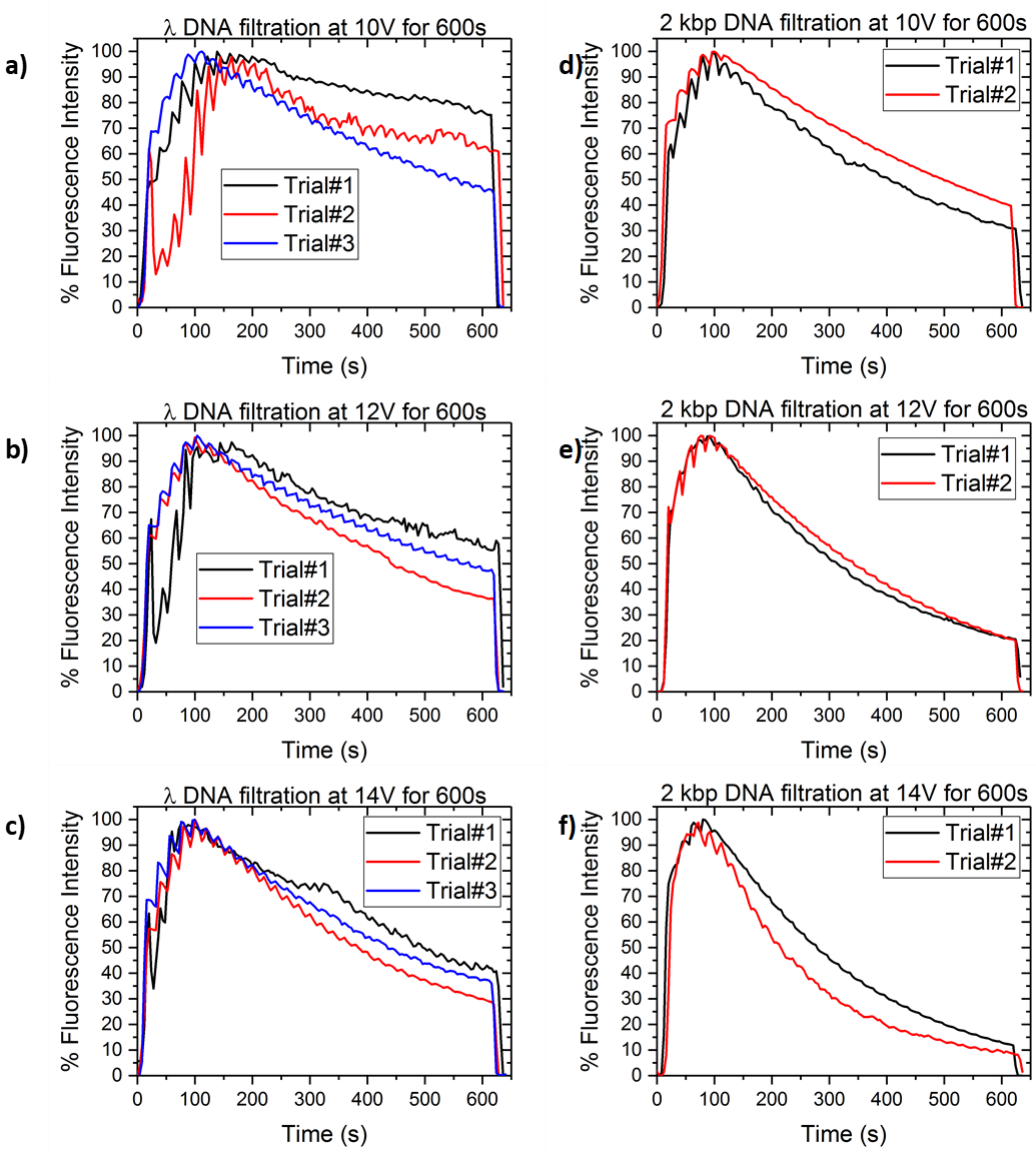

Figure 2.10 Different trials for the filtration of λ DNA (a-c) and 2 kbp DNA (d-f) at 600 s filtration time for various filtration voltages. The final percentage fluorescence intensity of these trials are tabulated in Table 2.1.

filtration time to predict the result for a 450 s experiment. The additional data for a filtration voltage of 14 V appear as Figure 2.12. Despite the variation in the mobility for different trials that we observed in Table 2.1, a similar recovery and overall filtration curves were obtained for the two different filtration times.

Having demonstrated separately the two approaches for controlling β, i.e. filtration voltage and filtration time, we further computed the predicted selectivity profiles (Figure 2.11b) for the filtration of λ and 2 kbp DNA at different filtration times for 12 V and 14 V, based on the data presented in Figure 2.10 and Table 2.1. The data in Figure 2.11b were obtained by taking the ratio of average fluorescence intensity for λ and 2 kbp DNA molecules at different filtration times. For each DNA size, the average fluorescence

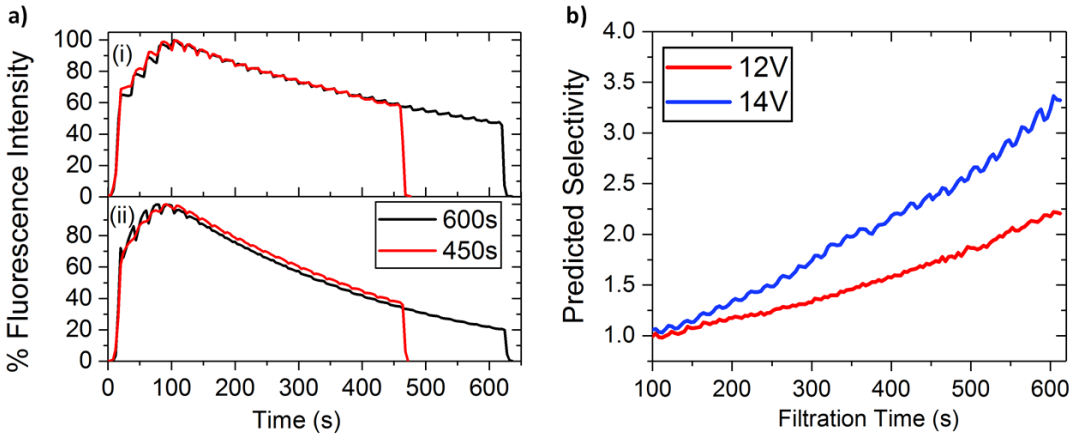

Figure 2.11 a) Percentage recovery of DNA for the filtration voltage of 12 V at different filtration times for i) λ DNA and ii) 2kbp DNA molecules. Each filtration profile is an average of two filtration cycles. The color coding is the same for both panels. b) Predicted selectivity profile for the filtration of λ DNA over the 2kbp DNA. The average fluorescence intensity profile for λ DNA and 2 kbp molecules used to obtain the selectivity at a particular filtration voltage is the average of three separate trials for λ DNA and two separate trials of 2 kbp DNA respectively, shown in Figure 2.10

intensity for particular filtration voltage is computed from the ensemble of all the independent trials.

Figure 2.11b shows that for a particular filtration time, the selectivity increases with increasing filtration voltage and there is a higher selectivity for longer filtration times at a fixed filtration voltage. There is a small difference between the selectivity values at 600 s in Figure 2.11b and Table 2.1. This difference arises from the need to manually align the filtration profiles between different experiments for all filtration times to compute the average intensity profiles and selectivity. Overall, these results demonstrate the ability of our system to tune the filtration quality by balancing between the selectivity and recovery efficiency depending upon the need of the application.

2.4 Conclusions

We have designed and fabricated a filtration device that can preferentially remove the small DNA molecules from a DNA solution to improve the sample preparation for a genomic application. The filtration system operates as an automated injection-filtration process that concentrates and purifies the long DNA solution before a downstream application. The device operates continuously, producing plugs of concentrated long DNA at its outlet. The selectivity and recovery in the device are understood as the balance between the residence time at the nanoslit-microchannel interface and the escape time through the entropic trap. For a given slit depth, the device performance can be tuned by either changing the duration of the filtration step or the filtration voltage. For proof-of-

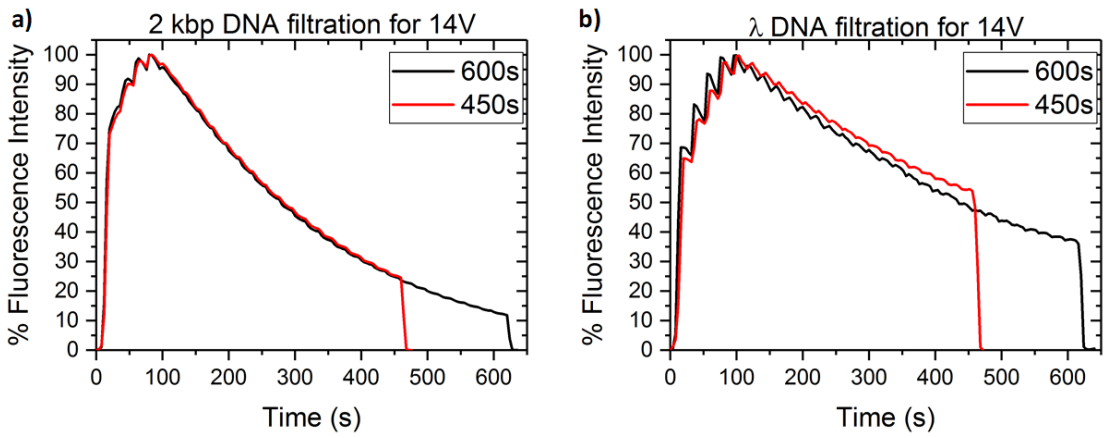

Figure 2.12 Data used to compute the percent recovery of DNA for the filtration voltage of 14 V at different filtration times for a) 2 kbp and b) λ DNA molecules. Each filtration profile is an average of two filtration cycles.

concept purposes, we used pure 2 kbp and λ DNA molecules to characterize the filtration process for our system. Moving forward, we envision this system as a short pass filter with a desired cut-off DNA size depending upon the application's needs. The device can be optimized for a desired cut-off size by adjusting the design and operating parameters, including the slit count and the height of each slit.

This work provides an important unit operation to improve the overall performance of genomic techniques, especially for genome mapping. Future work will focus on applying this system for genome mapping in nanochannels, where this filtration device is incorporated upstream of the nanochannel system to provide an integrated system.

Chapter 3 – Fast, efficient and gentle transfection of human adherent cells in suspension

3.1 Introduction

The cellular delivery of genetic material is a valuable tool for many fields of biology such as genetics, biochemistry, molecular and developmental biology, and regenerative medicine. The last decade has seen rapid development in these fields. For example, the discovery of factors that allow generation of iPSCs from somatic cells[88] and the ability to engineer the cellular genome with high specificity[89] have transformative potential for personalized medicine. These and other biomedical research fields are reliant upon the successful delivery of nucleic acids into primary and immortalized cells, which requires (i) a delivery system that packages nucleic acids into nano/micro-particles,[90] followed by (ii) transport of the cargo to the cell surface and attachment to the plasma membrane, and finally (iii) internalization, intracellular trafficking and release of genetic material at a target intracellular location, typically the nucleus.[91,92] Many viral and non-viral gene delivery vehicles (GDVs)—with variable delivery efficiency and cell specificity—are available for the first step of this process to package genetic material of interest.[90] For laboratory investigations, commonly used non-viral GDVs involve cationic lipids or polymers. These are particularly attractive as they can be rapidly prepared with various nucleic acid types (such as, mRNA, miRNA, lncRNA, shRNA, DNA) of different

* This chapter is based on P. Agrawal, N.P. Ingle, W.S. Boyle, E. Ward, J. Tolar, K.D. Dorfman, and T.M. Reineke, "Fast, Efficient, and Gentle Transfection of Human Adherent Cells in Suspension", ACS Appl. Mater. Interfaces **8**, 8870–8874 (2016).

sizes, combinations, and sequences.[90,93] Furthermore, producing these materials is inexpensive and scalable.[90] For adherent cells, the second step, endocytosis, typically involves plating a monolayer of cells, allowing cells to grow to near-confluency, and then exposing them to the GDV solution for several hours (commonly referred to as the transfection time). This step is limited by slow transport of GDV particles, variable rate of particle delivery to membrane in cell-cell contacts versus medium-exposed surfaces of the plated cells, and—critically— cytotoxicity.[91,92,94] These limitations make cellular membrane transport an attractive target for improvement of the speed and efficiency of transfection in adherent cells.

The similarities between GDV procedures and chemical reactor design for heterogeneous reactions suggest that the conventional transfection procedures can be significantly optimized. In particular, heterogeneous reactions are enhanced in slurry reactors, where the catalyst particles are in suspension.[95] The challenge in applying this approach to gene delivery is that adherent cells stop dividing and undergo apoptosis when kept in suspension for an extended period of time.[96] However, physical transfection methods, such as electroporation or nucleofection, succeed because the cells are kept in suspension for small durations.[97] Therefore, we should be able to deliver GDV particles in suspension if the adhesion of the particle to the cell membrane occurs faster than the biological time scale for cell death. To this end, we propose a new suspension-based method to improve transfection efficiency of human induced pluripotent stem cells (iPSCs), primary cells, and immortalized cell lines. After the delivery process—achieved

in suspension—is complete, cells can then be plated for further culture expansion, or, if prepared in clinical grade, delivered to the patient.[98] The innovation in our solution is recognizing different time scales in the delivery process; the GDV particles adhere to the cell surface in a much shorter time than it takes for them to cross the cellular membrane. This is based on the fact that cells take-up these particles through various endocytic pathways and have to undergo internal dynamic trafficking, which is both cell and GDV dependent.[99] In contrast, attachment of GDV particles is usually due to non-specific interactions between membrane proteins and GDV particles. We employed bulk and microfluidic systems to understand how the exposure time of GDVs to the cell surface, spanning from seconds to hours, affects the overall delivery of nucleic acid to cells.

3.2 Materials and Methods

Cell culture

Human cervical adenocarcinoma (HeLa) cells (American Type Culture Collection, Manassas, VA), primary human dermal fibroblasts from neonatal foreskin (HDFn; Life Technologies, Thermo Fisher Scientific Inc., Carlsbad, CA), and adult primary fibroblasts (PFB) were cultured in DMEM (Life Technologies, Thermo Fisher Scientific, Inc., Carlsbad, CA) supplemented with 10% FBS (Life Technologies, Thermo Fisher Scientific, Inc., Carlsbad, CA) and 1% AB/AM (Life Technologies, Thermo Fisher Scientific Inc., Carlsbad, CA) at 37˚C and 5% CO_2. The HDFn were additionally supplemented with 1 μL/mL EGF and 1 μL/mL FGF (PeproTech, Inc., Rocky Hill, NJ). The cells were cultured in 75-cm^2 flasks and passaged at least once a week. All cells were confirmed to be

mycoplasma free using a MycoAlert™ Mycoplasma Detection Kit (Lonza Group Ltd., Walkersville, MD).

Induced pluripotent stem cells (iPSCs) derived from naïve T cells were cultured on Matrigel® (Corning) in mTeSR™1 (STEMCELL Technologies, Vancouver, BC, Canada) media. Cultures were maintained in 6-well plates. Media was changed daily, and cells were passaged at a ratio of 1/6 every 5 day, by gently scraping them from the well surface after incubating in PBS (Life Technologies, Thermo Fisher Scientific Inc., Carlsbad, CA) for 5 minutes. iPSCs were confirmed mycoplasma negative by PCR assay.

GDV particle preparation

GDV particles were formulated by complexing pDNA with transfection reagents FugeneHD (Promega Corporation, Madison, WI) and Glycofect (donation from Techulon Inc., Blacksburg, VA). Briefly, to make GDV particles with FugeneHD, 3 μl of FugeneHD per 1 μg pDNA was used and incubated for at least 15 min. For Glycofect, the GDV particles were complexed with pDNA at 20 N/P ratio (N/P ratio implies the number of secondary amines on the polymer backbones to the number of phosphate groups on the nucleic acid backbones to form the GDV particle solution)[100] and incubated for 60 minutes. Cy5-labeled pCMV-lacZ (7.1kb; PlasmidFactory GmbH & Co. KG, Bielefeld, Germany), using Label IT® Nucleic Acid Labeling Kit (Mirus Bio, LLC., Madison, WI), was used to quantify attachment of the transfection reagents to the cell surface by measuring Cy5-positive cells and for the gene expression assay, pZs-Green plasmid (3.3 kb; Clontech

Laboratories Inc., Mountain View, CA) was used to detect GFP-positive cells. For Glycofect systems, GDV particles were formulated in DNase/RNase-free water (Life Technologies, Thermo Fisher Scientific Inc., Carlsbad, CA) for bulk experiments, but for microfluidic device experiments, 5% dextrose sugar in water (Hospira Inc., Lake Forest, IL) was used instead of pure water to avoid cell lysis. For FugeneHD systems, GDV particles were prepared in OptiMEM (Life Technologies, Thermo Fisher Scientific Inc., Carlsbad, CA) solution for all experiments. The negative control samples in the experiments are denoted as "Cell only", without any pDNA, or transfection vehicles and "pDNA only" with only free pDNA, without any transfection reagent, prepared in media similar to the GDV particle solution. All experiments were performed in triplicate, which are used to assess the error for each condition.

Microfluidic device experiment

Device prototyping:

PDMS-glass hybrid microfluidic device was fabricated using the standard rapid prototyping and replica molding techniques, as described previously[17,101,102]. Briefly, the SU-8 structure was patterned on 4" silicon wafer (Nanofabrication Center, University of Minnesota, Minneapolis, MN) by using SU8-2050 negative photoresist (MicroChem, Inc., Santa Clara, CA). A pre-mixed 10:1 mixture of polydimethylsiloxane (PDMS) pre-polymer and a curing agent solution (Sylgard184 kit; Dow Corning Corporation, Midland, MI) was poured over the patterned silicon wafer and cured at 70°C for at least 2 hours. The PDMS mold was peeled off from the wafer and holes were punched into the PDMS with 1

mm biopsy punch (Paramount Surgimed Ltd., New Delhi, India) to form the inlet and outlet of the device. PDMS replica was then bonded with the glass after plasma treatment using a plasma reactor (PDC-32G, Harrick Scientific, Pleasantville, NY). All channels in the device are 100 μm wide and ~70 μm deep. The fabrication workflow is outlined in Figure 3.1.

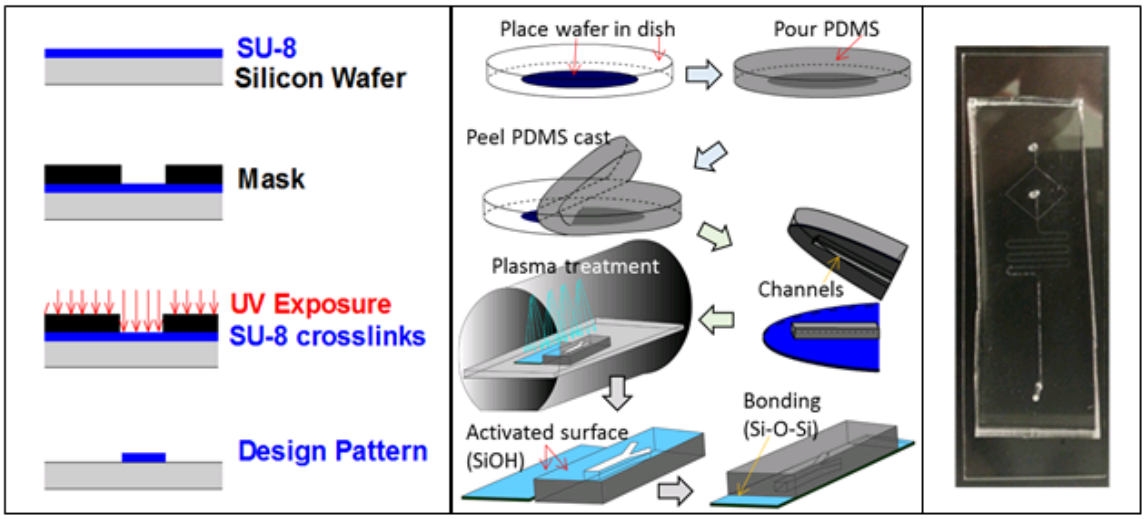

Figure 3.1 Schematic of device fabrication: a) Fabrication of a negative mold of SU8 on a silicon wafer; b) Casting of a PDMS replica on the negative mold and bonding of the PDMS channel to glass slide using plasma treatment; c) Image of the microfluidic device.

Prep-work:

All the microfluidic supplies such as gastight glass syringes (SGE Analytical Science, Trajan Scientific Americas Inc., Austin, TX), Tygon tubing (Component Supply Co, Florida), and the device were thoroughly washed with three times as follows: (1) water, (2) 10% bleach, (3) water, (4) ethanol (190 proof), and (5) water. The complete setup was then filled with 7.5% BSA (bovine serum albumin) solution and incubated for 30 minutes. A new device was used for each experiment.

Next, to make the cell suspension, the cells in flasks were first washed with PBS, then trypsinized using trypsin-EDTA (Life Technologies, Thermo Fisher Scientific Inc., Carlsbad, CA) and later neutralized by DMEM. This cell suspension was then centrifuged at 1000 rpm (201 X g) at +4˚C for 10 minutes (Eppendorf 5810R) to pellet the cells. The cell-pellet was then re-suspended in reduced serum media OptiMEM and counted using a hemocytometer. Finally, a cell solution at the required concentration of 750,000 cells/mL was created and loaded into the cell reservoir, which consisted of Tygon tubing (0.02 inches inner diameter, 0.06 inches outer diameter, 420 cm) wound around an empty 50-ml centrifuge tube. A 1-mL syringe (inner diameter: 4.606 mm) filled with PBS, was used to pump the cell solution from the reservoir into the device, while another 1-mL syringe was filled with required GDV particle solution and pumped into the device at desired flow rate, using syringe pumps (Harvard Apparatus, Holliston, MA).

Device setup:

Individual syringe pumps were used to operate each syringe to administer cells and GDV particles separately into the device at a pre-determined flow rates. Both the syringes (cells and GDV particles) were mounted on to the syringe pump and locked in place. The tubing from the cell reservoir was then connected to the cell-inlet on the device. Similarly the tubing from GDV particle syringe was connected to the GDV particle-inlet on the device. Finally, one end of an outlet-tubing was attached to the outlet of the device, whereas the other end was placed in a vial containing PBS (collection vial). Flow and mixing profiles inside the microfluidic device were characterized by using fluorescein sodium salt

solution (460 nm; Sigma-Aldrich Co. LLC., St. Louis, MO) instead of the cell suspension and water (the GDV solution), for various flow rates. Fluorescent images were analyzed using ImageJ software (National Institutes of Health).

For real-time flow cytometry (FACSVerse; BD Biosciences, San Jose, CA), the collection vial was directly attached to the flow cytometer via an adapter. Schematic of the setup is outline in Figure 3.2. Similarly, for other assays that required these device-treated cells to be plated, the vial with cells was centrifuged at 1000 rpm (201 X g) at +4˚C for 10 minutes (Eppendorf 5810R) to pellet cells. After removal of the supernatant, the cell pellet was re-suspended in the desired media (OptiMEM or DMEM) and subsequently added to wells in a cell culture plate. Various flow rates were studied using the microfluidic setup. Specifically, the flow rate of 10 μL/min for cell suspension and 40 μL/min for GDV particles was used for most GFP assays (at this flow rate, contact time between particles and cells is <1 minute).

Cell surface attachment – Cy5 assay

The cell surface attachment assay consisted of measuring percent positive cells for Cy5 using flow cytometry. The GDV particles were formulated using fluorescently labeled Cy5-pDNA. Data were acquired on flow cytometer for 2 to 5 minutes acquisition time. Cells positive for propidium iodide (PI; Life Technologies, Thermo Fisher Scientific Inc., Carlsbad, CA) were considered dead and gated out from analysis by using Flow Jo

software.

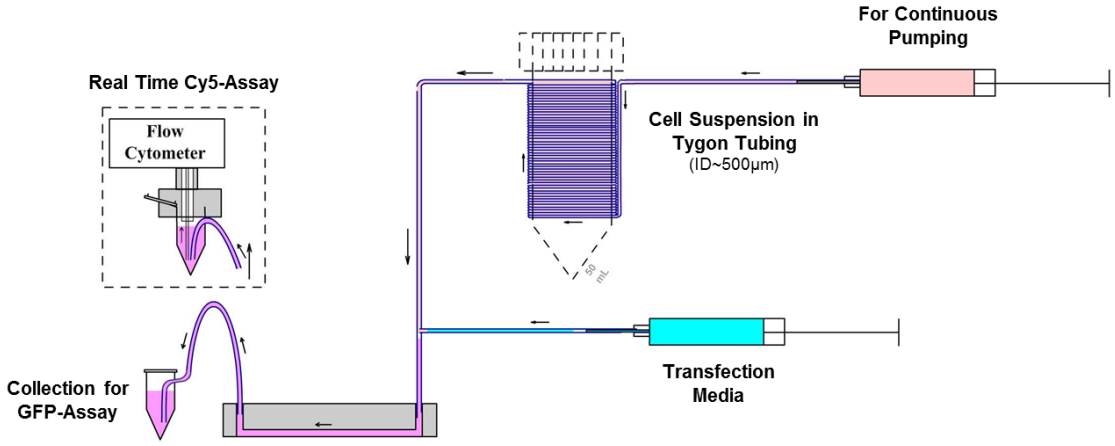

Figure 3.2 Schematic of the experimental setup. Transfection media was filled in a syringe and the cell suspension was filled in Tygon® tubing, which is pumped by another syringe into the device. The outlet of the device is connected to a flow cytometer for real time-Cy5 or collected in vial for GFP assay.

Method-1: Bulk plated:

A fixed number of cells were plated 24 hours prior to transfection: 50,000 cells/well in 12-well and 24-well plates for HDFn and HeLa cells respectively, and 120,000 cells/well in a 12-well plate for iPSC cells (<50% confluency at time of transfection). At the time of transfection, 264 μL of GDV particles solution (2.64 μg of pDNA) diluted with 528 μL of culture media, were added to wells to be transfected with GDV particles. Similarly, 264 μL of pDNA (2.64 μg of pDNA) diluted with 528 μL of culture media was added to control "pDNA only" wells and 264 μL of water diluted with 528 μL of culture media was added to control "Cell only" wells. The cells were then allowed to transfect for a pre-determined time of 15 minutes or 60 minutes at 37˚C and 5% CO_2. After the transfection time, cells

were trypsinized, washed with PBS and analyzed using flow cytometer for Cy5 positive cells.

Method-2: Bulk suspension:

Cells were added at a fixed concentration per tube, similar to that of the plated condition, to 5-ml-round-bottom Falcon-tubes. Next, 528 μL of culture media was added to each tube followed by 264 μL of GDV particles. Additionally, 264 μL of pDNA was added to "pDNA only" and 264 μL of water/culture media was added to "Cell only" samples, as a control. The cells were then allowed to transfect for a pre-determined time of 15 or 60 minute at 37˚C and 5% CO_2. Next, the cells were centrifuged, washed with PBS and analyzed on a flow cytometer for Cy5 positive cells.

Method-3: Device Suspension:

Cells treated on the device were collected in 500 μL PBS in a vial that was directly attached to the sample injection tube (SIT) on the flow cytometer. The acquisition rate on flow cytometer was higher than the outlet flow rate from the device, to enable real-time analysis of Cy5 positive cells.

Gene expression – GFP assay

The GFP gene expression assay was performed to quantify the transfected cells and measure the gene expression in the transfected cells. The GDV particles were formulated

using pZs-Green pDNA. Data was acquired on flow cytometer for 2 to 5 minute acquisition time. Propidium iodide stain was used to gate out dead cells from analysis.

Method-1: Bulk plated:

The cells were plated and transfected as described for the plated Cy5 assay. At the end of the transfection time, the cell monolayer was washed with PBS, followed by addition of cell culture media to the wells. The cells were then allowed to further incubate for specified durations (48 hours for iPSC and 72 hours for HDFn and HeLa cells). The media was periodically replaced (i.e., 24 hours) with fresh media specific cell type during incubation. Finally, the cells were washed, trypsinized and analyzed via flow cytometer for GFP positive cells and GFP intensity.

Method-2: Bulk suspension:

The cells were added to Falcon tubes and transfected as described for the suspension Cy5 assay. Similar to the plated assay, the cells were plated and incubated for a fixed duration (48 hours for iPSC and 72 hours for HDFn and HeLa cells). After incubation, cells were analyzed via flow cytometer for GFP positive cells and GFP intensity.

Method-3: Device Suspension:

Cells treated on the microfluidic device were collected in 1 mL PBS in 5 mL round-bottom Falcon tubes with a total of 50,000 cells/tube. The cells were then centrifuged at

1000 rpm (201Xg) at +4˚C for 10 minutes. After centrifugation, the supernatant was removed to eliminate the excess unattached vehicles from the media/cell suspension. The cell pellet was then re-suspended in 528 μL of OptiMEM and transferred to wells (24-well plate for HeLa cells and 12-well plate for HDFn and PFB). Subsequently, cell culture media was added to each well and incubated for specified duration (48 hours for iPSCs and 72 hours for HDFn and HeLa cells). Finally, cells were analyzed via flow cytometer for GFP positive cells and GFP intensity.

Cell synchronization experiments

To synchronize cells at the transition of G1/S phase in the cell cycle, a double thymidine block method was used. Briefly, cells were treated with 2 mM thymidine (Sigma-Aldrich Co. LLC., St. Louis, MO) in 10% FBS DMEM for fixed durations over two-day time prior to transfection. For the bulk-plated experiments, the cells were plated at a concentration of 30,000 cells/well in 12-well plate at 24 hours prior to the cell synchronization procedure. For the bulk suspension experiments, the cells were synchronized in a 75-cm^2-flask with less than 50% confluency. The cells were first blocked at the transition of G1/S phase by treating the cells with 2mM thymidine containing media for 18 hours. Thymidine solution was then removed from cells to release them from the blocked phase in the cell cycle, by washing with PBS, and fresh media was added to wells/flask. Cells were further cultured for 9 hours in the fresh media, followed by a second block in cell cycle at G1/S phase for 15 hours by again adding a fresh thymidine containing media to cells. Prior to transfection, synchronized cells were released from the blocked

condition by washing cells with PBS to remove any thymidine from well/flask. These synchronized cells were then transfected with GDV solution containing 0.66 μg of pDNA, according to the procedure described earlier in the GFP assay section. For the bulk suspension experiments with HDFn, the GFP assay was performed 96-hour after transfection. The efficiency of cell synchronization was confirmed by fluorescent Vybrant Dye Cycle Ruby nuclear stain (Life Technologies, Thermo Fisher Scientific Inc., Carlsbad, CA) using the manufacturer's protocol.

Statistical analysis

Data in bar graphs are presented as mean ± standard deviations. Statistical analysis was performed using JMP software from SAS Institute (Raleigh, NC) and means were compared using either a Student's t-test or Tukey's test method, with $p<0.05$ being considered as statistically significant.

3.3 Results and Discussion

GDV binding during bulk transfection of adherent cells

To test our hypothesis that the attachment of GDVs to cells is faster and more efficient in suspension than with a cell monolayer, we examined the delivery of GDV particles to the surface of human iPSCs. GDV particles were formed by the complexation

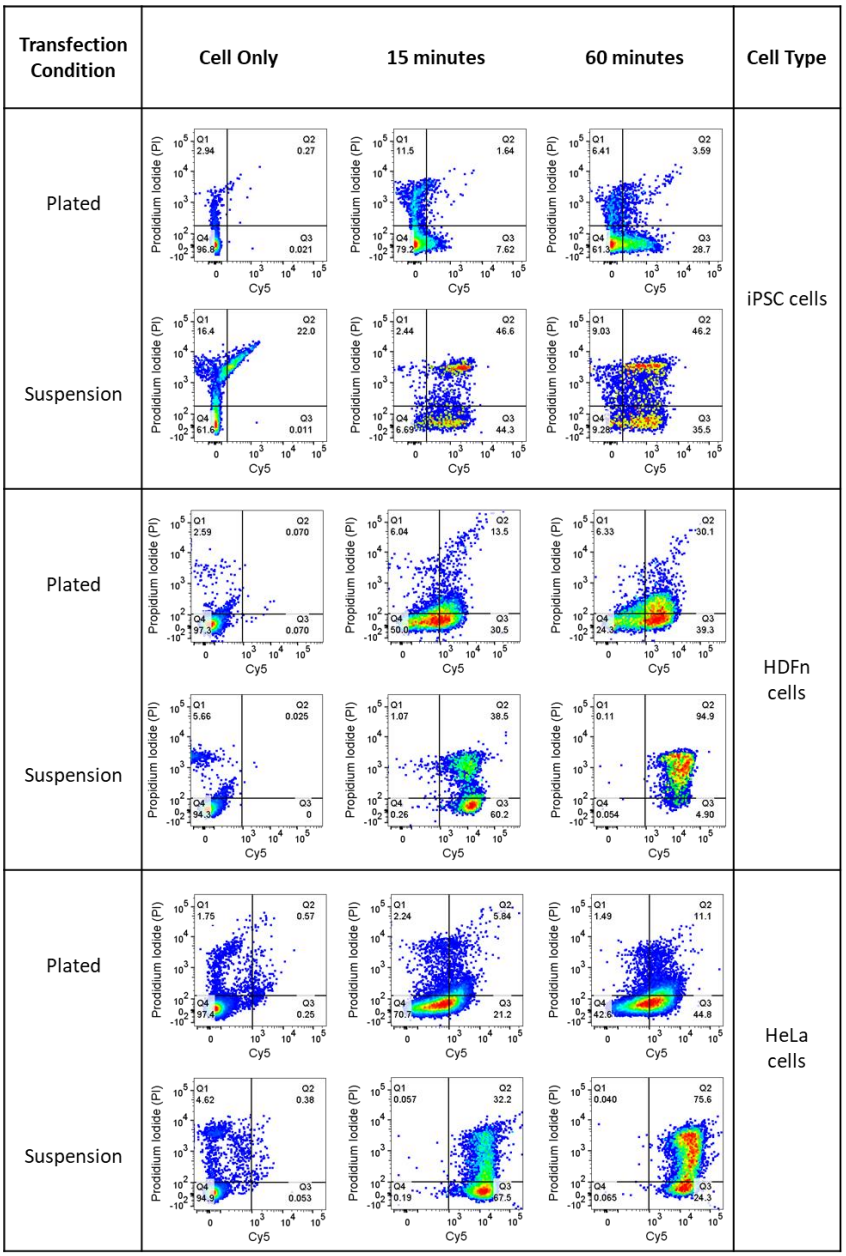

Figure 3.3 Flow cytometry analysis for the transfection of adherent cells (iPSC, HDFn and HeLa cells) with FugeneHD in bulk for Cy5 assay. Data are plotted as PI (y-axis) versus Cy5 (x-axis). Quadrant 1 (Q1) depicts cells that are only PI positive, Q2 denotes cells that are PI and Cy5 positive, and Q3 denotes transfected cells that are only Cy5 positive. All experiments were performed in triplicate and analyzed data are plotted in Figure 3.4.

of Cy5-labeled pCMV-lacZ plasmid with FugeneHD, a commercial non-liposomal

transfection reagent. iPSCs were suspended in mTeSR™1 media after gently scraping them from the well surface and exposed to the GDV solution for 15 minutes or 60 minutes, followed by a quick washing and centrifugation step to remove excess unbound delivery vehicles. Flow cytometry was then used to quantitate the percentage of live cells exhibiting

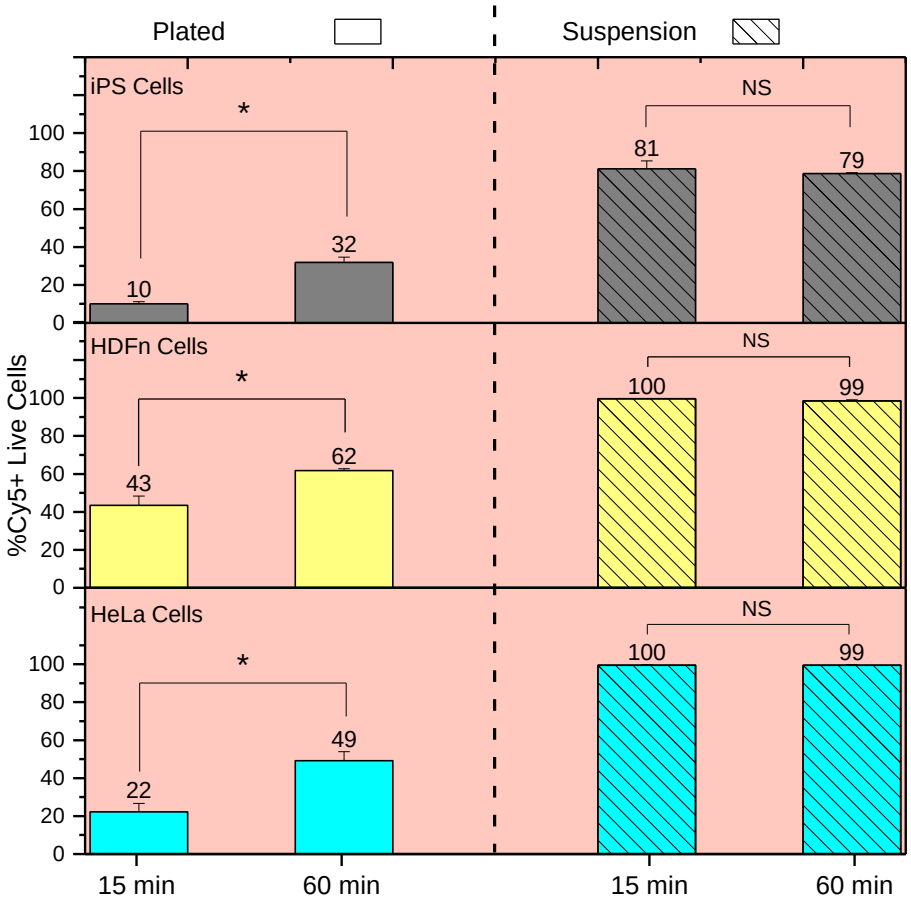

Figure 3.4 Comparison of delivery/gene expression (green region) of GDV particles to iPSc, HDFn, and HeLa cells in plated cells and in suspension. GDV particles were complexes of FugeneHD with pZs-Green plasmids (delivery). Data are reported as the percentage of live cells positive for GFP (n = 3). Representative raw flow cytometry data with gating are provided in Figures 3.3. [Note: "*" indicates samples are significantly different ($P<0.05$), "NS" indicates no significant differences between samples, all negative controls (cell only and pDNA only) < 0.5% and no significant differences between control samples for each cell types.]

a Cy5 signal (denotes GDV-cell attachment or internalization). Similar experiments were repeated with commercially available human dermal fibroblasts (HDFn) derived from neonatal foreskin, and human cervical adenocarcinoma (HeLa) cells that are a commonly used model for gene delivery studies. Figure 3.3 are the representative raw flow cytometry data with gating for different cell types and the analyzed data are plotted in Figure 3.4. As seen in Figure 3.4, the percent live cells associated with GDVs for all three cell types reached a maximum value within 15 minutes of exposure to the GDV transfection solution in suspension. In contrast, similar exposure of a cell monolayer (<50% confluent at the time of transfection) to transfection media had a significantly lower binding efficiency of GDVs to cells. The binding efficiency of GDVs to iPSCs is reduced as these cells tend to aggregate in cell clumps and shear stress during pipetting can cause differentiation of

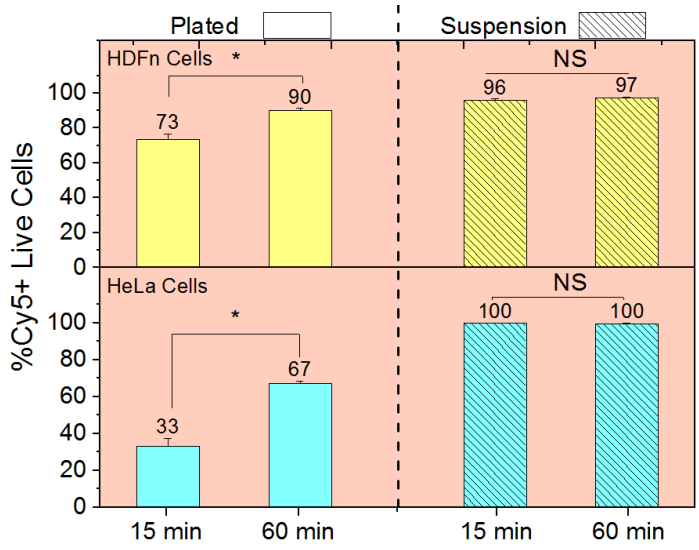

Figure 3.5 Successful binding (pink) of GDV particles (Glycofect complexed with Cy5 labeled pCM-lacZ) to HDFn and HeLa cells in plated cells and in suspension. Data are reported as the percentage of live cells positive for Cy5 (n = 3). [Note: "*" indicates samples are significantly different (P<0.05), "NS" indicates no significant differences between samples, all negative controls (cell only and pDNA only) <0.5%, and no significant differences between control samples for each cell types.]

iPSCs. Nevertheless, transfection of iPSCs in suspension provided much better access for GDV particles to adhere to iPSCs, even in clumps, when compared to the transfection of these cells in a 2D culture. To test that this procedural improvement was not specific to only FugeneHD, we repeated the experiments using HeLa cells and HDFn with another delivery vehicle, Glycofect, a polymeric delivery vehicle developed in our lab.[103] We observed similar results (Figure 3.5).

Gene delivery for the bulk transfection of FugeneHD GDVs

Fast and complete binding of GDV particles to the cell membrane is highly desirable but irrelevant if the bound particles do not eventually lead to internalization and the desired biological response, such as gene expression. To further examine transfection in terms of transgene expression after transfection of cells in suspension with the above conditions, we used pZs-Green plasmid (which contains a gene that encodes for green fluorescent protein, GFP) for the formulation of GDVs with FugeneHD. These experiments were similar to the binding assay with a minor modification. After washing the cells, they were plated and cultured for a fixed duration (48 hours for iPSCs and 72 hours for HDFn and HeLa cells). Thereafter they were analyzed for the number of live cells expressing GFP (Figures 3.6 and 3.7). Our results for iPSCs and HeLa cells demonstrate that attaching GDV particles in suspension results in at least a 2-fold increase in the overall efficiency of transfection (as evidenced by GFP expression) compared to conventional transfection in culture plates for 15 minutes of transfection time. For both cell types, the majority population of live cells was successfully transfected (77% for iPSCs and 91% for HeLa

cells) by GDV particles within 15 minutes of exposure to GDV solution in suspension. Moreover, transfection of HDFn in suspension (4.1% GFP-positive live cells) was

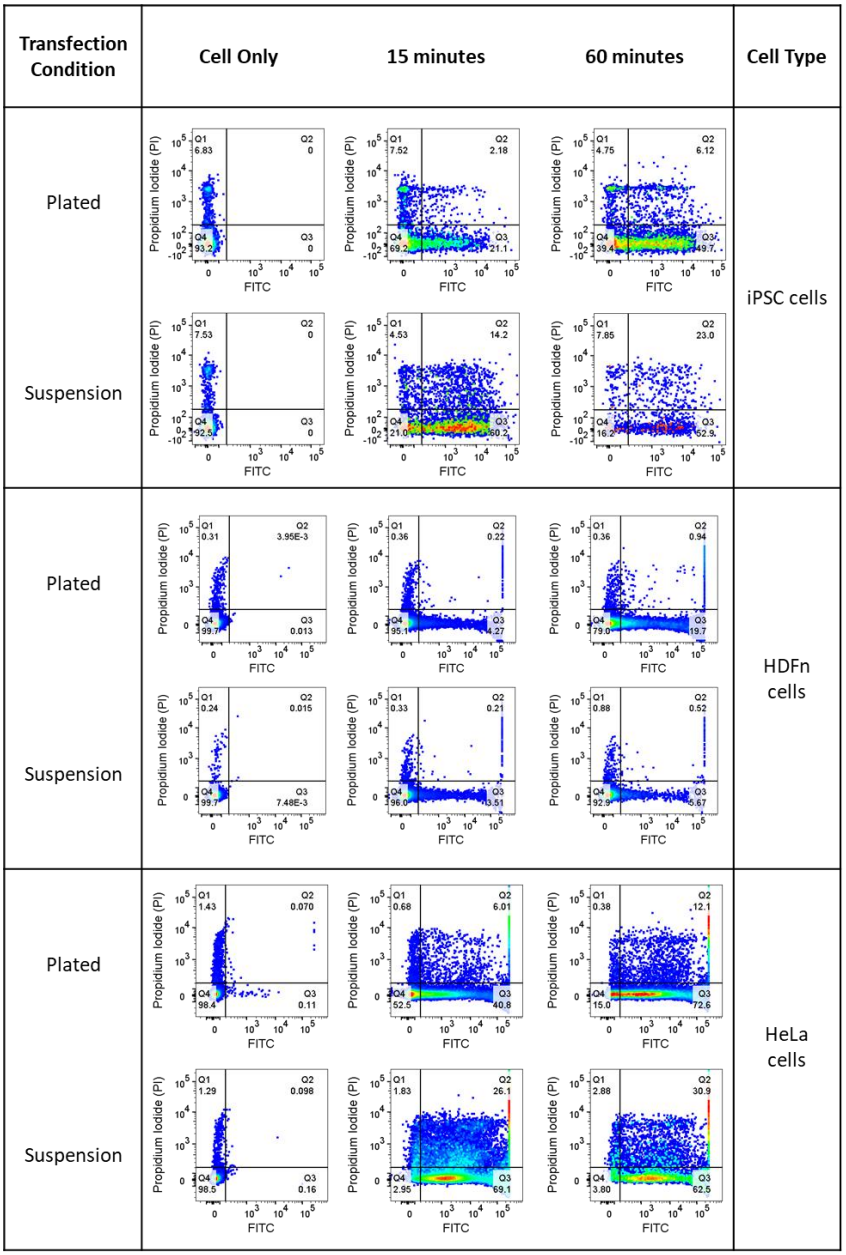

Figure 3.6 Flow cytometry analysis for the transfection of adherent cells (iPS, HDFn and HeLa cells) with FugeneHD in bulk for GFP assay. Data are plotted as PI (y-axis) versus FITC (x-axis). Quadrant 1 (Q1) depicts cells that are only PI positive, Q2 denotes cells that are PI and FITC positive, and Q3 denotes transfected cells that are only FITC positive. All experiments were performed in triplicate and analyzed data are plotted in Figure 3.7.

comparable to the plated condition (5% GFP-positive live cells) for a 15-minute transfection time.

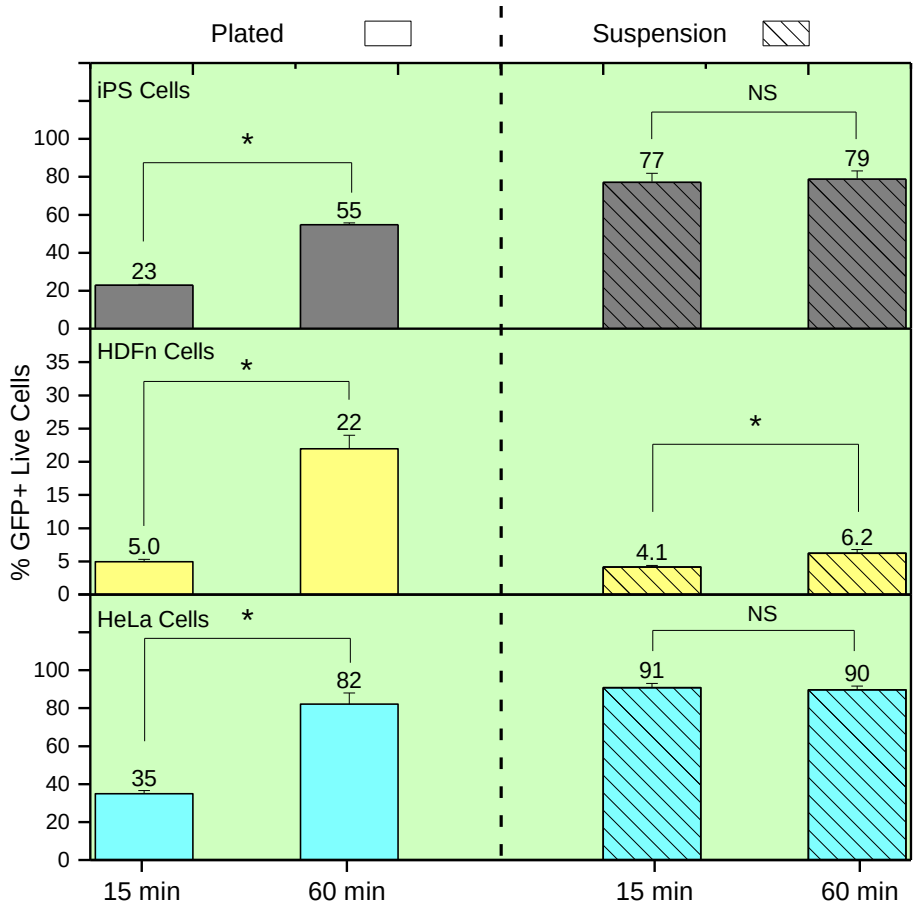

Figure 3.7 Comparison of delivery/gene expression (green region) of GDV particles to iPSc, HDFn, and HeLa cells in plated cells and in suspension. GDV particles were complexes of FugeneHD with pZs-Green plasmids (delivery). Data are reported as the percentage of live cells positive for GFP (n = 3). Representative raw flow cytometry data with gating are provided in Figures 3.6. [Note: "*" indicates samples are significantly different ($P<0.05$), "NS" indicates no significant differences between samples, all negative controls (cell only and pDNA only) < 0.5% and no significant differences between control samples for each cell types.]

Cell synchronization to improve gene expression for Glycofect GDVs

While we obtained high levels of GDV binding and transgene expression using the FugeneHD system, we found that Glycofect transfection reagent led to similar high binding efficiency of GDV particles in HDFn and HeLa cells (>95%) as compared to the negative controls (Figure 3.5). However, we did not observe any gene expression in either suspension or cell monolayer conditions. This negative result is contrary to the earlier reports of transfection in a cell monolayer for the 4-hour transfection time and may be explained by the use of a different reporter plasmid (luciferase versus GFP reporter system), or a lower dose of Glycofect particles in the experiments at 15 or 60 minute

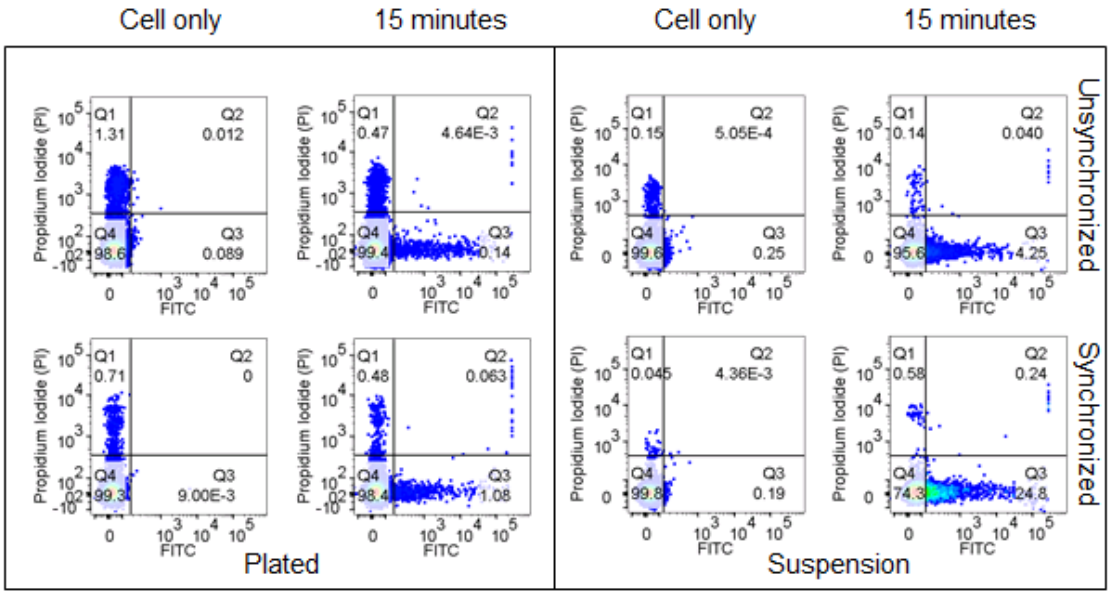

Figure 3.8 Flow cytometry analysis for the delivery (GFP assay) of GDV particles (Glycofect and pZs-Green) to HDFn cells synchronized at the transition of G1/S phase in 15 minute transfection time for plated and suspension condition. Data are plotted as PI (y-axis) versus FITC (x-axis). Quadrant 1 (Q1) depicts cells that are only PI positive, Q2 denotes cells that are PI and FITC positive, and Q3 denotes transfected cells that are only FITC positive. All experiments were performed in triplicate and analyzed data are plotted in Figure 3.9.

exposure times as compared to the 4-hour transfection time.[103–106] Earlier studies have reported that in the cell monolayer, Glycofect GDVs have slower kinetics of delivery[104] and that it is dependent on the cell cycle phase.[105] Therefore, we synchronized HDFn at the transition of G1 and S phase[107] and then transfected them with Glycofect GDVs for 15 minutes. Transfected cells were incubated for an additional 24 hours as compared to our previous experiments (i.e., 96-hour incubation) prior to assaying for GFP expression. The transfection data were again quantified using flowcytometry (Figure 3.8) and the analyzed

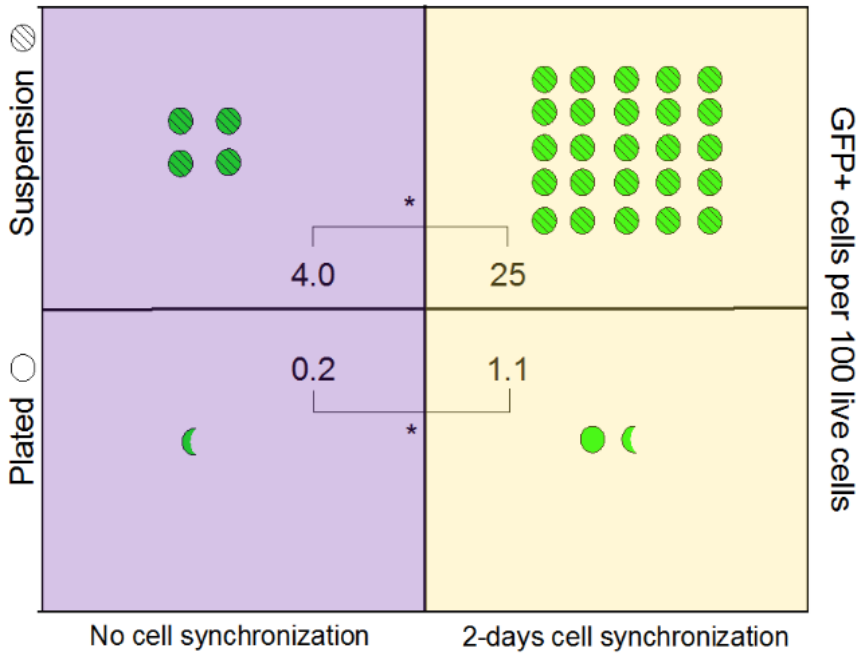

Figure 3.9 Successful suspension delivery of GDV particles (Glycofect and pZs-Green) to HDFn synchronized at the transition of G1/S phase. The cells were transfected for 15 minutes, followed by 96 hours of incubation. As a control, a cell monolayer was transfected for 15 minutes followed by 72 hours of incubation. Data are reported as the percentage of live cells positive for GFP (n = 3) and pictorially represented as green circles in the figure. Representative raw flow cytometry data with gating are provided in Figure 3.8. [Note: "*" indicates samples are significantly different ($P<0.05$), all negative controls (cell only and pDNA only) <0.5%, and no significant differences between control samples for each cell types.]

data were plotted in Figure 3.9. Under these modified transfection conditions, a 6-fold increase was found for suspended HDFn synchronized at G1/S phase (25% GFP positive live cells), as compared to unsynchronized suspended cells (4% GFP positive live cells) for 15-minute transfection time, as shown in Figure 3.9. This result further supports our finding that transfection of cells in suspension does not impact the intracellular transport of transfection agents and that a 15-minute exposure time is sufficient for the transfection of cells in suspension.

Microfluidic-based transfection of cells with GDVs

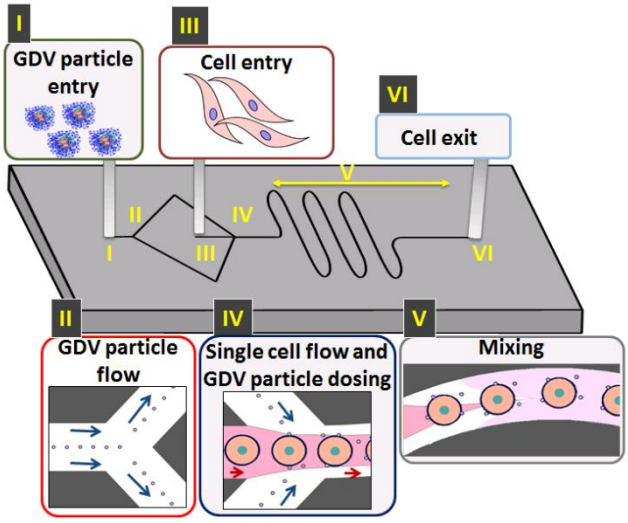

Figure 3.10 Schematic of the microfluidic suspension transfection device. The figure was designed by Nilesh Ingle.

To further investigate the suspension transfection method, we also explored the minimum contact time that can promote effective binding of GDV particles to cells. To provide increased control over the contact time, we fabricated a microfluidic device that

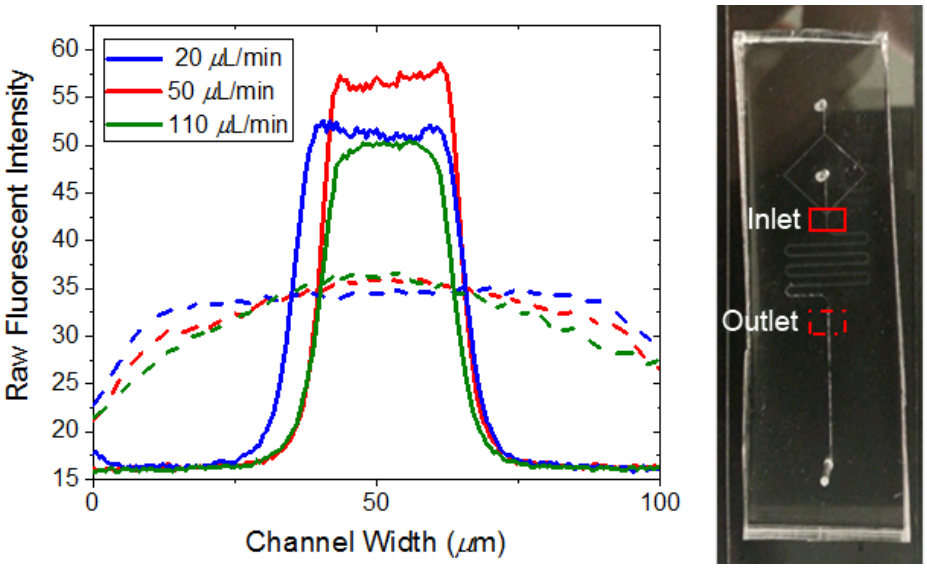

Figure 3.11 Mixing profile for total flow rates of 20 (blue), 50 (red), and 110 μL/min (green) in the microfluidic device. Water was used instead of the GDV solution and a solution of fluorescein was used instead of the cell solution. Ratio of flow rates for water and fluorescein solution was 4:1in all cases. Fluorescent images were taken at the inlet (solid line) and outlet (dash line) of the device (position marked in device image) and the fluorescent intensity was measured using ImageJ software.

delivers two streams of GDV particles that sheath a central stream containing an almost single-file stream of cells (Figure 3.10). A serpentine channel geometry was added that facilitated mixing of fluids (Figure 3.11) and promote reagent/cell interactions in suspension.[108] The device provides a contact time between the streams of less than one minute. Even with such a short contact time, we observed significant binding (>90%) of GDV particles to both HDFn and HeLa cells on the device (Figures 3.12). This result is robust to changes in the flow rates used on the device (Figure 3.13). Moreover, such high binding efficiency resulted in a significant percentage of GFP positive live cells (37% for HeLa cells and 4.6% for HDFn) compared to the negative controls (cell only), even for human adult primary fibroblasts (2.6%), as shown in Figure 3.14 and 3.15. The flow rates

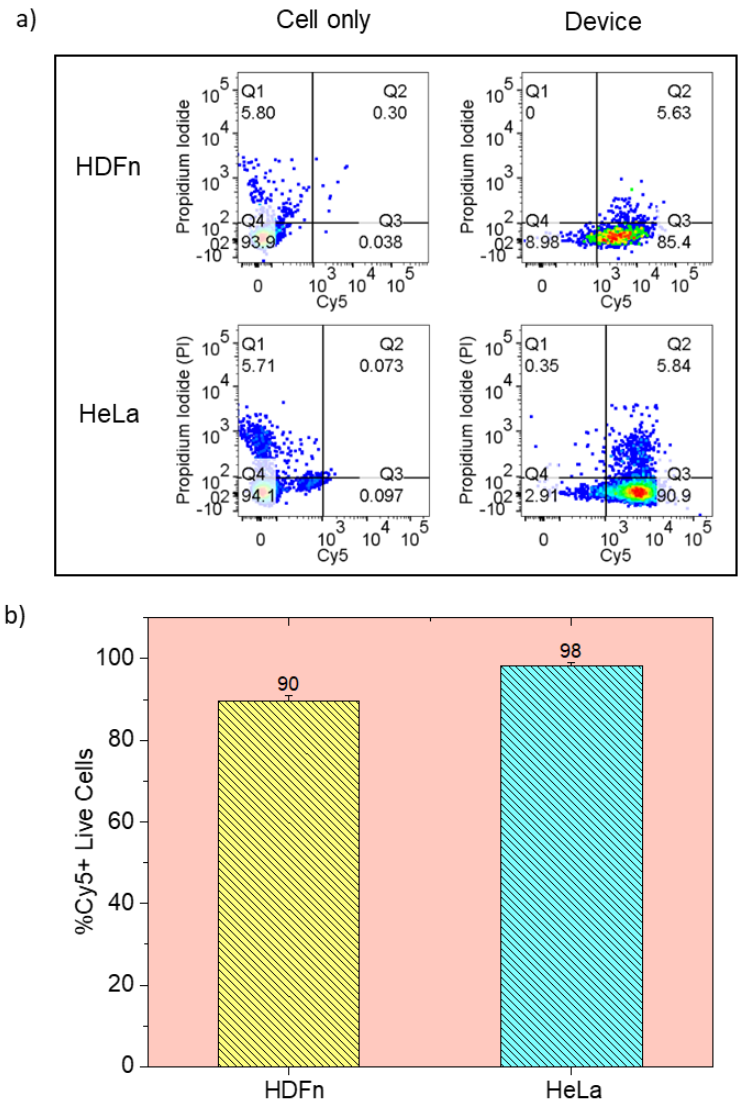

Figure 3.12 Successful microfluidic binding (pink) of FugeneHD GDVs to HDFn and HeLa cells (pCMV-lacZ plasmid). Flow rates were 10 μL/min (cells) and 40 μL/min (GDVs); the effective contact time between cells and GDVs was < 1 minute. Data are reported as the percentage of live cells positive for Cy5 (n = 3). a) Representative raw flow cytometry data with gating and b) analyzed result of the flow cytometry data. [Note: "*" indicates samples are significantly different ($P<0.05$) from "cell only" control, all negative controls (cell only and pDNA only) < 0.5%, and no significant differences between control samples for each cell types.]

(Figure 3.16a & c) had no significant effects on transfection, which is mainly attributed to

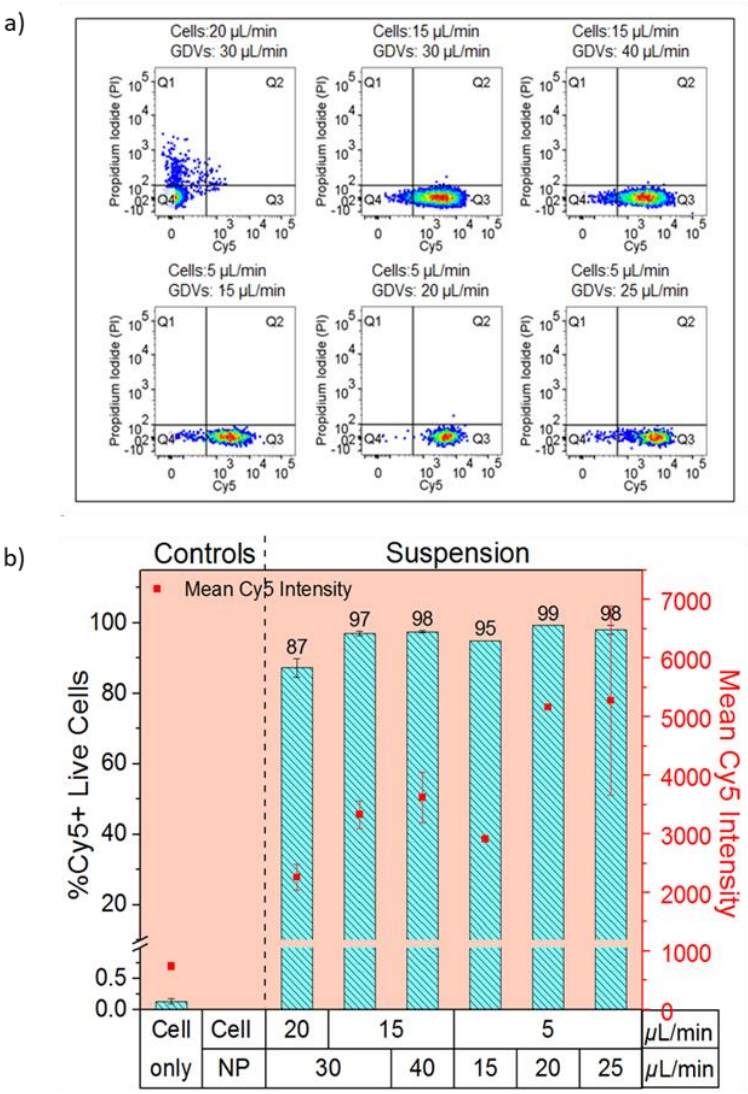

Figure 3.13 Effect of the relative flow rate of the inlet streams on GDV attachment to the cell surface for HeLa cells transfected with Glycofect GDV particles formulated with Cy5-labeled pCMV-lacZ plasmid. a) Representative raw flow cytometry data with gating for various flow rates. Data are plotted as PI (y-axis) versus Cy5 (x-axis). Quadrant 1 (Q1) depicts cells that are only PI positive, Q2 denotes cells that are PI and Cy5 positive, and Q3 denotes transfected cells that are only Cy5 positive. b) Analyzed data for the effect of flow rate on GDV attachment on cell surface. [Note: "*" indicates samples are significantly different ($P<0.05$) from "cell only" control, all negative controls (cell only and pDNA only) < 0.5% and no significant differences between control samples for each cell types.]

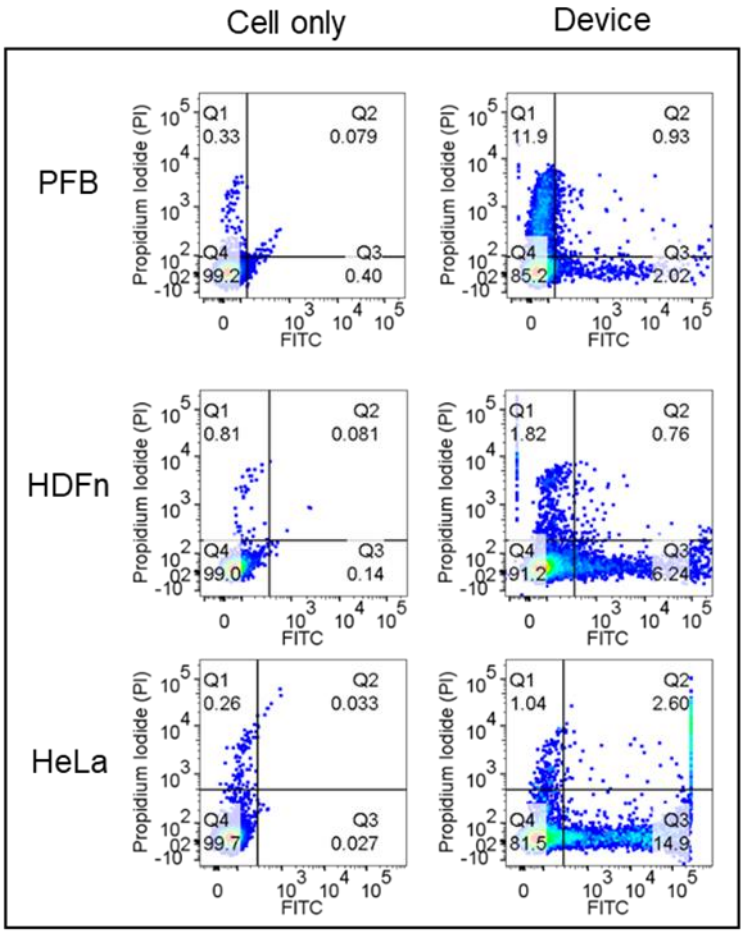

Figure 3.14 Flow cytometry analysis for the delivery (GFP assay) of FugeneHD GDVs to PFB, HDFn and HeLa cells using the microfluidic device. Data are plotted as PI (y-axis) versus FITC (x-axis). Quadrant 1 (Q1) depicts cells that are only PI positive, Q2 denotes cells that are PI and FITC positive, and Q3 denotes transfected cells that are only FITC positive. All experiments were performed in triplicate and analyzed data are plotted in Figure 3.15.

the similar mixing profile of the GDV and cell solutions inside the device at various flow rates (Figure 3.13). Similarly, the concentration of GDV particles in solution also had no significant effect on transfection (Figure 3.16b & d) because in a well-mixed environment, GDV particles quickly saturate the cell surfaces (<1 minute) and excess particles in solution will not have a significant effect on overall delivery at such a short time scale. Taken

together, the data show that there are essentially no transport limitations to GDV particle binding in suspension at the microscale and bond GDV particles are sufficient to achieve significant gene delivery.

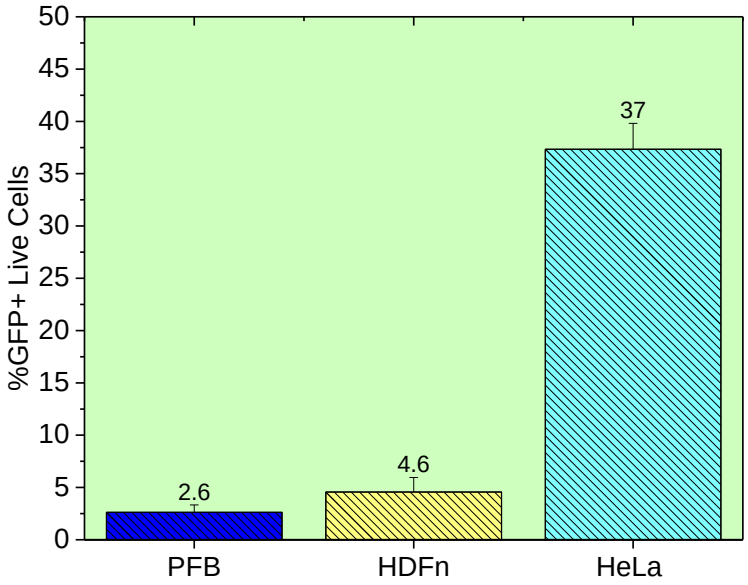

Figure 3.15 Successful gene delivery (green) to primary fibroblasts (PFB), HDFn, and HeLa cells (pZs-Green plasmid). Flow rates were 10 μL/min (cells) and 40 μL/min (GDVs); the effective contact time between cells and GDVs was < 1 minute. Data are reported as the percentage of live cells positive for GFP (n = 3). Representative raw flow cytometry data with gating are provided in Figures 3.14. [Note: "*" indicates samples are significantly different ($P<0.05$) from "cell only" control, all negative controls (cell only and pDNA only) < 0.5%, and no significant differences between control samples for each cell types.]

3.4 Conclusion

In summary, we have demonstrated that human stem cells, primary cells, and immortalized cells are effectively transfected in suspension. For laboratory applications, suspension transfection can reduce the protocol time by a full day, expediting the screening

of different gene delivery systems for a variety of biomedical uses. These improvements are potentially transformative for clinical applications, as our suspension transfection

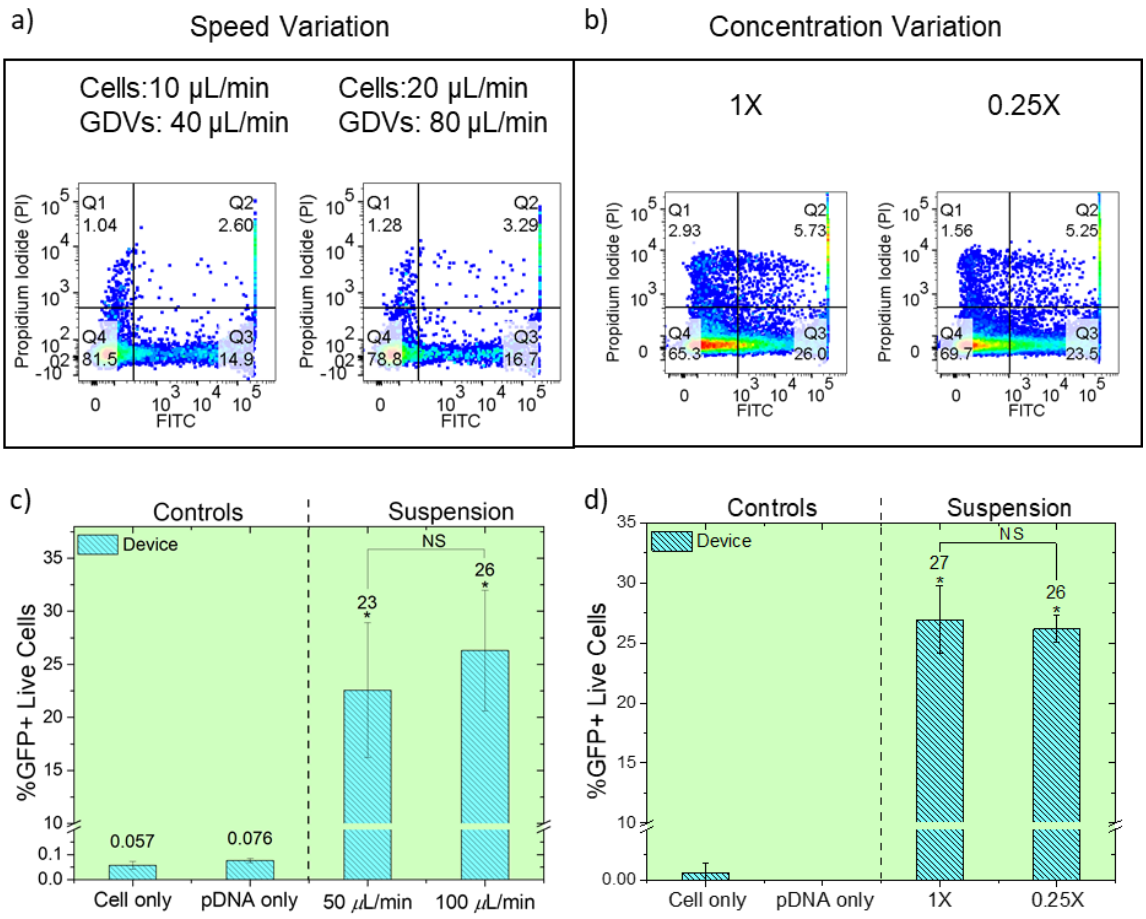

Figure 3.16 Optimization of delivery parameters for suspension transfection in a microfluidic device. Flow cytometry analysis for the transfection of HeLa with FugeneHD using a microfluidic device for a) different flow rates and b) different GDV concentration. Data are plotted as PI (y-axis) versus FITC (x-axis). All experiments were performed in triplicate. c) Effect of total flow rate on gene expression/delivery of GDV particles to HeLa cells in suspension with FugeneHD formulated with pZs-Green plasmid. Cell to GDV suspension flow rate ratio is 1:4. d) Effect of reagent concentration on gene expression for HeLa cells in suspension. GDV is FugeneHD complexed with pZs-Green plasmid with 1X concentration (2.64 μg pDNA/ 50,000 cells). Flow rates were 10 μL/min (cells) and 40 μL/min (GDVs). [Note: "*" indicates samples are significantly different ($P<0.05$) from "cell only" control, all negative controls (cell only and pDNA only) < 0.5% and no significant differences between control samples for each cell types.]

methods that also include a microfluidic system are fast, broadly applicable, scalable, amenable for high throughput transfections, and designed to ameliorate cell injury associated with gene transfer.

Chapter 4 – Micro-engineered cell culture systems to study the pathogen-host interaction

4.1 Introduction

The gastrointestinal tract is an extremely complex ecosystem with the largest microbial community in the human host, consisting of up to 10^{14} microorganisms over 500 species.[109,110] This diverse gut microbiome is often considered as a separate organ instead of just the collection of bacteria because of its significant role in human health and disease. Maintenance of the microbiome composition is crucial, and its disequilibria, commonly referred to as dysbiosis, leads to several gastrointestinal diseases. For example, the disruption in gut microbiota during antibiotic treatment or inflammation leads to increased susceptibility to intestinal infections.[111,112] The altered microbiota structure has been correlated with increased risk of obesity, colon cancer, etc.[113–115] Gut microbiota is also being considered as an intermediate target to alter the pharmacokinetics of an oral drug with the aim to improve the clinical response.[116–118] Moreover, recent evidence suggests that the gut microbiota influences the host response to immunotherapy.[119,120] All these potential benefits and disease management require an understanding of bacteria-host interaction, the mechanism of bacterial infection and host defense, the role of native microbiota in the pathogenic response and influence of local physiological conditions on bacterial infection. It is becoming increasingly clear that pathogens in the gut use signals derived from the host and commensal organisms to assess their environment and successfully deploy their virulence regime.[121,122] However, the complexity and diversity of

the human gut have made it challenging to elucidate the mechanisms of the response due to the interactions between the host, microbiota and intestinal pathogens. Establishing an *in vitro* gut tissue model will enable systematic research on commensal-pathogen interactions in the GI tract.

Enterohemorrhagic Escherichia coli (EHEC) is a deadly intestinal pathogen in humans that incorporates environmental, host and microbiota-derived signals in a complex signalling cascade to regulate its virulence genes. To colonize the intestine, EHEC employs a type III secretion system (T3SS) to inject effector proteins into host epithelial cells.[123] Bacterial effector proteins instigate host actin polymerization to form a "pedestal" structure around the bacteria. This leads to tighter adherence by the bacteria to host cells and eventual microvilli effacement and destruction of the intestinal epithelial layer. Physiological conditions, such as glucose and oxygen content, influence the bacterial adherence, expression of the T3SS and virulence of the pathogen.[124–126] In particular, the low oxygen concentration has been postulated to be necessary for adequate adherence of EHEC for viral infection but the mechanistic understanding in human physiological condition is important for managing EHEC infection.[125,126] There is a growing consensus on the significant influence of the gut microbiome on EHEC infection. It was recently observed in a cell culture infection model that the presence of the intestinal commensal organisms, *Bacteroides thetaiotaomicron* and *Enterococcus faecalis*, enhances expression of the EHEC T3SS and increase pedestal formation by EHEC.[127] However, the mechanism

governing this interaction remains unknown and the co-culture of bacteria with the epithelial cells is necessary for its study.

Applicability of *in vivo* or *ex vivo* tissue systems from humans and animals are limited by the fact that they are not always readily available owing to ethical considerations, short sample viability and tremendous variability among samples.[110] For example, genetically modified mouse models have a different lifespan, diet variation and microbiome population as compared to humans. Furthermore, small animal models of infection often fail to reproduce comparable symptoms as those seen in human clinical diseases. In particular, EHEC does not produce disease in mice similar to that seen in humans. Most often the natural mouse pathogen *Citrobacter rodentium* must be used for *in vivo* studies and results are extrapolated to the human pathogen, EHEC.[128] These limitations have advanced the development of many *in vitro* models that could provide the necessary physiological conditions required for the study and offer systematic control of experimental parameters.

An engineered *in vitro* model using intestinal adenocarcinoma cell lines is one such lucrative option. These biomimetic systems can provide an organizational complexity mimicking the *in vivo* conditions for understanding various forms of regulation, which control bacterial infection when they colonize the gut. The most common “gold standard” for the *in vitro* model is the static well plate based assays, including multi-well, Petri dish and Transwell, which provides a fast, easy-to-use and standardized model for the studies.[110] However, the static well models often fail to predict clinical results, as they do not fully

consider the role of local microenvironment on the biological response because these models do not incorporate important *in vivo* physiological conditions such as fluidic flow and anaerobic conditions. The static culture conditions allow bacterial overgrowth and low cell viability that limit the understanding of the host-microbe interactions.

Microfluidic systems are an increasingly popular tool to control the microenvironment for cell culture purposes.[129] The attractive features of microfluidics include a laminar flow profile, small sample volume, temporal and spatial control on a chemical gradient, in-situ characterization, and availability of biocompatible materials for the device fabrication. Microfluidic systems have been successfully adopted for many cell-based assays including chemotaxis, cell sorting and high-throughput screening. More recently, "organ-on-a-chip" microfluidic systems have been employed to support necessary requirements to recapitulate the minimal tissue- or organ- level functions and are being perceived as an alternative to animal studies for drug discovery and disease models.[130,131] Significant progress has already been made to mimic the functional response of human organs including the gut,[132,133] placenta,[134] eye,[135] breast,[136] heart,[137] kidney,[138,139] liver,[140] and lungs.[141] Few gut-on-a-chip models are available in the literature with important gut physiology including highly differentiated human villus epithelium with high barrier property, continuous fluid flow and selective oxygen control that have been used for viral and bacterial infection as well as drug discovery.[131] As these systems represent only the minimal function necessary for a particular study, having an adequate model is a prerequisite for the successful study. The ability to main the epithelial cell layer viability

and evaluate the infection response are the important necessities for the device design in this study.

Oxygen tension is an important parameter in an *in vivo* setting both for host cells as well as bacterial diversity, especially in the human gut.[142] For example, a typical epithelial cell only experiences 3-9 % oxygen concentration inside a human body as compared to 20 % oxygen in atmospheric air.[143] Similarly, the gut microbiome has a large population of strict anaerobes that flourish in the gut lumen without oxygen.[144] For the *in vitro* systems, the oxygen concentration could be controlled in three ways – by a chemical, biological, or physical method. The chemical approach is a common way for culturing the bacterial systems by using anaerobic packs that remove the oxygen from the vessel vicinity.[145] In the biological approach, facultative anaerobes can also create this environment by consuming oxygen through aerobic respiration, giving rise to an anaerobic environment which facilitates the growth of strictly anaerobic species.[127] This is also the natural method to achieve the anaerobic condition in a human gut, where facultative anaerobes are the initial colonizers of the infant's gut and strict anaerobes bloom later when the environment is fully reduced.[146] Finally, the physical method through passive diffusion involves the gaseous exchange of oxygen with inert carrier gas from the culture media.[147] This is the popular method in microfluidic systems, especially for the polymethyl siloxane (PDMS)-based devices, taking advantage of the high gas permeability ($D_{O_2} = 3 \times 10^{-9}\, m^2/s$) in PDMS.[148] The combination of high gas permeability and small diffusion length scale, the response time is fast in microsystems as in bulk.

In this work, we developed a microfluidic platform that facilitates the co-culture of bacteria and epithelial cells to study host-pathogen-commensal interactions during EHEC infection. This is of an urgent need for studies focusing on the role of commensal bacteria on the EHEC infection of epithelial cells.[149] Many of the species in the native microbiota are strict anaerobes while foreign pathogens invade the gut tissue lining in anaerobic conditions. The conducive anaerobic conditions for the diverse microbiota are maintained through a population of enteric facultative anaerobes. The common method to study bacterial infection of epithelial cells in static multi-well assays fails to provide the necessary environment that can maintain epithelial cells for an extended period while still promoting bacterial adherence and virulence. Additionally, the lack of an anaerobic environment in a traditional well-based assay makes the interactions between EHEC and anaerobic species of the microbiota challenging. This specific limitation stems from the competing requirements for the epithelial cells and microbiome, and requires engineering tools to achieve selective environment mimicking the apical and lumen side of the gut. The blood in the apical side of the gut supplies oxygen for the viability of epithelial cells and the facultative anaerobes in gut lumen support anaerobic conditions. We have designed a system where oxygen is pumped into the lower blood-like channel to support epithelial cells viability while EHEC consumes oxygen in the apical gut chamber to provide the anaerobic lumen-like environment.

4.2 Materials and methods

Device Fabrication

The microfluidic device (Figure 4.1) provides a biologically relevant environment for establishing intestinal cell/microbial floral community in the partitioned aerobic/anaerobic-partitioned milieu. The upper and lower chambers are two microchannels for fluid flow and were fabricated using a two-step lithography process – fabrication of SU8 mold on silicon wafer and casting of PDMS replica on the SU8 mold.[30]

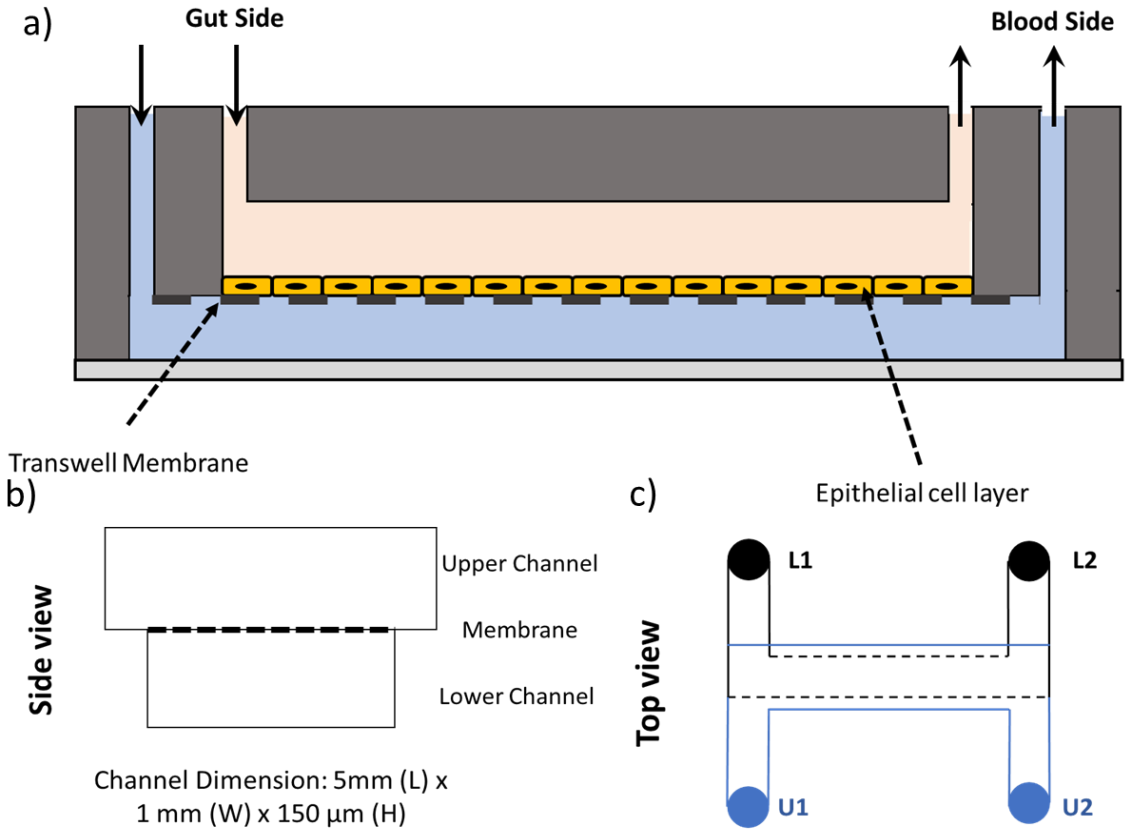

Figure 4.1 a) Schematic of device with the intended use for cell culture. b) & c) are the side and top views of the assembled device respectively, highlighting device components and channel dimensions.

The upper channel in 1.5 mm wide while the height of the lower channel was 1 mm. Both channels were 150 µm high and a length of 5 mm. To enable on-device imaging of a cell layer and bacterial infection, a very thin PDMS layer was cast on the SU-8 mold by using spin coater at 150 rpm for 60 s. The device was assembled by sandwiching a porous PET membrane (pore size 0.4 µm; VWR) between the two channels by using thin PDMS mortar for the leak-proof bonding of three components and curing it on a 80 ºC hot plate overnight.[150] The assembled device was bonded to the coverslip using plasma chamber, to provide mechanical rigidity as well as prevent evaporation through a lower channel inside the incubator. The schematic for the channel fabrication and the procedure to bond the PET membrane between the two channels are outlined in Figure 4.2.

Cell culture

Bulk cell culture

Caco2 (ATCC HTB-37) and HeLa (ATCC CCL-2) cells were cultured in DMEM

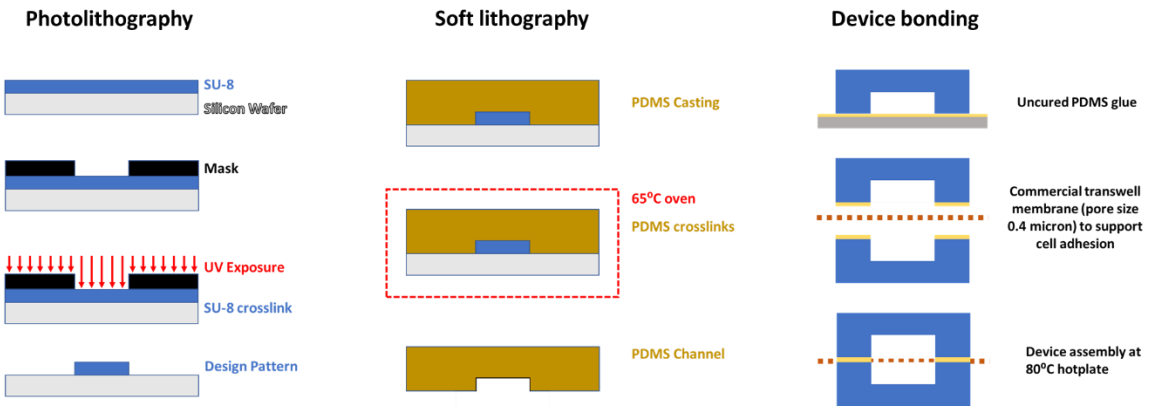

Figure 4.2 Workflow for the device fabrication involving photolithography and soft lithography process in silicon and PDMS respectively.

(4.5 g/L of glucose, Gibco) supplemented with 10 % FBS (Gibco). Cells were grown on T-75 flasks (Thermo Fisher) and passaged at 80 % confluence (typically every 5 days). Culture media was replaced every three days.

EHEC O157:H7 strain 86-24 transformed with pDP151, a constitutive-mCherry-expressing plasmid, were cultured in LB media (Sigma) with 100 μg/mL Ampicillin. The standing culture was incubated at 37 ˚C overnight in aerobic conditions. For the bacterial infection, the overnight bacterial culture is diluted to the desired CFU concentration in the DMEM with 1 g/L glucose and was added to the apical side of the cell layer for its direct contact to the cell surface.

Microfluidic cell culture

The fabricated device was sterilized before using it for the cell culture by washing both channels with 70 % ethanol, followed by overnight UV-irradiation inside the biosafety cabinet. On the day of the experiment, the top channel was coated with the appropriate extracellular matrix (ECM) components and incubated in a 37 ºC incubator for at least 4 h to assist the adhesion of epithelial cells to the membrane surface. For HT29 and Caco2 cells, rat-type collagen I (Corning) solution in PBS (1 mg/mL) was used,[151] while the fibronectin (Sigma-Aldrich) solution in PBS (10 μg/mL) was used for HeLa cells. The top channel was then washed with PBS solution to remove the excess ECM solution. Cells were trypsinized from a T-75 flask and added to the top channel (6-8 × 10^6 cell/mL) with a pipette. Seeded cells were kept in an incubator for 1 h under the no-flow condition to

allow cell adhesion to the membrane surface. After incubation, the top channel was washed to remove unattached clumps of cells, the bottom channel was filled with fresh media and the device was kept in an incubator for prolonged culture. Media was replaced each day and the cell layer was maintained for long durations (>10 days). A similar procedure was followed for the seeding of HeLa, Caco2 and HT29 cells.

Bacterial infection on the coverslip

The standard coverslip method was used as a positive control for the bacterial infection and establish the desired bacterial response that needs to be translated in the device before its use for the mechanistic study. The epithelial cells were seeded to a coverslip in a one well of a 12-well plate and the bacterial infection was performed after the two-day cell culture.[127] On the day of the experiment, the bacterial inoculum was prepared in DMEM solution (1 g/L glucose, sodium pyruvate) of desired concentration, added to the well and incubated at 37 °C with a 5 % CO_2 incubator for 3 h before changing the bacterial media with fresh media to maintain the viability of epithelial cells. The plate was further incubated for 3 h before fixing cells for imaging.

Bacterial infection on a microfluidic device

Figure 4.3 is the experimental setup for the co-culture of bacteria with epithelial cells. Briefly, the setup involved a continuous fluid flow in the bottom channel to provide continuous nutrition and oxygen to epithelial cells while facultative anaerobic bacteria like EHEC consumes the oxygen to maintain a microaerobic environment in the top channel

during its co-culture with epithelial cells. Various flow rates in the bottom channel were employed to understand the impact of oxygen supply on EHEC T3SS expression, which was quantified through EspA immunofluorescence (EspA is the major structural protein of the T3SS). The top channel was seeded with the desired bacterial concentration and co-cultured with epithelial cells at 37 °C in an incubator at the stationary condition for 6 h. The standing bacterial culture in a top channel provided the necessary contact time to attain microaerobic condition for bacterial adhesion to cell surface and virulence.

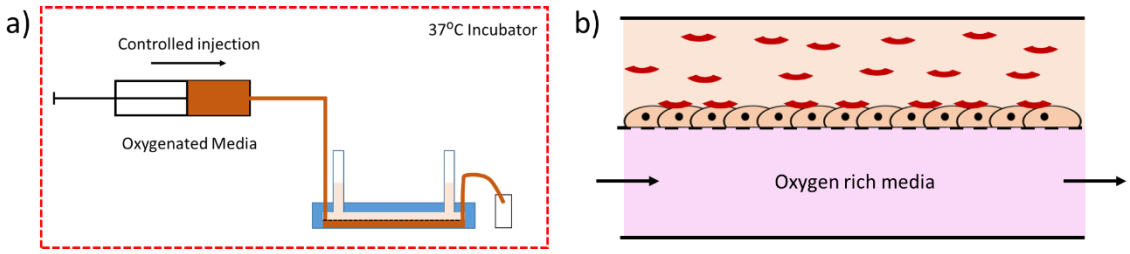

Figure 4.3 a) The experimental setup for the bacterial infection. The fluid flow in the bottom channel was controlled by syringe pump and the bacterial cells are cultured in the top channel under quiescent condition. b) Schematic of epithelial and bacterial cells locations inside the device during the bacterial infection.

Confocal and wide field microscopy

For immunofluorescence microscopic analysis, cells were grown in the coverslip/microfluidic device were fixed with 4 % (w/v) PFA, permeabilized with 0.2 % (v/v) Triton X-100. Hoechst Stain (Sigma) was used for nuclei counterstaining. Actin in permeabilized cells was stained with 1 µg/mL FITC-phalloidin to characterize cells layer on device and pedestal formation in response to infection. For the imaging of T3SS assembly, the EspA filament was stained with rabbit polyclonal EspA antisera at room

temperature followed by the staining with secondary antibody anti-rabbit IgG FITC (Sigma).[152] The samples were hard mounted using ProLong Diamond Antifade Mountant (Thermofisher) and liquid mounted using SlowFade Diamond Antifade Mountant (Thermofisher). The prepared sample was visualized using Zeiss LSM800 laser scanning confocal microscopy as well as Zeiss axiovision widefield fluorescence microscope. The device membranes were imaged on-device at 20X and the membranes were peeled off the device for 63X oil objective.

Oxygen measurement in bulk

The dissolved oxygen was measured for standing bacterial cell culture with a fiber optic sensor (FOXY, Ocean Optics) dipped in the culture solution. The sensor was calibrated with deoxygenated media by purging nitrogen and fresh media equilibrated at atmospheric conditions.

4.3 Result and discussion

Epithelial cell layer on the device

Epithelial tissues line the outer surfaces of organ and blood vessels as well as the inner surface of cavities in many internal organs such as the intestine. Many bacterial virulence factors cause damage to these epithelial tissues, thus breaking one of the defences against bacterial infection. Immortalized cell lines such as HeLa, HT29 and Caco2 cells are commonly used in epithelial cells and are thus used in this study. HeLa cells are a common epithelial cell type for the coverslip studies but do not truly represent the intestinal

lining, while the HT29 and Caco2 cells have been used in *in vitro* models to mimic functional characteristics of the human intestine.[153]

The cell culture of adherent cells in microfluidic devices requires a strong adhesion of cells to the channel surface and resistance to the shear stress on its surface during the fluid flow. The use of extracellular matrix components such as fibronectin, collagen and poly-L-lysin have been used to assist adhesion of mammalian cells in a microfluidic channel and choice of these components are cell type dependent. For the HeLa and gut epithelial cells (HT 29 and Caco2 cells), fibronectin and rat type collagen I were used respectively.

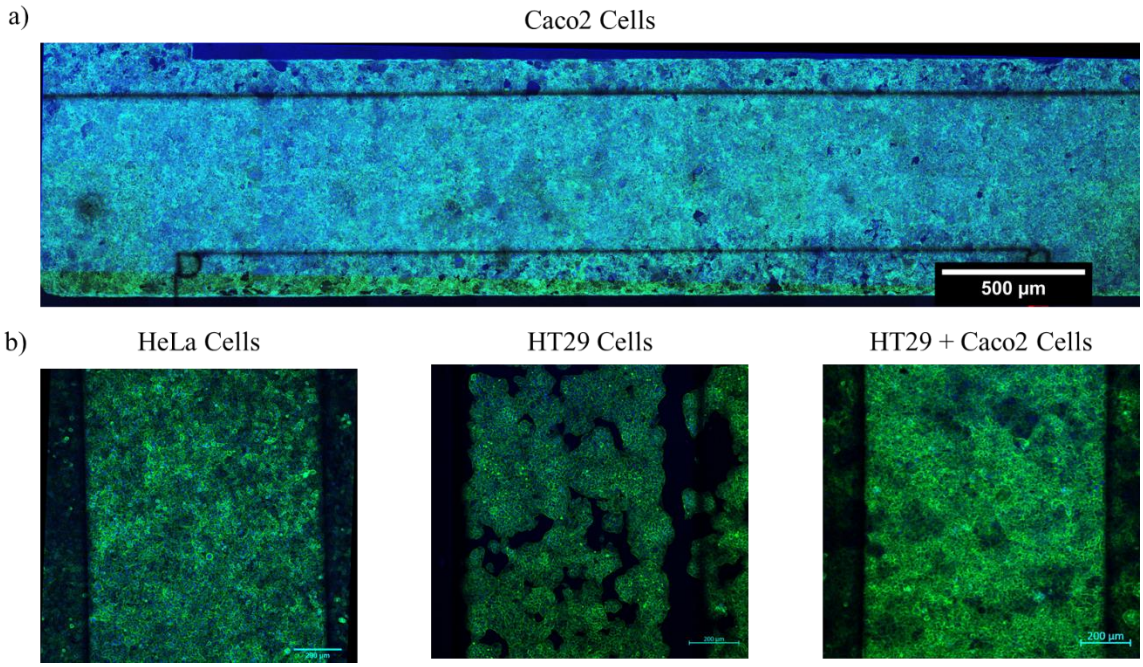

Figure 4.4 Confocal image of the epithelial cells in a microfluidic device. The cell nuclei were labelled with Hoechst stain (blue) and cell actin were stained with FITC-phalloidin (green). a) The confocal image of Caco2 cell along the microfluidic channel (scale bar 500 µm) and b) the representative confocal image on the channel for different cell epithelial cells: HeLa, HT29 and HT29+Caco2 cells (scale bar 200 µm).

The three epithelial cells were successfully seeded, and cell culture was maintained for at least 7 days. Figure 4.4 shows the confluent cells layer in the microchannel as highlighted by the staining of nuclei and actin using the Hoechst and phalloidin stains respectively. All three cell types form a living cell lining and its confluency was dependent on the cell type. For example, Caco2 and HeLa cells form a better confluent layer than HT29 cells. A mixture of Caco2 and HT29 was used to provide the necessary barrier property as well as the more functional characteristic of the human gut.

Bacterial virulence in epithelial cells on the coverslip

To observe the level of EHEC virulence factor expression, HeLa and HT29 cells were infected with EHEC and the T3SS needle, which is composed of EspA protein, was stained via immunofluorescence as shown in Figure 4.5. The bacterial infection was performed at the seeding concentration of 10^7 CFU/mL. EHEC is a facultative anaerobe capable of growing in anaerobic conditions. EHEC has a high rate of oxygen consumption[124] and the standing bacterial culture over the epithelial cell layer on the coverslip creates an anaerobic condition near the bacterial-epithelial cell interface as highlighted by the temporal graph of dissolved oxygen in the bacterial culture media. This setup supports the bacterial virulence response but significantly deteriorates the epithelial cell layer for prolonged culture. Therefore, the media must be replaced to prolong epithelial cell viability. This does not mimic the *in vivo* condition where the epithelial tissue line continuously receive oxygen from the apical blood side while the large population of facultative anaerobes maintains the anaerobic condition for a bacterial response.

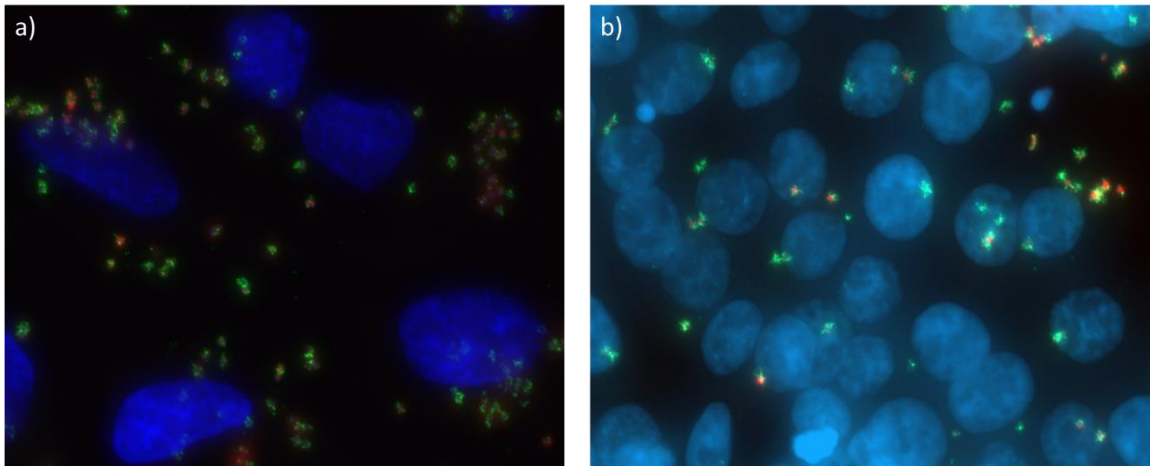

Figure 4.5 Representative images of EHEC infection for 6h in a) HeLa and b) HT29 cells in the coverslip setup. Images show m-cherry expressing EHEC (red), Hoechst stained nuclei (blue) and the FITC immune-stained EspA (green).

A mathematical model for oxygen consumption for the coverslip setup

EHEC uses several environmental cues such as the concentration of glucose, sodium pyruvate and oxygen to tightly control T3SS expression. Oxygen is an important variable as the *in vivo* conditions are drastically different from what can be simulated artificially. To better model a system that can closely recapitulate the *in vivo* condition in a microfluidic device, we need to understand the role of oxygen in modulating T3SS expression.

The dissolved oxygen is significantly consumed in the media by the bacteria as compared to the epithelial cells adhered to the coverslip, while the oxygen is only supplied through the atmosphere. The doubling time for EHEC is between 15-30 minutes and for the experimental duration of 6 h, the EHEC reaches to the 10^9 CFU/ml within 3 h in the standing culture. The oxygen consumption also increases with the bacterial growth during

the infection. The total oxygen consumption depends on the bacterial concentration (biomass) in the solution and the rate of oxygen uptake can be assumed to be independent of oxygen concentration (zeroth order kinetics) at a bacterial concentration. A quasi-steady state can be assumed at each bacterial concentration with the boundary conditions as a constant oxygen concentration at the top liquid surface and no oxygen flux at the coverslip surface. The oxygen concentration profile will be governed by the balance between the bulk consumption of oxygen and its diffusion from the top surface as related by the Damköhler numbers (*Da*). *Da* for this system is represented as:

$$Da = \frac{Kh^2}{DC_0} \tag{1}$$

where $K = K_0 \times b$ is the rate constant for the oxygen consumption that depends on the bacterial concentration (b) in the solution and has a constant specific oxygen

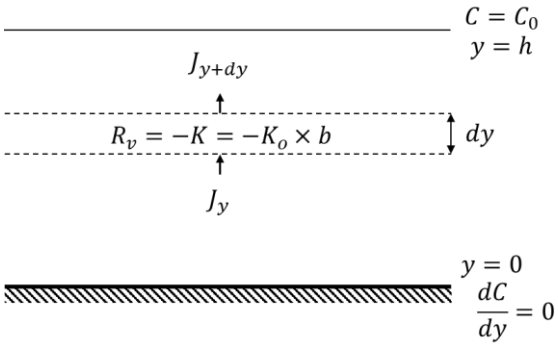

Figure 4.6 Steady state diffusion in a standing liquid. Concentration of oxygen molecule in liquid solution will be established by its diffusive influx through the surface as well as in bulk (J_y), while it is continuously consumed (R_v)in the bulk liquid. The schematic represents the mass balance and the boundary condition for small molecule in bulk. The mass balance at a steady state include the diffusion flux at element interface of area *A* and bulk consumption R_v.

consumption rate (K_0), h is the height of the liquid, D is the oxygen diffusivity in water and C_0 is the oxygen solubility in water at the experimental condition.

Figure 4.6 highlights the mass balance for oxygen in an element for the bulk and the boundary condition that must be satisfied by the solution. The material balance for oxygen at steady state and a particular biomass is represented by:

$$In - Out + Gen = 0 \tag{2}$$

$$AJ_y - AJ_{y+dy} + R_v A dy = 0 \tag{3}$$

$$\Longrightarrow \frac{dJ}{dy} = -R_v \tag{4}$$

Fick's first law relates the diffusion flux (J) to the concentration gradient and is represented as :

$$J = -D\frac{dC}{dy} \tag{5}$$

$$\Longrightarrow \frac{d^2C}{dy^2} = \frac{K}{D} \tag{6}$$

The final concentration profile for at a bacterial concentration can be expressed by the following non-dimensionless equation for $Da < 1$:

$$\theta = 1 - \frac{Da}{2}(1 - \eta^2) \tag{7}$$

where $\theta = C_a/C_0$ and $\eta = y/h$. The solution to this equation must satisfy the boundary conditions of $\theta = 1$ at $\eta = 1$ and $\frac{d\theta}{d\eta} = 0$ at $\eta = 0$.

For $Da > 1$, the oxygen concentration reaches to zero at a certain height in the liquid and the final equations representing all liquid height is given by:

$$\theta(\eta) = \begin{cases} 1 - \frac{Da}{2}(1 - \eta^2), & h \le \eta \le \eta_0 \\ 0, & \eta_0 < \eta \le 0 \end{cases}, \text{ where } \eta_0 = \sqrt{1 - \frac{2}{Da}} \tag{8}$$

Table 4.1 tabulates the rate of oxygen consumption and doubling time for EHEC in literature as well as calculated values for Da.[154,155] Based on the doubling time, EHEC will reach to 10^9 CFU/mL in ~2.5 h. The predicted high oxygen consumption with an increase in the biomass is consistent with the actual dissolved oxygen measurements in the standing bacterial culture using the DO probe as shown in Figure 4.7. These results suggest that the coverslip experiments were performed under oxygen tension near the vicinity of the epithelial cells surface. To maintain the epithelial cell layer viability, the oxygen-depleted

well media was replaced with fresh media after 3 h of infection. This is not the case *in vivo* as there is a continous oxygen supply to epithelia tissue lining from the blood side that supports tissue viability and provides a necessary barrier to the bacterial infection. A similar approach was adopted for the new microfluidic platform that used facultative bacteria as an oxygen scavenger and the blood-like bottom channel to control oxygen supply in the culture system.

Table 4.1 Parametric calculation for oxygen consumption in coverslip setup.

Max. oxygen consumption by *E. coli* (moles/CFU/h)		1.05×10^{-17}
Diffusivity of oxygen in water (cm^2/h)		0.117
Doubling time (min) $G \equiv \frac{t}{3.3 \log_{10}\frac{b}{B}}$		22.5
Bacterial concentration (CFU/mL)	$b = 10^7$	$B = 10^9$
K (mole/mL/h)	8.31×10^{-8}	8.31×10^{-6}
Da	0.54	54
η_0	NA	0.98

Effect of flow rate on EHEC T3SS in epithelial cells

EHEC infects both the human and bovine gut, where robust colonization is dependent on its T3SS expression.[126,127,156] While building the *in vitro* model, it is necessary to simulate both conditions — the coverslip and the *in vivo* like conditions, to make full use of the already known results based on existing models and then provide a more realistic prediction for various disease manifestations in the human body. In this

effort, we performed the bacterial infection on microfluidic devices with standing bacterial

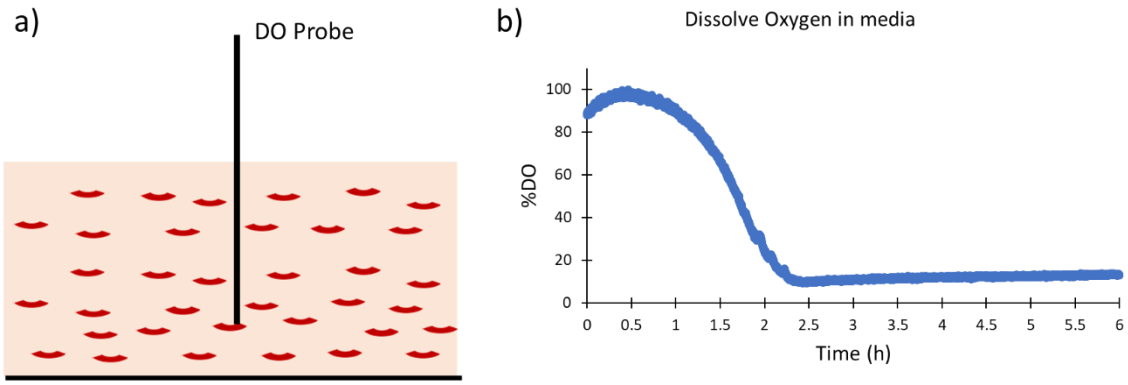

Figure 4.7 a) Schematic of coverslip setup used for bacterial infection. This setup was used to measure the oxygen concentration in media over time, which is similar to the coverslip condition. b) Temporal measurement of dissolved oxygen (%) in media using a DO probe for 6 h duration.

culture in the top channel that consumes oxygen in the top channel and limited the oxygen flux from the bottom channel by controlling the fluid flow in the bottom channel. To visualize levels of T3SS expression, immune-staining of EspA was performed to characterise the extent of infection in response to the oxygen tension.

The bacterial response was first evaluated at 50 µL/h flow rate in the bottom channel. Under such conditions, the T3SS was not observed in HT29 cells devices for 6 h incubation. Prolonged infection for 9 h showed few cells with T3SS expression, while very long infection duration of 24 h showed significant T3SS expression. Performing a long infection on the device also deteriorated the epithelial cell layer in the device. All epithelial cells were washed out of the channel during the staining process indicating high bacterial infection for the 24 h condition. The minimum flow rate of fresh media (based on Table 4.1) necessary to match the oxygen demand at inoculation density (10^7 CFU/mL) is ~0.3

µL/h and it increases to 30 µL/h for 10^9 CFU/mL. At high flow rate condition (50 µL/h), the oxygen supply to the device is higher than the oxygen consumption by the epithelial and bacterial cells. This suggests that the high oxygen concentration delays bacterial infection in epithelial cells, which is mainly attributed to the decrease in the bacterial adhesion to the epithelial cell surface.

If the adherence of epithelial cells and T3SS expression are oxygen dependent, controlling its flux by the fluid flow in the bottom channel should reproduce a similar phenotype as observed in coverslip experiments. To further verify the impact of oxygen on T3SS expression in EHEC infection of epithelial cells, we compared the response of on-device infection at two flow rates: 0.5 and 50 µL/h for 6 h infection. The low flow rate value was estimated based on the oxygen consumption rates used for the bulk model and a 100-fold increase flow rate represent the oxygen-rich condition, as shown in Figure 4.9 and 4.10. Under the limited oxygen supply, all types of epithelial cell devices expressed a significant increase in EspA expression within 6 h of infection at 0.5 µL/h as compared to the high flow rate condition of 50 µL/h.

The microfluidic model works on the idea that the bottom (apical side) channel would be the only source of oxygen available for consumption by the epithelial and bacterial cells. While the oxygen is necessary for the epithelial cells, limited oxygen (microaerobic) condition enhances bacterial adhesion factor for EHEC which in turn assist higher bacterial infection. We hypothesise that EHEC self-regulates the oxygen condition

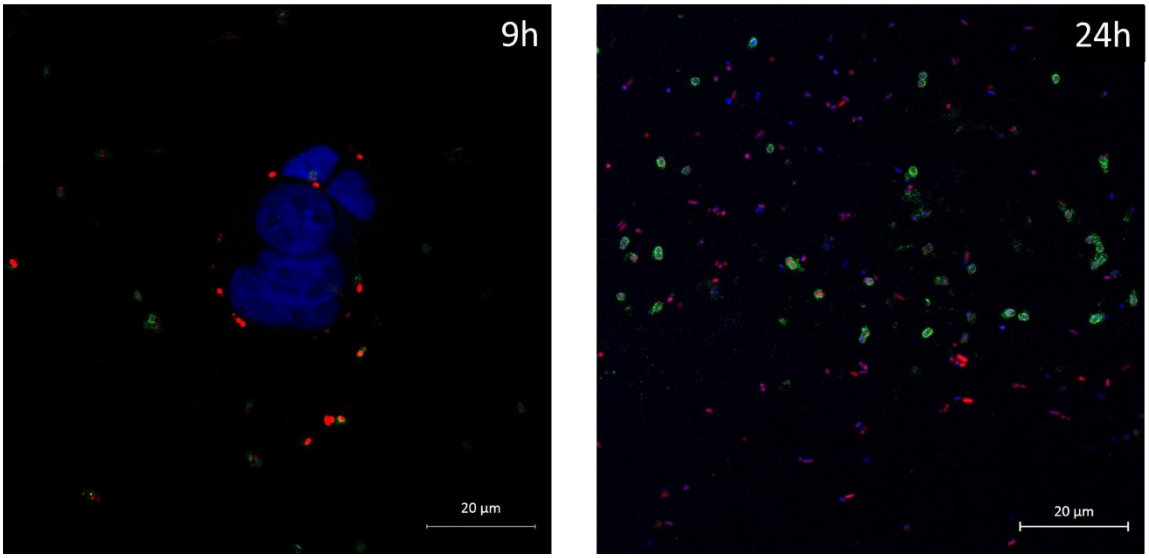

Figure 4.8 Representative image for the EspA expression due to EHEC infection in HT29 cells at 50 µL/h for the 9 h and 24 h infection. Images show m-cherry expressing EHEC (red), Hoechst stained nuclei (blue) and the FITC immune-stained EspA (green). Scale bar 20 µm.

analogous to the *in vivo* condition where the large pool of facultative anaerobes assists in achieving the anaerobic/microaerobic environment in the human gut.

4.4 Next generation microfluidic system

Our current model successfully demonstrates the impact of oxygen on the bacterial response for the facultative anaerobe (EHEC), but the system does not support the culture of only strict anaerobes which need low oxygen concentration to grow. Certain modifications are necessary to independently manipulate the oxygen concentration in the top channel. This will be useful in two ways – as a control device that supplies oxygen to the top channel to compensate for the oxygen usage by the bacterial cells and secondly, to

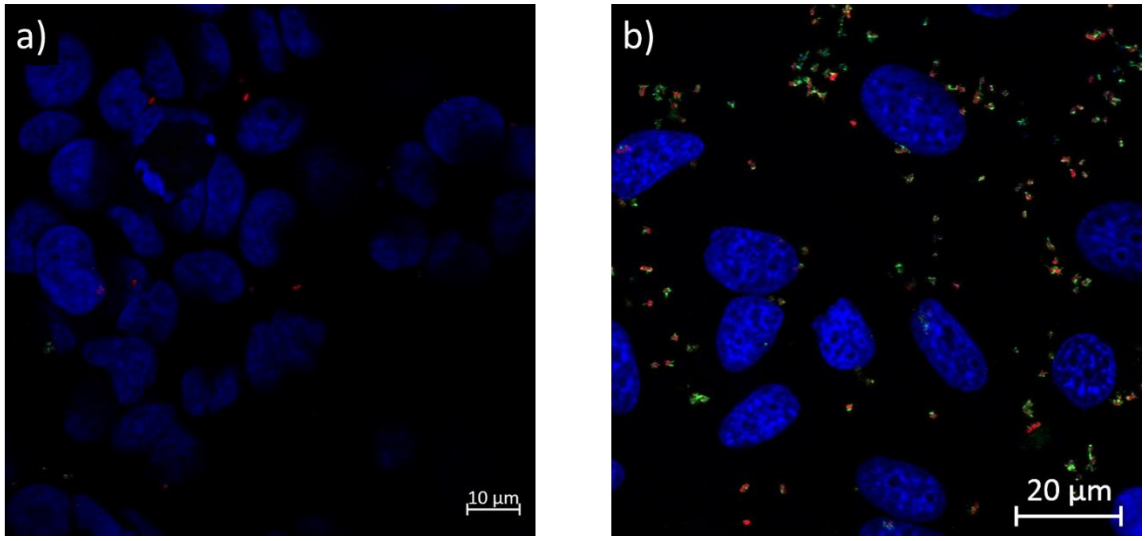

Figure 4.9 Representative image for the EspA expression due to EHEC infection for 6 h in HeLa cells at different flow rates: a) 50 µL/h and b) 0.5 µL/h. Images show m-cherry expressing EHEC (red), Hoechst stained nuclei (blue) and the FITC immune-stained EspA (green). Scale bar 20 µm.

remove oxygen from the top channel irrespective of the type of bacteria present in the channel. The first role will help validate the hypothesis that EHEC infection is oxygen dependent that was observed at low flow rate while the second usage of the new device will be to provide an anaerobic condition for strict anaerobes for more advanced parametric studies. Taking advantage of the high gas permeability in PDMS, an additional control channel will be added to the existing design for the operational flexibility.[157]

We can modify our system to remove oxygen from the top channel through its diffusion into the carrier gas by adding a third channel over the top channel separated by a thin PDMS layer to provide liquid barrier and gas permeation, as shown in Figure 4.11.

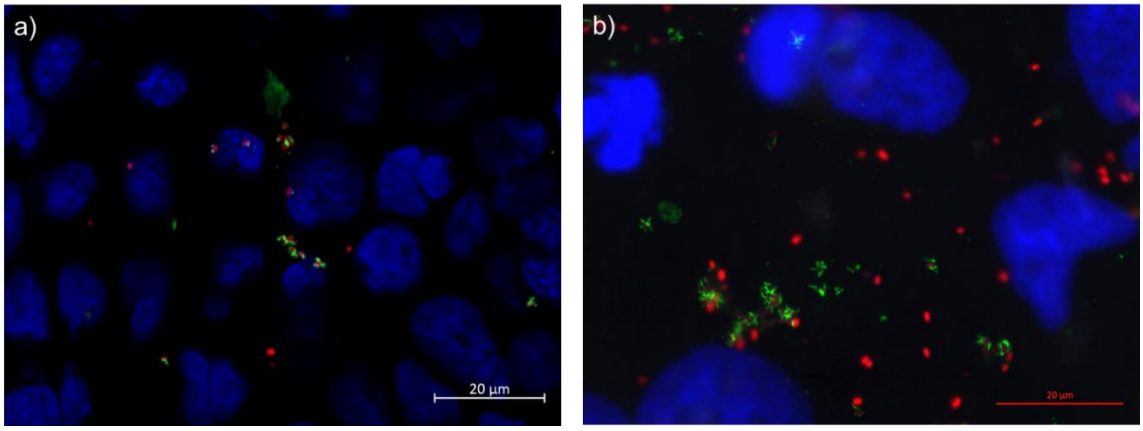

Figure 4.10 Representative image for the EspA expression due to EHEC infection for 6 h in a) Caco2 cells and b) HT29+Caco2 cells at 0.5 µL/h. Images show m-cherry expressing EHEC (red), Hoechst stained nuclei (blue) and the FITC immune-stained EspA (green). Scale bar is 20 µm.

The three-layered device can be fabricated using the soft lithography. The control gas channel would be cast on the SU-8 mold on the silicon wafer while the middle bacterial channel is spin coated on a SU-8 mold to control the thickness of the PDMS layer and control the rate of oxygen removal through carrier gas. The control channel fabricated using bulk casting and bonded to the spin-coated PDMS casting on the SU-8 top channel mold before peeling it off the mold. The assembled channel and the bottom channel will sandwich the trans-well membrane similar to that shown in Figure 4.2.

For the new setup to work as a negative control for the study, the control channel needs to have a continuous flow of oxygen-saturated PBS that will supply the oxygen to the bacterial channel and counter the oxygen usage by the bacterial uptake. If oxygen is indeed such an important factor for EHEC infection, this indirect supply of oxygen should

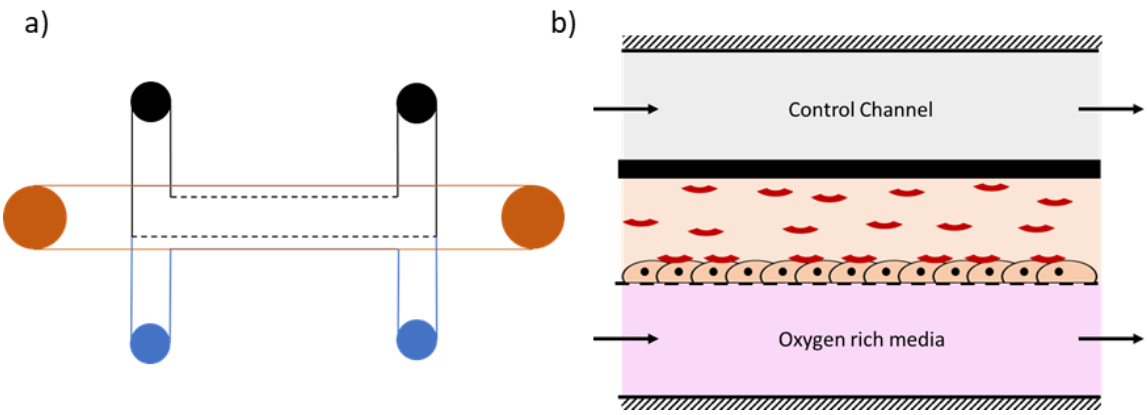

Figure 4.11 a) Schematic of modified device with the additional control channel. b) Schematic of epithelial and bacterial cells location inside the device along with the control channel during the bacterial infection. Flow of oxygen-rich media or nitrogen gas will be controlled in the top channel depending on the intended role of the new device as a control device or anaerobic micro-reactor respectively.

show low/no EspA expression similar to the high flow rate condition in the earlier device. The use of PBS instead of air will prevent the drying of the bacterial channel due to the evaporation of water through the control channel.

On the other hand, for the device to act as an anaerobic chamber for strict anaerobes, pressured nitrogen flow through the control channel to strip the oxygen from the bacterial media. The carrier gas in the control channel should be saturated with water to prevent water evaporation during the experiment. An important requirement for this system to work is the design of a pressure system to control the pressure and composition of the carrier gas in the channel. The anaerobic condition in the bacterial channel could be verified with the luminescence measurement of oxygen sensitive dye, Tris(4,7-diphenyl-1,10-phenanthroline)ruthenium(II) dichloride complex (1 mg/ml) in PBS.[158]

4.5 Conclusion

This is a first attempt to use microfluidic tools to study the mechanism of EHEC virulence especially in the more *in vivo* like setting. The first design successfully elucidated the role of oxygen for EHEC infection in epithelial cells and demonstrated the ability to use facultative anaerobes in a microfluidic device to modulate oxygen. This is an ongoing effort to better the *in vitro* model for a more realistic study to predict *in vivo* response. Furthermore, we propose an advanced model that will allow the culture of strict anaerobes as well as facultative anaerobes for the parametric study. For example, to investigate the contribution of native gut microbes towards the EHEC infection, it would require co-culturing commensal gut bacteria before introducing a pathogen into the system. Our interdisciplinary approach helped to develop a unique as a well as a simple solution for the mechanistic understanding of a human gut. Indeed, interest in microbiome studies extends far beyond EHEC, as it has been linked to obesity, colon cancer, infectious disease, brain development, Crohn's disease and many other illnesses. The current system can further be modified to handle engineering as well as biological problems related to the gut, such as prolonged co-culture as well as drug-resistance bacteria.

Chapter 5 – Conclusion and perspective

The three applications described in this dissertation demonstrate the benefits of microfluidic technology in overcoming some of the challenges in the field of biotechnology. Chapters 2, 3 and 4 describe the proof-of-concept results for the technology and further advancements can be made in the device design or its application in other fields, for each of the three technologies. This chapter discusses some plausible future improvements in the device design and operations that will help in the advancement of their applications in various fields.

5.1 Entropic trap purification of long DNA

This is still an ongoing work in our group with many potential avenues to explore its use for long DNA applications such as genome mapping. This includes the optimization for device design and operation, filtration of different biological molecules, and the characterization of filtration performance for real-life applications.

There are several aspects of optimization possible in our filtration system. In terms of device design, we have employed six slits each for the pre-filtration and main-filtration zone. These nanoslit counts were retained during the initial development process and can be optimized using the resistor model. Furthermore, the filtration system design in Chapter 2 is a unit operation and multiples of such operations can be arranged in series to achieve desired purity, as shown in Figure 5.1. For single stage filtration, we have demonstrated

that the selectivity and yield complement each other and must be optimized further for each application. Multiple stages can help achieve higher purity without compromising the DNA yield. Moreover, the height of the nanoslit dictates the filtration performance and the multi-stage filtration can have various nanoslit heights for sequential filtration of different sizes of DNA. Further optimization will involve tuning the operating parameters such as filtration voltage, filtration time, injection pressure, and injection time. For the advancement of the filtration system to commercial use, these design and operation parameters will have to be explored in detail for each application.

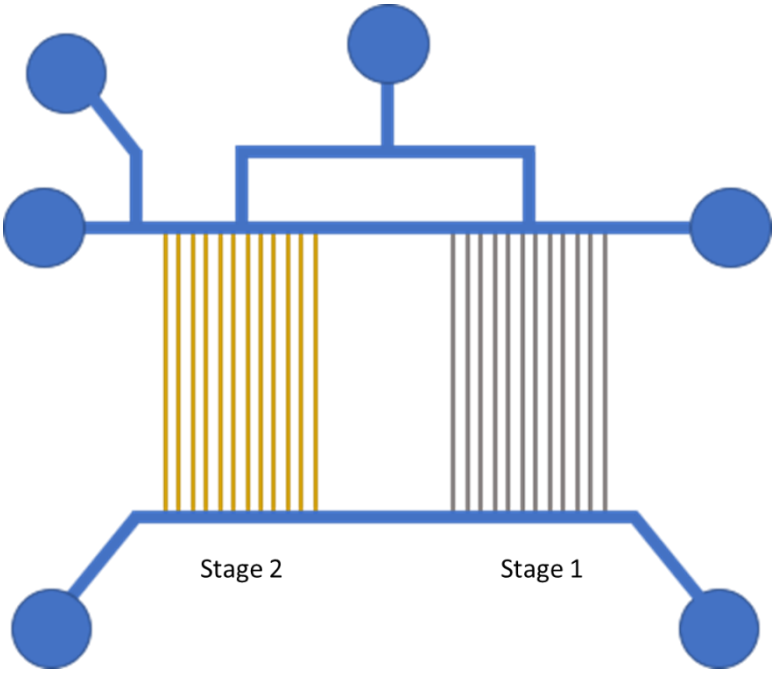

Figure 5.1 Schematic of the proposed dual-stage filtration. The two stages can have different slit height depending on the application.

A major bottleneck in the complete characterization of our device is the recovery of the filtered DNA from the device. This is less of an issue when it is used for our intended

applications in the field of genomics. Most of the genomic application are microfluidic-based and the current system can be easily integrated into the upstream, thus eliminating the need to recover the filtered DNA. As discussed in Chapter 2, the device performance was characterized by quantifying the filtration of different-sized DNA molecules under similar operating conditions and we demonstrated high selectivity for long DNA molecules as compared to short DNA fragments. Moving forward, it is important to characterize the device performance for specific application and genome mapping is the ideal application of this device. Confining DNA in nanochannels at laboratory scale is already well-established, including the device design, fabrication as well as experimental protocols.[159] The device design in Figure 5.2 is one way to combine our device with nanochannels and is already under trials in our group. This approach of incorporating the nanochannel at the downstream will not only help characterize the filtration performance; it can also be used for the genome mapping of clinical samples.

In addition to the size of the molecule, it must be negatively charged in order to be focused at the slit-channel interface during the filtration step. As the development work of this device is being focused towards genome mapping, this filtration system can have additional benefits for removing smaller biological entities such as RNA and proteins, which are also common impurities in a clinical sample along with short DNA fragments. This filtration system will also be advantageous to remove free dye molecules from the solution that are difficult to remove during chemical processes. Free dyes are often removed using drop-dialysis, but it causes further fragmentation during pipetting as well

as

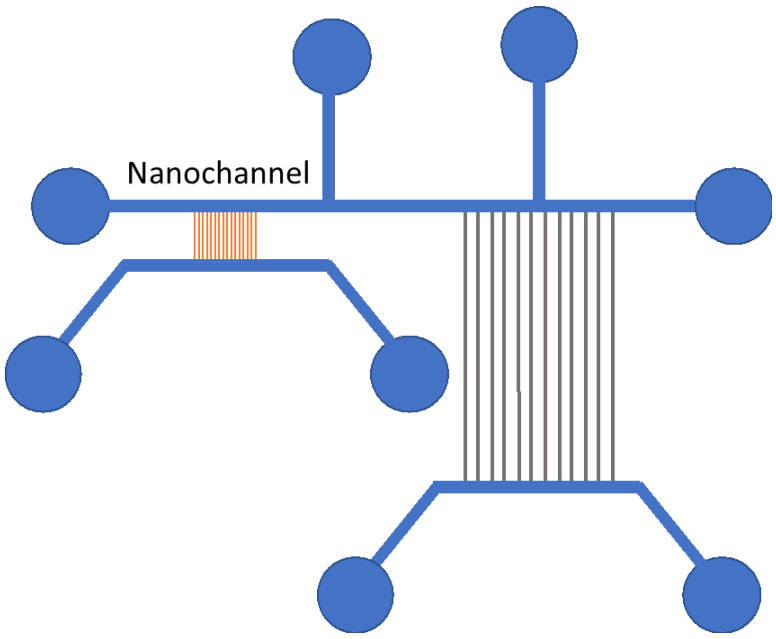

Figure 5.2 The proposed device for incorporating nanochannel with the filtration system for genome mapping applications. This device is being fabricated and tested in our group by Hui-Min Chuang.

sample loss. Molecules such as ChromaTide™ Alexa Fluor™ 546-14-dUTP, commonly used for labelling long DNA, are also negatively charged and can be filtered out using our filtration method.[77]

5.2 Fast, efficient and gentle transfection of human adherent cells in suspension

Our work discussed in Chapter 3 highlights the different time scales involved in the delivery of non-viral gene delivery and demonstrates its use to expedite the delivery process. Recently, this idea was further explored by another research group, to deliver plasmid in mouse embryonic stem cells in suspension within 5 minutes of transfection

time.[160] As the field progresses from the proof-of-concept experiments towards its clinical application, it will be necessary to adopt the protocol for more practical applications such as large-scale manufacturing.

Non-viral delivery vehicles have the advantage of large payload, low cytotoxicity, low production cost, and easy manufacturing scalability, but they face several challenges such as low colloidal stability, short half-life, low delivery efficiency, and long delivery time. Our work described in Chapter 3 is a convenient way to expedite the delivery time through fast attachment of GDV to the cell surface. Furthermore, this can be useful to overcome the limitation of low efficiency by performing multiple transfections of the cell population.[161] The unique control on the delivery of GDV at a single cell level achieved through microfluidic-based transfection in our work will be very useful for gene editing applications, especially for the CRISPR-Cas9 system, where high copy number may cause undesirable off-target editing. Sequential delivery of different payloads for gene editing can also be easily achieved with our protocol. A major challenge in translating our current protocol for multiple transfections is the ability to maintain cell viability of adherent cells in suspension. For single transfection, we addressed this issue by performing the attachment step quickly (<1 minute in the microfluidic system) and replacing it into fresh culture media. However, in the context of multiple transfections, a major challenge will be to detach cells from the solid surface for suspension transfection multiple times. Such a fast change in cell physiology will be detrimental to cells and may increase cytotoxicity. Another difficulty with current commercial transfection reagents is the low colloidal

stability of delivery vehicles in serum-rich media. Therefore, many of these transfection protocols require less-favorable media condition for transfection and the transfected cells are replaced with serum-containing media for the intracellular trafficking of GDVs.

The advancement of the new protocol to clinical application will require its integration with the usage of microcarrier that supports a sustainable culture of anchorage-dependent mammalian cells in suspension. Microcarrier has been a popular choice in the pharmaceutical industry for the large-scale production of vaccine and biologics. Large development work on microcarrier is already available for the cell culture applications, including size, materials, porosity and surface properties. Many soluble microcarriers have also been commercialized for such applications.[162] Adaptation of microcarriers for gene delivery purposes is in its early stages, as shown in Figure 5.3,[163] and is expected to be more widely used for gene-based therapy. Continuous microcarrier-based culture is already being adopted in a microfluidic system.[164] We envision the new design for integrating microcarrier with our protocol to involve three stages: (i) gradual replacement of serum-rich media with appropriate transfection condition; (ii) mixing of carriers with delivery vehicles and; (iii) finally replacing transfection media with fresh culture media for normal culture. This can be done both with the bulk system, similar to that shown in Figure 5.3, or a continuous microfluidic reactor that can be designed to achieve short contact time. From the delivery point of view, solid microcarriers will be preferable with low cell confluency to achieve higher delivery performance.

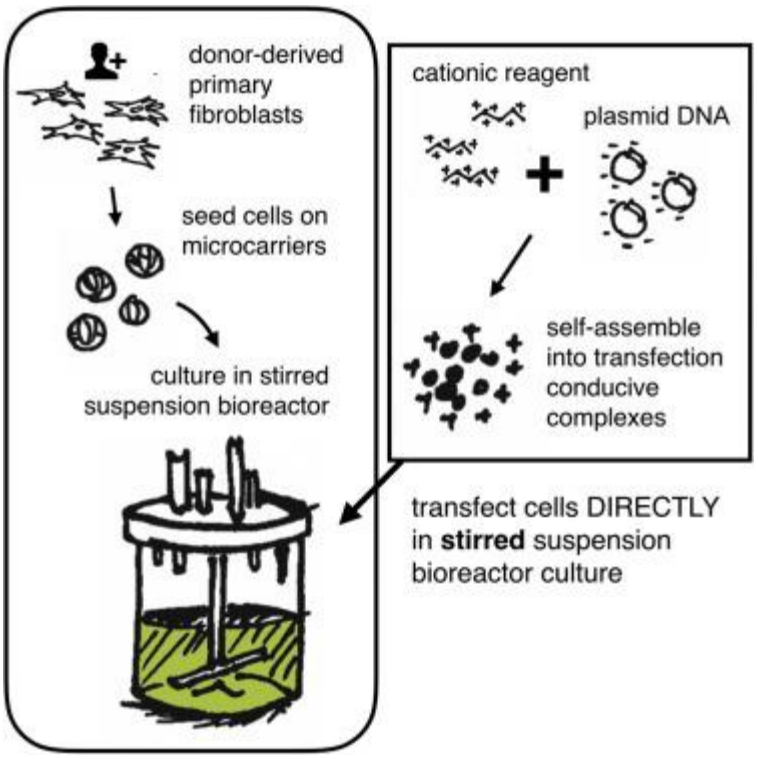

Figure 5.3 Schematic shows the integration of microcarriers and gene delivery for large scale manufacturing. It can be further improved by incorporating our protocol and microfluidic system. Figure was adapted from *Molecular Therapy - Methods and Clinical Development.*[161]

5.3 Micro-engineered cell culture system as a human gut model

Chapter 5 is an excellent example of how to adapt an existing design to build the tools necessary for a study. We demonstrated in chapter 5 that the dual-channel with controlled oxygen flux recapitulates some of the *in vivo* conditions and demonstrated its use for host-pathogen interaction for EHEC in a human epithelial cell system. As outlined in the chapter, these technological developments are not limited to the EHEC pathogen but can have a more general impact on the study of the role of microbiota in human health. We have further outlined some of the immediate future directions in terms of the device

modification and its impact on the ease in investigating the host-pathogen interaction in an *in vivo*-like environment. Several types of research are actively underway to develop gut models to support drug discovery and have huge potential to expedite developmental works in the pharmaceutical industry.[165] These opportunities include target identification and validation, drug screening for hit-to-lead and lead optimization, and modelling of pharmacokinetic processes that govern drug bioavailability.

An application in the field of drug discovery that can be benefited by the gut model is the screening of the polymer excipient, as well as evaluating the bioavailability of oral drugs for different excipient systems. The majority of oral drugs are either hydrophobic or crystalline in pure form and thus precipitate out of the aqueous solution. This requires high or multiple dosages for effective therapeutic response. One way to overcome this limitation is the use of excipient to improve the solubility of the drug in aqueous solutions. The solubility often increases due to the complexation of the drug with the excipient molecule and the strength of this complexation is critical for its absorption by the GI tract. For the drug to be effective, it should be available in free-form for uptake. If the strength of binding with the excipient is very strong, this may not be possible. For the screening of the excipients, the first step is to evaluate the solubility profile in a gut-simulating fluid. However, the bioavailability of drug due to its enhanced solubility can only be tested through cell-based *in vitro* model or animal studies. As discussed in Chapter 5, better *in vitro* models are necessary to reduce the depends on animal model as well as to have a better prediction for clinical studies.

Permeability assay on the gut-on-a-chip model will be an important tool for the fast screening of excipient. The requirement for this model will be more stringent than the one we have demonstrated in Chapter 5. The barrier properties of the cell layer for the device has to be similar to that of the GI tract. Two ways to characterize the barrier properties are transepithelial electrical resistance (TEER) and permeability of inert dye.[166] Both methods have been employed as gut models,[134,167] but require further optimization in terms of their adaptability for in-situ validation with culture media. The microfluidic gut model provides significant improvement over static trans-well system for investigating the role of fluid flow and actual drug dosage on the permeability as well as bioavailability of a drug on the blood side.

In conclusion, these are exciting time for the advancements of microfluidics in the field of biotechnology. As chemical engineers, we are uniquely trained in the integration of fundamental of engineering principles such as transport phenomena, reaction engineering, and polymer physics in microfluidic system for biological and life science applications. This thesis has detailed some of these advancements and envision more developmental work in the near future, both academically as well as commercially.

Chapter 6 – Bibliography

(1) Sackmann, E. K.; Fulton, A. L.; Beebe, D. J. The Present and Future Role of Microfluidics in Biomedical Research. *Nature* **2014**, *507* (7491), 181–189.

(2) Hanna, R.; Gross, R.; Speirs, J.; Heptonstall, P.; Gambhir, A. *Innovation Timelines from Invention to Maturity*; 2015.

(3) Volpatti, L. R.; Yetisen, A. K. Commercialization of Microfluidic Devices. *Trends Biotechnol.* **2014**, *32*, 347–350.

(4) Pandey, C. M.; Augustine, S.; Kumar, S.; Kumar, S.; Nara, S.; Srivastava, S.; Malhotra, B. D. Microfluidics Based Point-of-Care Diagnostics. *Biotechnol. J.* **2018**, *13* (1), 1700047.

(5) Ohno, K. I.; Tachikawa, K.; Manz, A. Microfluidics: Applications for Analytical Purposes in Chemistry and Biochemistry. *Electrophoresis* **2008**, *29* (22), 4443–4453.

(6) El-Ali, J.; Sorger, P. K.; Jensen, K. F. Cells on Chips. *Nature* **2006**, *442* (7101), 403–411.

(7) Chiu, D. T.; DeMello, A. J.; Di Carlo, D.; Doyle, P. S.; Hansen, C.; Maceiczyk, R. M.; Wootton, R. C. R. Small but Perfectly Formed? Successes, Challenges, and Opportunities for Microfluidics in the Chemical and Biological Sciences. *Chem* **2017**, *2* (2), 201–223.

(8) Mancera-Andrade, E. I.; Parsaeimehr, A.; Arevalo-Gallegos, A.; Ascencio-Favela, G.; Parra Saldivar, R. Microfluidics Technology for Drug Delivery: A Review. *Front. Biosci. (Elite Ed).* **2018**, *10*, 74–91.

(9) Shields, C. W.; Reyes, C. D.; López, G. P. Microfluidic Cell Sorting: A Review of the Advances in the Separation of Cells from Debulking to Rare Cell Isolation. *Lab Chip* **2015**, *15* (5), 1230–1249.

(10) Ugaz, V. M.; Christensen, J. L. Electrophoresis in Microfluidic Systems. In *Microfluidic Technologies for Miniaturized Analysis Systems*; Springer US: Boston, MA, 2007; pp 393–438.

(11) Beebe, D. J.; Mensing, G. A.; Walker, G. M. Physics and Applications of Microfluidics in Biology. *Annu. Rev. Biomed. Eng.* **2002**, *4* (1), 261–286.

(12) Ahrberg, C. D.; Manz, A.; Chung, B. G. Polymerase Chain Reaction in Microfluidic Devices. *Lab Chip* **2016**, *16* (20), 3866–3884.

(13) Mashaghi, S.; Abbaspourrad, A.; Weitz, D. A.; van Oijen, A. M. Droplet Microfluidics: A Tool for Biology, Chemistry and Nanotechnology. *TrAC - Trends Anal. Chem.* **2016**, *82*, 118–125.

(14) Lan, F.; Demaree, B.; Ahmed, N.; Abate, A. R. Single-Cell Genome Sequencing at Ultra-High-Throughput with Microfluidic Droplet Barcoding. *Nat. Biotechnol.* **2017**, *35* (7), 640–646.

(15) Bazant, M. Z.; Squires, T. M. Induced-Charge Electrokinetic Phenomena: Theory and Microfluidic Applications. *Phys. Rev. Lett.* **2004**, *92* (6), 1–4.

(16) Ren, K.; Zhou, J.; Wu, H. Materials for Microfluidic Chip Fabrication. *Acc. Chem. Res.* **2013**, *46* (11), 2396–2406.

(17) McDonald, J. C.; Whitesides, G. M. Poly(Dimethylsiloxane) as a Material for Fabricating Microfluidic Devices. *Acc. Chem. Res.* **2002**, *35* (7), 491–499.

(18) Zhou, J.; Ellis, A. V.; Voelcker, N. H. Recent Developments in PDMS Surface Modification for Microfluidic Devices. *Electrophoresis* **2010**, *31* (1), 2–16.

(19) Inglis, D. W. A Method for Reducing Pressure-Induced Deformation in Silicone Microfluidics. *Biomicrofluidics* **2010**, *4* (2), 026504.

(20) Sun, X.; Peeni, B. A.; Yang, W.; Becerril, H. A.; Woolley, A. T. Rapid Prototyping of Poly(Methyl Methacrylate) Microfluidic Systems Using Solvent Imprinting and Bonding. *J. Chromatogr. A* **2007**, *1162* (2 SPEC. ISS.), 162–166.

(21) Aghvami, S. A.; Opathalage, A.; Zhang, Z. K.; Ludwig, M.; Heymann, M.; Norton, M.; Wilkins, N.; Fraden, S. Rapid Prototyping of Cyclic Olefin Copolymer (COC) Microfluidic Devices. *Sensors Actuators B Chem.* **2017**, *247*, 940–949.

(22) Ogończyk, D.; Węgrzyn, J.; Jankowski, P.; Dąbrowski, B.; Garstecki, P. Bonding of Microfluidic Devices Fabricated in Polycarbonate. *Lab Chip* **2010**, *10* (10), 1324.

(23) Iliescu, C.; Taylor, H.; Avram, M.; Miao, J.; Franssila, S. A Practical Guide for the Fabrication of Microfluidic Devices Using Glass and Silicon. *Biomicrofluidics* **2012**, *6* (1), 16505–1650516.

(24) Lima, R. S.; Carneiro Leão, P. A. G.; Monteiro, A. M.; de Oliveira Piazzetta, M. H.; Gobbi, A. L.; Mazo, L. H.; Carrilho, E. Glass/SU-8 Microchip for Electrokinetic Applications. *Electrophoresis* **2013**, *34* (20–21), 2996–3002.

(25) Stjernström, M.; Roeraade, J. Method for Fabrication of Microfluidic Systems in Glass. *J. Micromechanics Microengineering* **1998**, *8* (1), 33–38.

(26) Chen, Q.; Li, G.; Jin, Q. H.; Zhao, J. L.; Ren, Q. S.; Xu, Y. Sen. A Rapid and Low-Cost Procedure for Fabrication of Glass Microfluidic Devices. *J. Microelectromechanical Syst.* **2007**, *16* (5), 1193–1200.

(27) Ho, C. M. B.; Ng, S. H.; Li, K. H. H.; Yoon, Y. J. 3D Printed Microfluidics for Biological Applications. *Lab Chip* **2015**, *15* (18), 3627–3637.

(28) Waheed, S.; Cabot, J. M.; Macdonald, N. P.; Lewis, T.; Guijt, R. M.; Paull, B.; Breadmore, M. C. 3D Printed Microfluidic Devices: Enablers and Barriers. *Lab Chip* **2016**, *16* (11), 1993–2013.

(29) Agrawal, P.; Bognár, Z.; Dorfman, K. D. Entropic Trap Purification of Long DNA. *Lab Chip* **2018**, *18* (6), 955–964.

(30) Agrawal, P.; Ingle, N. P.; Boyle, W. S.; Ward, E.; Tolar, J.; Dorfman, K. D.; Reineke, T. M. Fast, Efficient, and Gentle Transfection of Human Adherent Cells in Suspension. *ACS Appl. Mater. Interfaces* **2016**, *8* (14), 8870–8874.

(31) Heather, J. M.; Chain, B. The Sequence of Sequencers: The History of Sequencing DNA. *Genomics* **2016**, *107* (1), 1–8.

(32) The Cost of Sequencing a Human Genome - National Human Genome Research Institute (NHGRI) https://www.genome.gov/27565109/the-cost-of-sequencing-a-human-genome/ (accessed Nov 12, 2017).

(33) Neely, R. K.; Deen, J.; Hofkens, J. Optical Mapping of DNA: Single-Molecule-Based Methods for Mapping Genomes. *Biopolymers* **2011**, *95* (5), 298–311.

(34) Howe, K.; Wood, J. M. Using Optical Mapping Data for the Improvement of Vertebrate Genome Assemblies. *Gigascience* **2015**, *4* (1), 10.

(35) Bogas, D.; Nyberg, L.; Pacheco, R.; Azevedo, N. F.; Beech, J. P.; Gomila, M.; Lalucat, J.; Manaia, C. M.; Nunes, O. C.; Tegenfeldt, J. O.; et al. Applications of Optical DNA Mapping in Microbiology. *Biotechniques* **2017**, *62* (6), 255–267.

(36) Michaeli, Y.; Ebenstein, Y. Channeling DNA for Optical Mapping. *Nat. Biotechnol.* **2012**, *30* (8), 762–763.

(37) Eid, J.; Fehr, A.; Gray, J.; Luong, K.; Lyle, J.; Otto, G.; Peluso, P.; Rank, D.; Baybayan, P.; Bettman, B.; et al. Real-Time DNA Sequencing from Single Polymerase Molecules. *Science* **2009**, *323* (5910), 133–138.

(38) Baker, M. De Novo Genome Assembly: What Every Biologist Should Know. *Nat. Methods* **2012**, *9* (4), 333–337.

(39) Viovy, J. L. Electrophoresis of DNA and Other Polyelectrolytes: Physical Mechanisms. *Rev. Mod. Phys.* **2000**, *72* (3), 813–872.

(40) Reed, K. D.; Stemper, M. E.; Shukla, S. K. Pulsed-Field Gel Electrophoresis of MRSA. *Methods Mol. Biol.* **2007**, *391* (1), 59–69.

(41) Barron, A. E.; Heller, C. Influence of Polymer Concentration and Electric Field Experimental Study and Comparison with Theory. In *Analysis of Nucleic Acids by Capillary Electrophoresis*; Springer Fachmedien Wiesbaden, 1997; pp 93–124.

(42) Fangman, W. L. Separation of Very Large DNA Molecules by Gel Electrophoresis. *Nucleic Acids Res.* **1978**, *5* (3), 653–665.

(43) Viovy, J. L. Pulsed Electrophoresis: Some Implications of Reptation Theories. *Biopolymers* **1987**, *26* (11), 1929–1940.

(44) Kovacic, R. T.; Comal, L.; Bendich, A. J. Protection of Megabase DNA from Shearing. *Nucleic Acids Res.* **1995**, *23* (19), 3999–4000.

(45) Schneider, G. F.; Dekker, C. DNA Sequencing with Nanopores. *Nat. Biotechnol.* **2012**, *30* (4), 326–328.

(46) Feng, Y.; Zhang, Y.; Ying, C.; Wang, D.; Du, C. Nanopore-Based Fourth-Generation DNA Sequencing Technology. *Genomics Proteomics Bioinforma.* **2015**, *13* (1), 4–16.

(47) Lam, E. T.; Hastie, A.; Lin, C.; Ehrlich, D.; Das, S. K.; Austin, M. D.; Deshpande, P.; Cao, H.; Nagarajan, N.; Xiao, M.; et al. Genome Mapping on Nanochannel Arrays for Structural Variation Analysis and Sequence Assembly. *Nat. Biotechnol.* **2012**, *30* (8), 771–776.

(48) Dorfman, K. D.; King, S. B.; Olson, D. W.; Thomas, J. D. P.; Tree, D. R. Beyond Gel Electrophoresis : Micro Fl Uidic Separations , Fluorescence Burst Analysis , and DNA Stretching. *Chem. Rev.* **2013**, *113* (4), 2584–2667.

(49) Dorfman, K. D. DNA Electrophoresis in Microfluidic Post Arrays under Moderate Electric Fields. *Phys. Rev. E - Stat. Nonlinear, Soft Matter Phys.* **2006**, *73* (6), 1–10.

(50) Han, J.; Fu, J.; Schoch, R. B. Molecular Sieving Using Nanofilters: Past, Present and Future. *Lab Chip* **2008**, *8* (1), 23–33.

(51) Han, J.; Craighead, H. G. Separation of Long DNA Molecules in a Microfabricated Entropic Trap Array. *Science* **2000**, *288* (5468), 1026–1029.

(52) Huang, L. R.; Tegenfeldt, J. O.; Kraeft, J. J.; Sturm, J. C.; Austin, R. H.; Cox, E. C. A DNA Prism for High-Speed Continuous Fractionation of Large DNA Molecules. *Nat. Biotechnol.* **2002**, *20* (10), 1048–1051.

(53) Rahong, S.; Yasui, T.; Yanagida, T.; Nagashima, K.; Kanai, M.; Klamchuen, A.; Meng, G.; He, Y.; Zhuge, F.; Kaji, N.; et al. Ultrafast and Wide Range Analysis of DNA Molecules Using Rigid Network Structure of Solid Nanowires. *Sci. Rep.* **2014**, *4*, 5252.

(54) Zhang, H.; Wirth, M. J. Electromigration of Single Molecules of DNA in a Crystalline Array of 300-Nm Silica Colloids. *Anal. Chem.* **2005**, *77* (5), 1237–1242.

(55) Shi, N.; Ugaz, V. M. Noise-Enhanced Gel Electrophoresis. *Electrophoresis* **2014**, *35* (12–13), 1758–1765.

(56) Jones, P. V.; Salmon, G. L.; Ros, A. Continuous Separation of DNA Molecules by Size Using Insulator-Based Dielectrophoresis. *Anal. Chem.* **2017**, *89* (3), 1531–1539.

(57) Kühnlein, A. Handling of Long DNA – Applications and Polymer Physics, Lund University, 2016.

(58) Muthukumar, M.; Baumgärtner, A. Effects of Entropic Barriers on Polymer Dynamics. *Macromolecules* **1989**, *22* (4), 1937–1941.

(59) Rousseau, J.; Drouin, G.; Slater, G. W. Entropic Trapping of DNA during Gel Electrophoresis: Effect of Field Intensity and Gel Concentration. *Phys. Rev. Lett.* **1997**, *79*, 1945–1948.

(60) Shi, N.; Ugaz, V. M. Tailoring the Nnoporous Architecture of Hydrogels to Exploit Entropic Trapping. *Phys. Rev. Lett.* **2010**, *105* (10), 108101.

(61) Han, J.; Turner, S.; Craighead, H. Entropic Trapping and Escape of Long DNA Molecules at Submicron Size Constriction. *Phys. Rev. Lett.* **1999**, *83*, 1688–1691.

(62) Duan, L.; Cao, Z.; Yobas, L. Continuous-Flow Electrophoresis of DNA and Proteins in a Two-Dimensional Capillary-Well Sieve. *Anal. Chem.* **2017**, *89* (18), 10022–10028.

(63) Fu, J.; Schoch, R. B.; Stevens, A. L.; Tannenbaum, S. R.; Han, J. A Patterned Anisotropic Nanofluidic Sieving Structure for Continuous-Flow Separation of DNA

and Proteins. *Nat. Nanotechnol.* **2007**, *2* (2), 121–128.

(64) Han, J.; Craighead, H. G. Characterization and Optimization of an Entropic Trap for DNA Separation. *Anal. Chem.* **2002**, *74* (2), 394–401.

(65) Thomas, J. D. P.; Joswiak, M. N.; Olson, D. W.; Park, S.-G.; Dorfman, K. D. Ratchet Nanofiltration of DNA. *Lab Chip* **2013**, *13* (18), 3741–3746.

(66) Wu, Q.; Kaji, N.; Yasui, T.; Rahong, S.; Yanagida, T.; Kanai, M.; Nagashima, K.; Tokeshi, M.; Kawai, T.; Baba, Y. A Millisecond Micro-RNA Separation Technique by a Hybrid Structure of Nanopillars and Nanoslits. *Sci. Rep.* **2017**, *7*, 43877.

(67) Wu, L.; Levy, S. Fluctuations of DNA Mobility in Nanofluidic Entropic Traps. *Biomicrofluidics* **2014**, *8* (4), 044103.

(68) Fu, J.; Yoo, J.; Han, J. Molecular Sieving in Periodic Free-Energy Landscapes Created by Patterned Nanofilter Arrays. *Phys. Rev. Lett.* **2006**, *97* (1), 1–4.

(69) Wong, C. T. A.; Muthukumar, M. Scaling Theory of Polymer Translocation into Confined Regions. *Biophys. J.* **2008**, *95* (8), 3619–3627.

(70) Chen, Z.; Escobedo, F. a. Simulation of Chain-Length Partitioning in a Microfabricated Channel via Entropic Trapping. *Mol. Simul.* **2003**, *29* (6–7), 417–425.

(71) Muthukumar, M. Translocation of a Confined Polymer through a Hole. *Phys. Rev. Lett.* **2001**, *86* (14), 3188–3191.

(72) Han, J.; Craighead, H. G. Entropic Trapping and Sieving of Long DNA Molecules in a Nanofluidic Channel. *J. Vac. Sci. Technol. A Vacuum, Surfaces, Film.* **1999**, *17* (4), 2142–2147.

(73) Gupta, D.; Sheats, J.; Muralidhar, A.; Miller, J. J.; Huang, D. E.; Mahshid, S.; Dorfman, K. D.; Reisner, W. Mixed Confinement Regimes during Equilibrium Confinement Spectroscopy of DNA. *J. Chem. Phys.* **2014**, *140* (21), 214901.

(74) Gupta, D.; Miller, J. J.; Muralidhar, A.; Mahshid, S.; Reisner, W.; Dorfman, K. D. Experimental Evidence of Weak Excluded Volume Effects for Nanochannel Confined DNA. *ACS Macro Lett.* **2015**, *4* (7), 759–763.

(75) Persson, F.; Utko, P.; Reisner, W.; Larsen, N. B.; Kristensen, A. Confinement Spectroscopy: Probing Single DNA Molecules with Tapered Nanochannels. *Nano Lett.* **2009**, *9* (4), 1382–1385.

(76) Reisner, W.; Larsen, N. B.; Silahtaroglu, A.; Kristensen, A.; Tommerup, N.; Tegenfeldt, J. O.; Flyvbjerg, H. Single-Molecule Denaturation Mapping of DNA in Nanofluidic Channels. *Proc. Natl. Acad. Sci.* **2010**, *107* (30), 13294–13299.

(77) Persson, F.; Tegenfeldt, J. O. DNA in Nanochannels—directly Visualizing Genomic Information. *Chem. Soc. Rev.* **2010**, *39* (3), 985–999.

(78) Panwar, A. S.; Kumar, S. Time Scales in Polymer Electrophoresis through Narrow Constrictions: A Brownian Dynamics Study. *Macromolecules* **2006**, *39* (3), 1279–1289.

(79) Stellwagen, N. C.; Gelfi, C.; Righetti, P. G. The Free Solution Mobility of DNA. *Biopolymers* **1997**, *42* (6), 687–703.

(80) Long, D.; Viovy, J. L.; Ajdari, A. Simultaneous Action of Electric Fields and Nonelectric Forces on a Polyelectrolyte: Motion and Deformation. *Phys. Rev. Lett.* **1996**, *76* (20), 3858–3861.

(81) Tessier, F.; Labrie, J.; Slater, G. W. Electrophoretic Separation of Long Polyelectrolytes in Submolecular-Size Constrictions: A Monte Carlo Study. *Macromolecules* **2002**, *35* (12), 4791–4800.

(82) Tree, D. R.; Muralidhar, A.; Doyle, P. S.; Dorfman, K. D. Is DNA a Good Model Polymer? *Macromolecules* **2013**, *46* (20), 8369–8382.

(83) Nyberg, L.; Persson, F.; Åkerman, B.; Westerlund, F. Heterogeneous Staining: A Tool for Studies of How Fluorescent Dyes Affect the Physical Properties of DNA. *Nucleic Acids Res.* **2013**, *41* (19), e184–e184.

(84) Edelstein, A. D.; Tsuchida, M. A.; Amodaj, N.; Pinkard, H.; Vale, R. D.; Stuurman, N. Advanced Methods of Microscope Control Using MManager Software. *J. Biol. Methods* **2014**, *1* (2), e10.

(85) Edelstein, A.; Amodaj, N.; Hoover, K.; Vale, R.; Stuurman, N. Computer Control of Microscopes Using Manager. *Current Protocols in Molecular Biology*. 2010, p 14.20.1-14.20.17.

(86) Ma, H.; Graham, M. D. Theory of Shear-Induced Migration in Dilute Polymer Solutions near Solid Boundaries. *Phys. Fluids* **2005**, *17* (8), 1–13.

(87) Ou, J.; Carpenter, S. J.; Dorfman, K. D. Onset of Channeling during DNA Electrophoresis in a Sparse Ordered Post Array. *Biomicrofluidics* **2010**, *4* (1), 1–4.

(88) Tolar, J.; Xia, L.; Riddle, M. J.; Lees, C. J.; Eide, C. R.; McElmurry, R. T.; Titeux,

M.; Osborn, M. J.; Lund, T. C.; Hovnanian, A.; et al. Induced Pluripotent Stem Cells from Individuals with Recessive Dystrophic Epidermolysis Bullosa. *J. Invest. Dermatol.* **2011**, *131* (4), 848–856.

(89) Sander, J. D.; Joung, J. K. CRISPR-Cas Systems for Editing, Regulating and Targeting Genomes. *Nat. Biotechnol.* **2014**, *32* (4), 347–355.

(90) Yin, H.; Kanasty, R. L.; Eltoukhy, A. A.; Vegas, A. J.; Dorkin, J. R.; Anderson, D. G. Non-Viral Vectors for Gene-Based Therapy. *Nat. Rev. Genet.* **2014**, *15* (8), 541–555.

(91) Tayi, V. S.; Bowen, B. D.; Piret, J. M. Mathematical Model of the Rate-Limiting Steps for Retrovirus-Mediated Gene Transfer Into Mammalian Cells. *Biotechnol. Bioeng.* **2010**, *105* (1), 195–209.

(92) Banks, G. a; Roselli, R. J.; Chen, R.; Giorgio, T. D. A Model for the Analysis of Nonviral Gene Therapy. *Gene Ther.* **2003**, *10* (20), 1766–1775.

(93) Jones, C. H.; Chen, C.-K.; Ravikrishnan, A.; Rane, S.; Pfeifer, B. A. Overcoming Nonviral Gene Delivery Barriers: Perspective and Future. *Mol. Pharm.* **2013**, *10* (11), 4082–4098.

(94) Chuck, A. S.; Clarke, M. F.; Palsson, B. O. Retroviral Infection Is Limited by Brownian Motion. *Hum. Gene Ther.* **1996**, *7*, 1527–1534.

(95) Wang, T.; Wang, J.; Jin, Y. Slurry Reactors for Gas-to-Liquid Processes: A Review. *Ind. Eng. Chem. Res.* **2007**, *46* (18), 5824–5847.

(96) Fluri, D. A.; Tonge, P. D.; Song, H.; Baptista, R. P.; Shakiba, N.; Shukla, S.; Clarke, G.; Nagy, A.; Zandstra, P. W. Derivation, Expansion and Differentiation of Induced Pluripotent Stem Cells in Continuous Suspension Cultures. *Nat. Methods* **2012**, *9* (5), 509–516.

(97) Covello, G.; Siva, K.; Adami, V.; Denti, M. a. An Electroporation Protocol for Efficient DNA Transfection in PC12 Cells. *Cytotechnology* **2014**, *66* (4), 543–553.

(98) Riddell, J.; Gazit, R.; Garrison, B. S.; Guo, G.; Saadatpour, A.; Mandal, P. K.; Ebina, W.; Volchkov, P.; Yuan, G.-C.; Orkin, S. H.; et al. Reprogramming Committed Murine Blood Cells to Induced Hematopoietic Stem Cells with Defined Factors. *Cell* **2014**, *157* (3), 549–564.

(99) El-Sayed, A.; Harashima, H. Endocytosis of Gene Delivery Vectors: From Clathrin-Dependent to Lipid Raft-Mediated Endocytosis. *Mol. Ther.* **2013**, *21* (6), 1118–1130.

(100) Srinivasachari, S.; Liu, Y.; Zhang, G.; Prevette, L.; Reineke, T. M. Trehalose Click Polymers Inhibit Nanoparticle Aggregation and Promote PDNA Delivery in Serum. *J. Am. Chem. Soc.* **2006**, *128* (25), 8176–8184.

(101) Duffy, D. C.; McDonald, J. C.; Schueller, O. J. A.; Whitesides, G. M. Rapid Prototyping of Microfluidic Systems in Poly(Dimethylsiloxane). *Anal. Chem.* **1998**, *70* (23), 4974–4984.

(102) Gilleland, C. L.; Rohde, C. B.; Zeng, F.; Yanik, M. F. Microfluidic Immobilization of Physiologically Active Caenorhabditis Elegans. *Nat. Protoc.* **2010**, *5* (12), 1888–1902.

(103) Yemin, L.; Reineke, T. M. Poly(Glycoamidoamine)s for Gene Delivery: Stability of Polyplexes and Efficacy with Cardiomyoblast Cells. *Bioconjug. Chem.* **2005**, *17* (1), 101–108.

(104) Fichter, K. M.; Ingle, N. P.; Mclendon, P. M.; Reineke, T. M. Exploit Active Interorganelle Trafficking Mechanisms. *ACS Nano* **2013**, *7* (1), 347–364.

(105) Grandinetti, G.; Reineke, T. M. Exploring the Mechanism of Plasmid DNA Nuclear Internalization with Polymer-Based Vehicles. *Mol. Pharm.* **2012**, *9* (8), 2256–2267.

(106) Grandinetti, G.; Smith, A. E.; Reineke, T. M. Membrane and Nuclear Permeabilization by Polymeric PDNA Vehicles: Efficient Method for Gene Delivery or Mechanism of Cytotoxicity? *Mol. Pharm.* **2012**, *9* (3), 523–538.

(107) Bostock, C. J.; Prescott, D. M.; Kirkpatrick, J. B. An Evaluation of the Double Thymidine Block for Synchronizing Mammalian Cells at the G1-S Border. *Exp. Cell Res.* **1971**, *68* (1), 163–168.

(108) Di Carlo, D. Inertial Microfluidics. *Lab Chip* **2009**, *9* (21), 3038–3046.

(109) Arnold, J. W.; Roach, J.; Azcarate-Peril, M. A. Emerging Technologies for Gut Microbiome Research. *Trends in Microbiology*. Elsevier Current Trends November 1, 2016, pp 887–901.

(110) Fritz, J. V; Desai, M. S.; Shah, P.; Schneider, J. G.; Wilmes, P. From Meta-Omics to Causality: Experimental Models for Human Microbiome Research. *Microbiome* **2013**, *1* (1), 14.

(111) Lupp, C.; Robertson, M. L.; Wickham, M. E.; Sekirov, I.; Champion, O. L.; Gaynor, E. C.; Finlay, B. B. Host-Mediated Inflammation Disrupts the Intestinal Microbiota and Promotes the Overgrowth of Enterobacteriaceae. *Cell Host Microbe* **2007**, *2* (2), 119–129.

(112) Wilson, K. H.; Silva, J.; Fekety, F. R. Suppression of Clostridium Difficile by Normal Hamster Cecal Flora and Prevention of Antibiotic-Associated Cecitis. *Infect. Immun.* **1981**, *34* (2), 626–628.

(113) Ridaura, V. K.; Faith, J. J.; Rey, F. E.; Cheng, J.; Alexis, E.; Kau, A. L.; Griffin, N. W.; Lombard, V.; Henrissat, B.; Bain, J. R.; et al. Cultured Gut Microbiota from Twins Discordant for Obesity Modulate Adiposity and Metabolic Phenotypes in Mice. *Science (80-.).* **2014**, *341* (6150), 1–22.

(114) *The Impact of Food Bioactives on Health: In Vitro and Ex Vivo Models*; Verhoeckx, K., Cotter, P., López-Expósito, I., Kleiveland, C., Lea, T., Mackie, A., Requena, T., Swiatecka, D., Wichers, H., Ed.; Springer US, 2015.

(115) Tilg, H.; Adolph, T. E.; Gerner, R. R.; Moschen, A. R. The Intestinal Microbiota in Colorectal Cancer. *Cancer Cell* **2018**, *33* (6), 954–964.

(116) Enright, E. F.; Gahan, C. G. M.; Joyce, S. A.; Griffin, B. T. The Impact of the Gut Microbiota on Drug Metabolism and Clinical Outcome. *Yale J. Biol. Med.* **2016**, *89* (3), 375–382.

(117) Wilkinson, E. M.; Ilhan, Z. E.; Herbst-Kralovetz, M. M. Microbiota–drug Interactions: Impact on Metabolism and Efficacy of Therapeutics. *Maturitas* **2018**, *112*, 53–63.

(118) Wilson, I. D.; Nicholson, J. K. Gut Microbiome Interactions with Drug Metabolism, Efficacy, and Toxicity. *Transl. Res.* **2017**, *179*, 204–222.

(119) Gopalakrishnan, V.; Spencer, C. N.; Nezi, L.; Reuben, A.; Andrews, M. C.; Karpinets, T. V; Prieto, P. A.; Vicente, D.; Hoffman, K.; Wei, S. C.; et al. Gut Microbiome Modulates Response to Anti-PD-1 Immunotherapy in Melanoma Patients. *Science* **2018**, *359* (6371), 97–103.

(120) Matson, V.; Fessler, J.; Bao, R.; Chongsuwat, T.; Zha, Y.; Alegre, M. L.; Luke, J. J.; Gajewski, T. F. The Commensal Microbiome Is Associated with Anti-PD-1 Efficacy in Metastatic Melanoma Patients. *Science* **2018**, *359* (6371), 104–108.

(121) Abt, M. C.; Artis, D. The Dynamic Influence of Commensal Bacteria on the Immune Response to Pathogens. *Curr. Opin. Microbiol.* **2013**, *16* (1), 4–9.

(122) Baümler, A. J.; Sperandio, V. Interactions between the Microbiota and Pathogenic Bacteria in the Gut. *Nature* **2016**, *535* (7610), 85–93.

(123) Jarvis, K. G.; Giron, J. A.; Jerse, A. E.; McDaniel, T. K.; Donnenberg, M. S.; Kaper, J. B. Enteropathogenic Escherichia Coli Contains a Putative Type III Secretion

System Necessary for the Export of Proteins Involved in Attaching and Effacing Lesion Formation. *Proc. Natl. Acad. Sci.* **1995**, *92* (17), 7996–8000.

(124) Carlson-Banning, K. M.; Sperandio, V. Catabolite and Oxygen Regulation of Enterohemorrhagic Escherichia Coli Virulence. *MBio* **2016**, *7* (6), e01852-16.

(125) Schüller, S.; Phillips, A. D. Microaerobic Conditions Enhance Type III Secretion and Adherence of Enterohaemorrhagic Escherichia Coli to Polarized Human Intestinal Epithelial Cells. *Environ. Microbiol.* **2010**, *12* (9), 2426–2435.

(126) Ando, H.; Abe, H.; Sugimoto, N.; Tobe, T. Maturation of Functional Type III Secreation Machinery by Activation of Anaerobic Respiration in Enterohaemorrhagic Escherichia Coli. *Microbiology* **2007**, *153* (2), 464–473.

(127) Curtis, M. M.; Hu, Z.; Klimko, C.; Narayanan, S.; Deberardinis, R.; Sperandio, V. The Gut Commensal Bacteroides Thetaiotaomicron Exacerbates Enteric Infection through Modification of the Metabolic Landscape. *Cell Host Microbe* **2014**, *16* (6), 759–769.

(128) Mundy, R.; MacDonald, T. T.; Dougan, G.; Frankel, G.; Wiles, S. Citrobacter Rodentium of Mice and Man. *Cell. Microbiol.* **2005**, *7* (12), 1697–1706.

(129) Duncombe, T. A.; Tentori, A. M.; Herr, A. E. Microfluidics: Reframing Biological Enquiry. *Nat. Rev. Mol. Cell Biol.* **2015**, *16* (9), 554–567.

(130) Bhatia, S. N.; Ingber, D. E. Microfluidic Organs-on-Chips. *Nat. Biotechnol.* **2014**, *32* (8), 760–772.

(131) Bein, A.; Shin, W.; Jalili-Firoozinezhad, S.; Park, M. H.; Sontheimer-Phelps, A.; Tovaglieri, A.; Chalkiadaki, A.; Kim, H. J.; Ingber, D. E. Microfluidic Organ-on-a-Chip Models of Human Intestine. *Cmgh* **2018**, *5* (4), 659–668.

(132) Shah, P.; Fritz, J. V.; Glaab, E.; Desai, M. S.; Greenhalgh, K.; Frachet, A.; Niegowska, M.; Estes, M.; Jäger, C.; Seguin-Devaux, C.; et al. A Microfluidics-Based in Vitro Model of the Gastrointestinal Human-Microbe Interface. *Nat. Commun.* **2016**, *7*, 1–15.

(133) Kim, H. J.; Huh, D.; Hamilton, G.; Ingber, D. E. Human Gut-on-a-Chip Inhabited by Microbial Flora That Experiences Intestinal Peristalsis-like Motions and Flow. *Lab Chip* **2012**, *12* (12), 2165–2174.

(134) Blundell, C.; Tess, E. R.; Schanzer, A. S. R.; Coutifaris, C.; Su, E. J.; Parry, S.; Huh, D. A Microphysiological Model of the Human Placental Barrier. *Lab Chip* **2016**, *16* (16), 3065–3073.

(135) Chen, L.-J.; Ito, S.; Kai, H.; Nagamine, K.; Nagai, N.; Nishizawa, M.; Abe, T.; Kaji, H. Microfluidic Co-Cultures of Retinal Pigment Epithelial Cells and Vascular Endothelial Cells to Investigate Choroidal Angiogenesis. *Sci. Rep.* **2017**, *7* (1), 3538.

(136) Ma, Y.-H. V.; Middleton, K.; You, L.; Sun, Y. A Review of Microfluidic Approaches for Investigating Cancer Extravasation during Metastasis. *Microsystems Nanoeng.* **2018**, *4*, 17104.

(137) Agarwal, A.; Goss, J. A.; Cho, A.; McCain, M. L.; Parker, K. K. Microfluidic Heart on a Chip for Higher Throughput Pharmacological Studies. *Lab Chip* **2013**, *13* (18), 3599–3608.

(138) Jang, K.-J.; Mehr, A. P.; Hamilton, G. a; McPartlin, L. a; Chung, S.; Suh, K.-Y.; Ingber, D. E. Human Kidney Proximal Tubule-on-a-Chip for Drug Transport and Nephrotoxicity Assessment. *Integr. Biol. (Camb).* **2013**, *5* (9), 1119–1129.

(139) Wilmer, M. J.; Ng, C. P.; Lanz, H. L.; Vulto, P.; Suter-Dick, L.; Masereeuw, R. Kidney-on-a-Chip Technology for Drug-Induced Nephrotoxicity Screening. *Trends Biotechnol.* **2016**, *34* (2), 156–170.

(140) Lee, P. J.; Hung, P. J.; Lee, L. P. An Artificial Liver Sinusoid with a Microfluidic Endothelial-like Barrier for Primary Hepatocyte Culture. *Biotechnol. Bioeng.* **2007**, *97* (5), 1340–1346.

(141) Huh, D.; Matthews, B. D.; Mammoto, A.; Hsin, H. Y.; Ingber, D. E. Reconstituting Organ-Level Lung Functions on a Chip. *Science* **2010**, *328*, 1662–1668.

(142) Evaldson, G.; Heimdahl, A.; Kager, L.; Nord, C. E. The Normal Human Anaerobic Microflora. *Scand. J. Infect. Dis. Suppl.* **1982**, *35*, 9–15.

(143) Marteyn, B.; Scorza, F. B.; Sansonetti, P. J.; Tang, C. Breathing Life into Pathogens: The Influence of Oxygen on Bacterial Virulence and Host Responses in the Gastrointestinal Tract. *Cell. Microbiol.* **2011**, *13* (2), 171–176.

(144) Lloyd-Price, J.; Abu-Ali, G.; Huttenhower, C. The Healthy Human Microbiome. *Genome Med.* **2016**, *8* (1), 1–11.

(145) Narihiro, T.; Kamagata, Y. Anaerobic Cultivation. In *Manual of Environmental Microbiology, 4th Edition*; American Society of Microbiology, 2016; p 2.1.2-1-2.1.2-12.

(146) Thursby, E.; Juge, N. Introduction to the Human Gut Microbiota. *Biochem. J.* **2017**, *474* (11), 1823–1836.

(147) Orcheston-Findlay, L.; Hashemi, A.; Garrill, A.; Nock, V. A Microfluidic Gradient Generator to Simulate the Oxygen Microenvironment in Cancer Cell Culture. *Microelectron. Eng.* **2018**, *195* (April), 107–113.

(148) Sove, R. J.; Fraser, G. M.; Goldman, D.; Ellis, C. G. Finite Element Model of Oxygen Transport for the Design of Geometrically Complex Microfluidic Devices Used in Biological Studies. *PLoS One* **2016**, *11* (11), 1–21.

(149) Kim, M.; Ashida, H.; Ogawa, M.; Yoshikawa, Y.; Mimuro, H.; Sasakawa, C. Bacterial Interactions with the Host Epithelium. *Cell Host Microbe* **2010**, *8* (1), 20–35.

(150) Chueh, B. H.; Huh, D.; Kyrtsos, C. R.; Houssin, T.; Futai, N.; Takayama, S. Leakage-Free Bonding of Porous Membranes into Layered Microfluidic Array Systems. *Anal. Chem.* **2007**, *79* (9), 3504–3508.

(151) Basson, M. D.; Turowski, G.; Emenaker, N. J. Regulation of Human (Caco-2) Intestinal Epithelial Cell Differentiation by Extracellular Matrix Proteins. *Exp. Cell Res.* **1996**, *225* (2), 301–305.

(152) Reading, N. C.; Rasko, D. A.; Torres, A. G.; Sperandio, V. The Two-Component System QseEF and the Membrane Protein QseG Link Adrenergic and Stress Sensing to Bacterial Pathogenesis. *Proc. Natl. Acad. Sci.* **2009**, *106* (14), 5889–5894.

(153) Rousset, M. The Human Colon Carcinoma Cell Lines HT-29 and Caco-2: Two in Vitro Models for the Study of Intestinal Differentiation. *Biochimie* **1986**, *68* (9), 1035–1040.

(154) Sezonov, G.; Joseleau-Petit, D.; D'Ari, R. Escherichia Coli Physiology in Luria-Bertani Broth. *J. Bacteriol.* **2007**, *189* (23), 8746–8749.

(155) Riedel, T. E.; Berelson, W. M.; Nealson, K. H.; Finkel, S. E. Oxygen Consumption Rates of Bacteria under Nutrient-Limited Conditions. *Appl. Environ. Microbiol.* **2013**, *79* (16), 4921–4931.

(156) Maier, E.; Anderson, R. C.; Roy, N. C.; Farin, H. F.; Karthaus, W. R.; Kujala, P.; Rakhshandehroo, M.; Schwank, G.; Vries, R. G. J.; Kalkhoven, E.; et al. Understanding How Commensal Obligate Anaerobic Bacteria Regulate Immune Functions in the Large Intestine. *Nutrients* **2015**, *7*, 45–73.

(157) Walsh, D. I.; Dydek, E. V.; Lock, J. Y.; Carlson, T. L.; Carrier, R. L.; Kong, D. S.; Cabrera, C. R.; Thorsen, T. Emulation of Colonic Oxygen Gradients in a Microdevice. *SLAS Technol.* **2018**, *23* (2), 164–171.

(158) Wood, D. K.; Soriano, A.; Mahadevan, L.; Higgins, J. M.; Bhatia, S. N. A Biophysical Indicator of Vaso-Occlusive Risk in Sickle Cell Disease. *Sci. Transl. Med.* **2012**, *4* (123), 1–8.

(159) Reisner, W.; Pedersen, J. N.; Austin, R. H. DNA Confinement in Nanochannels: Physics and Biological Applications. *Reports Prog. Phys.* **2012**, *75* (10), 106601.

(160) Tamm, C.; Kadekar, S.; Pijuan-Galitó, S.; Annerén, C. Fast and Efficient Transfection of Mouse Embryonic Stem Cells Using Non-Viral Reagents. *Stem Cell Rev.* **2016**, *12* (5), 584–591.

(161) Yamamoto, M.; Okumura, S.; Schwencke, C.; Sadoshima, J.; Ishikawa, Y. High Efficiency Gene Transfer by Multiple Transfection Protocol. *Histochem. J.* **1999**, *31* (4), 241–243.

(162) Jennifer L. Weber , Jeffery J. Scibek, J. L. M. Next-Gen Microcarrier Advances Cell Therapy | GEN https://www.genengnews.com/gen-articles/next-gen-microcarrier-advances-cell-therapy/6237 (accessed Sep 6, 2018).

(163) Hsu, C. Y. M.; Walsh, T.; Borys, B. S.; Kallos, M. S.; Rancourt, D. E. An Integrated Approach toward the Biomanufacturing of Engineered Cell Therapy Products in a Stirred-Suspension Bioreactor. *Mol. Ther. - Methods Clin. Dev.* **2018**, *9*, 376–389.

(164) Abeille, F.; Mittler, F.; Obeid, P.; Huet, M.; Kermarrec, F.; Dolega, M. E.; Navarro, F.; Pouteau, P.; Icard, B.; Gidrol, X.; et al. Continuous Microcarrier-Based Cell Culture in a Benchtop Microfluidic Bioreactor. *Lab Chip* **2014**, *14* (18), 3510–3518.

(165) Esch, E. W.; Bahinski, A.; Huh, D. Organs-on-Chips at the Frontiers of Drug Discovery. *Nat. Rev. Drug Discov.* **2015**, *14* (4), 248–260.

(166) Hubatsch, I.; Ragnarsson, E. G. E.; Artursson, P. Determination of Drug Permeability and Prediction of Drug Absorption in Caco-2 Monolayers. *Nat. Protoc.* **2007**, *2* (9), 2111–2119.

(167) Benson, K.; Cramer, S.; Galla, H.-J. Impedance-Based Cell Monitoring: Barrier Properties and Beyond. *Fluids Barriers CNS* **2013**, *10* (5), 1–11.